# Few-Cycle High Energy Mid-Infrared Pulse From Ho:YLF Laser
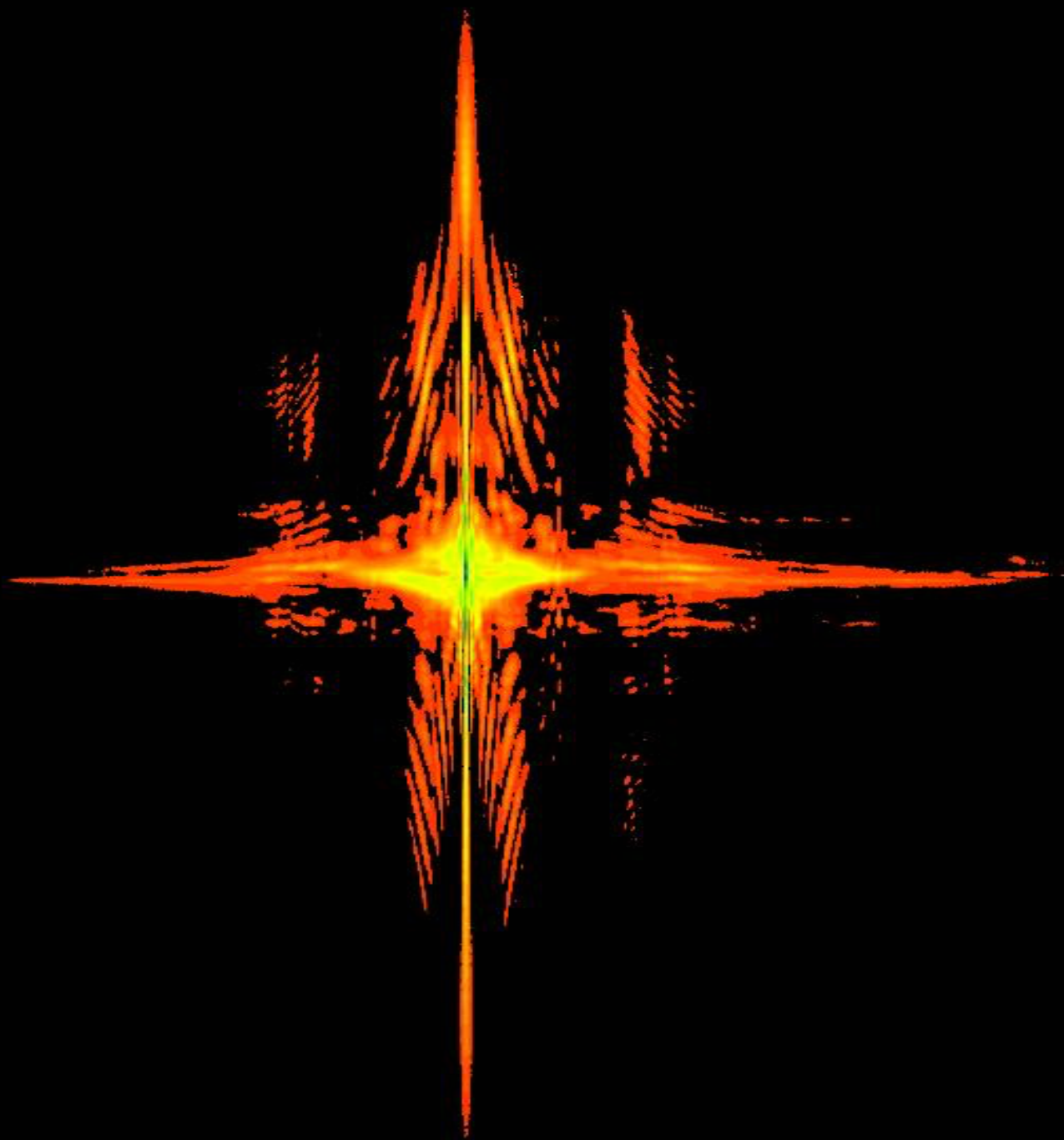
## Krishna Murari

# Few-Cycle High Energy Mid-Infrared Pulse From Ho:YLF Laser

Dissertation zur Erlangung des Doktorgrades
des Fachbereiches Physik
der Universität Hamburg

vorgelegt von

**Krishna Murari**

aus

**Begusarai, India**

Hamburg

2016

ॐ असतो मा सद्गमय ।
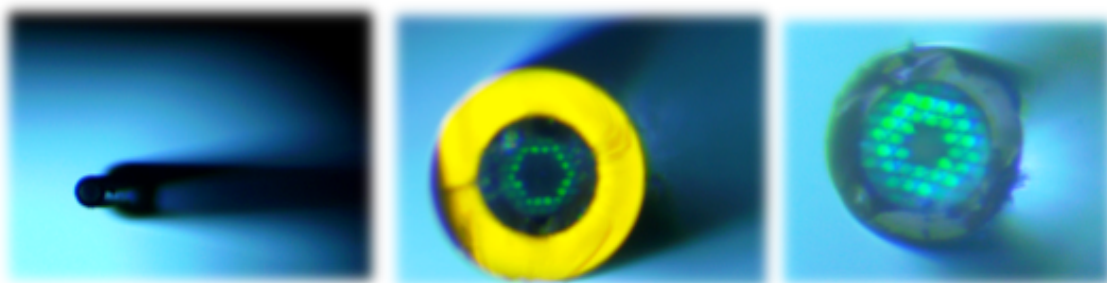
*O Lord! Lead us from darkness to light.*

*- Brihadaranyak Upanishad*
*- Vol. 1 (3.28)*

ॐ सूर्यस्य विवधवरणः पवनेन विघटिताः कराः सभ्रे। वियति धनुः संस्थानाः ये दृश्यन्ते तदिन्द्रधनुः।।

*The multi colored rays of the Sun, being dispersed in a cloudy sky,*
*are seen in the form of a bow, which is called the Rainbow*

- *Bruhatsamhita*
- *Chapter 35*
*(6th Century CE)*

*To my guru and my parents*

**Featured figure:** Bright-field image of Kagome fiber cross-section

# Zusammenfassung

I m vergangenen Jahrzehnt hat die Entwicklung ultrakurzer Laserpulse im mittelinfraroten (MIR) Spektralbereich zu wichtigen Durchbrüchen in der Attosekunden-Wissenschaft und Starkfeldphysik in Atomen, Molekülen und Festkörpern geführt. Die kohärente Synthese von hochenergetischen Pulsen mit Dauern von nur wenigen optischen Zyklen ist eine vielversprechende Technik zur Erzeugung isolierter Attosekunden-Pulse mittels hohe Harmonische Erzeugung (HHG). Eine wirksame Methode, die HHG Cutoff-Energie zu erhöhen, ist die Verwendung von Treiberwellenlängen im MIR, da die ponderomotorische Energie quadratisch mit der Wellenlänge skaliert. Wenn MIR Pulse in den multi-mJ Bereich mit Dauern von wenigen Zyklen skaliert werden, eröffnen sie einen direkten Zugang zu faszinierenden Experimenten an Gasen und Festkörpern. Zudem ermöglichen solche Pulse die Realisierung von hellen HHG-Quellen, die auf einen Labortisch passen. Mit solch einem kompakten Aufbau lassen sich Photonenenergien im Wasserfenster und bis in den keV-Bereich generieren. Die Erzeugung von langwelligen MIR Pulsen mit hoher Intensität blieb jedoch bislang stets eine große Herausforderung, insbesondere ausgehend von hochenergetischen Pikosekunden-Treiberlasern mit 2 $\mu$m Wellenlänge, die für die weitere Energieskalierung von MIR-Pulsen in den multi-mJ Bereich mittels optisch parametrischer Verstärkung (OPA) geeignet sind.

In dieser Arbeit wird einen Frontend für derartige MIR OPAs präsentiert. Insbesondere präsentieren wir ein neuartiges und robustes wenige-Zyklen Treiberlasersystem bei 2 $\mu$m für Starkfeldexperimente, das direkt auf einem Pikosekunden-Ho:YLF-Laser basiert und eine Pulskompression in Kagome-Glasfasern verwendet. Es wurde eine 70-fache Kompression von 140 $\mu$J, 3.3 ps Pulsen aus einem Ho:YLF Verstärker zu 11 $\mu$J, 48 fs Ausgangspulsen erzielt. Die in dieser Dissertation präsentierte Arbeit demonstriert einen direkten Weg zur Erzeugung von wenige-Zyklen MIR Pulsen und wir sind überzeugt, dass die Ultrakurzzeit-Community in Zukunft von dieser Schüsseltechnologie profitieren wird.

Die Resultate werden im wesentlichen in vier Teilen zusammengefasst: Im ersten Teil konzentrieren wir uns auf die Entwicklung einer hochenergetischen 2 $\mu$m Laserquelle als Frontend. Wir vergleichen die zur Verfügung stehenden Technologien im Allgemeinen, sowie die vielversprechendsten Verstärkermedien bei dieser Wellenlänge. Insbesondere, ausgehend von der anspruchsvollen Entwicklung eines

Ho:YLF-Oszillators, wird die Verstärkung und das damit einhergehende Problem der Verschmälerung der spektralen Bandbreite diskutiert. Im zweiten Teil werden zunächst verschiedene nichtlineare Kompressionsverfahren im Allgemeinen, und speziell die Kompression basierend auf verhinderte-Kopplung Kagome Glasfasern diskutiert. Danach werden unsere experimentellen Ergebnisse zur Erzeugung von wenige-Zyklen, $\mu$J-Level, 2-$\mu$m Laserpulsen in einem zweistufigen Kompressionsschema präsentiert. Im dritten Teil, ausgehend von den Grundlagen der optisch parametrischen Verstärkung (OPA), werden die Designkriterien besprochen. Die Anforderungen an die Pump- und Seed-Quellen und adequate Phasenanpassbedingungen zur effizienten Verstärkung werden diskutiert. Des Weiteren haben wir die entwickelte Pumpverstärkerkette zur Weißlicht-Erzeugung verwendet, welche zum späteren Seeden des MIR OPAs verwendet werden soll. Der theoretische Hintergrund der Superkontinuumerzeugung und die Randbedingungen an die Pulsdauer werden diskutiert. Im letzten Teil fassen wir schließlich die Ergebnisse zusammen und präsentieren einen Ausblick.

Als Ausblick kann der hier entwickelte Frontend zur Erzeugung von wenige-Zyklen MIR Pulsen benutzt werden, unter Verwendung von nichtlinearen Kristallen, die auf nicht-Oxiden basieren. Darüber hinaus, da sowohl Pump- als auch Seed-Pulse von derselben Laserquelle stammen, bietet das Schema die Möglichkeit zur passiven Selbststabilisierung der Träger-Einhüllenden-Phase (CEP) der erzeugten Idler-Pulse.

# Abstract

Over the past decade, development of high-energy ultrafast laser sources has led to important breakthroughs in attoscience and strong-field physics study in atoms and molecules. Coherent pulse synthesis of few-cycle high-energy laser pulse is a promising tool to generate isolated attosecond pulses via high harmonics generation (HHG). An effective way to extend the HHG cut-off energy to higher values is making use of long mid-infrared (MIR) driver wavelength, as the ponderomotive potential scales quadratically with wavelength. If properly scaled in energy to multi-mJ level and few-cycle duration, such pulses provide a direct path to intriguing attoscience experiments in gases and solids, which even permit the realization of bright coherent table-top HHG sources in the water-window and keV X-ray region. However, the generation of high-intensity long-wavelength MIR pulses has always remained challenging, in particular starting from high-energy picosecond 2-$\mu$m laser driver, that is suitable for further energy scaling of the MIR pulses to multi-mJ energies by utilizing optical parametric amplifiers (OPAs). In this thesis, a front-end source for such MIR OPA is presented. In particular, a novel and robust strong-field few-cycle 2-$\mu$m laser driver directly from picosecond Ho:YLF laser and utilizing Kagome fiber based compression is presented. We achieved: a 70-fold compression of 140-$\mu$J, 3.3-ps pulses from Ho:YLF amplifier to 48 fs with 11 $\mu$J energy. The work presented in this thesis demonstrates a straightforward path towards generation of few-cycle MIR pulses and we believe that in the future the ultrafast community will benefit from this enabling technology.

The results are summarized in mainly four parts: The first part is focused on the development of a 2-$\mu$m, high-energy laser source as the front-end. Comparison of available technology in general and promising gain media at MIR wavelength are discussed. Starting from the basics of an OPA, the design criteria, constraints on the pump & seed source and proper phase-matching conditions requirement for efficient amplification are discussed. In particular, starting from the challenge of developing a Ho:YLF oscillator, pulse amplification and the problem of gain narrowing are addressed. In the second part, various nonlinear compression schemes are discussed in general and specifically, inhibited-coupling Kagome fiber based compression is discussed. The experimental results for the generation of few-cycle, $\mu$J-level 2-$\mu$m laser pulses in a two-stage compression scheme are then presented. In the third part, the seed pulse generation for the MIR OPA by utilizing supercontinuum (SC)

are presented. The theoretical background of SC generation and the constraints on the pulse duration are discussed. Finally, in the last part, the results obtained are summarized in conclusion and the outlook in presented. The front-end source developed here can be used to generate few-cycle MIR pulses by employing non-oxide based nonlinear crystals. Moreover, as both the pump and seed pulses are derived from the same laser source, it offers the possibility of generating a passively carrier-envelope phase (CEP) stable idler.

# Contents

## II   Few-Cycle Pulse Generation                                                          91

## 6   Nonlinear Pulse Compression                                                          93

# List of Figures

# List of Tables

# List of Journal Publications

**2016**  *Kagome-fiber-based pulse compression of mid-infrared picosecond pulses from a Ho:YLF amplifier*
**<u>Krishna Murari</u>**, Gregory J. Stein, Huseyin Cankaya, Benoît Debord, Frederic Gérôme, Giovanni Cirmi, Oliver D. Mücke, Peng Li, Axel Rühl, Ingmar Hartl, Kyung-Han Hong, Fetah Benabid, Franz X. Kärtner
Optica **43** 816-822

**2016**  *Intracavity gain shaping in millijoule–level, high gain Ho:YLF regenerative amplifiers*
**<u>Krishna Murari</u>**, Huseyin Cankaya, Peter Krötz, Giovanni Cirmi, Peng Li, Axel Rühl, Ingmar Hartl, Franz X. Kärtner
Optics Letters **41** 1114-1117

**2016**  *Novel 2-μm strong-field few-cycle driver from Ho:YLF laser and kagome-fiber compression of picosecond Pulses*
**<u>Krishna Murari</u>**, Giovanni Cirmi, Benoît Debord, Huseyin Cankaya, Frederic Gérôme, Axel Rühl, Ingmar Hartl, Fetah Benabid, Oliver D. Mücke, Franz X. Kärtner
In preparation

**2016**  *Operation regimes, gain dynamics and highly stable operation points of Ho:YLF regenerative amplifiers*
Peter Krötz, Axel Rühl, Gourab Chatterjee, Anne-Laure Calendron, Huseyin Cankaya, **<u>Krishna Murari</u>**, Franz X. Kärtner, Ingmar Hartl, R. J. Dwayne Miller
Optics Express (In Press)

**2016**  *Numerical study of spectral shaping in high-energy Ho:YLF amplifiers*
Peter Krötz, Axel Rühl, **<u>Krishna Murari</u>**, Huseyin Cankaya, Franz X. Kärtner,

# List of Conference Publications

**2016** *Strong-field few-cycle 2-μm pulses via Kagome-fiber compression of picosecond Ho:YLF laser pulses*
**Krishna Murari**, Giovanni Cirmi, Benoît Debord, Huseyin Cankaya, Frederic Gérôme, Axel Ruehl, Ingmar Hartl, Fetah Benabid, Oliver D. Mücke, Franz X. Kärtner
Advanced Solid State Lasers (ASSL) - 2016

**2016** *Kagome fiber based nonlinear pulse compression of 1.8 ps to 250 fs at 2.05 μm from Ho:YLF amplifier*
**Krishna Murari**, Gregory J. Stein, Huseyin Cankaya, Benoît Debord, Frederic Gérôme, Giovanni Cirmi, Oliver D. Mücke, Peng Li, Axel Rühl, Ingmar Hartl, Kyung-Han Hong, Franz Benabid, Franz X. Kärtner
Conference on Lasers and Electro-Optics (CLEO/QELS) FTh1M.8 - 2016

**2016** *Stability optimized, 4 mJ and 1.2-ps pulses from a Ho:YLF regenerative amplifier*
Peter Krötz, Gourab Chatterjee, Axel Rühl, **Krishna Murari**, Franz X. Kärtner, Ingmar Hartl, R. J. Dwayne Miller
Conference on Lasers and Electro-Optics (CLEO/QELS) SF2I.2 - 2016

**2016** *High energetic and highly stable pulses from a Ho:YLF regenerative amplifier*
Peter Krötz, Axel Rühl, Gourab Chatterjee, Peng Li, **Krishna Murari**, Huseyin Cankaya, Anne-laure Calendron, Franz X. Kärtner, Ingmar Hartl, R. J. Dwayne Miller
Proc. SPIE 9726, Solid State Lasers XXV: Technology and Devices

**2015** *Sub-300 fs, 0.5 mJ pulse at 1 kHz from Ho:YLF amplifier and Kagome pulse compression*
**Krishna Murari**, Huseyin Cankaya, Benoît Debord, Peng Li, Giovanni Cirmi, Shaobo Fang, Guilio M. Rossi, Oliver D. Mücke, Peter Krötz, Gregory J. Stein,

# List of Abbreviations

| | |
|---|---|
| AC | Auto-correlation |
| BBO | Beta Borium Borate |
| CEP | Carrier Envelope Phase |
| CFEL | Centre for Free Electron Laser Sciences |
| CPA | Chirped pulse amplifier |
| CVBG | Chirped volume Bragg grating |
| CW | Continuous wave |
| DCM | Double Chirped Mirror |
| DESY | Deutsch Electron Synchrotron |
| DFG | Difference Frequency Generation |
| DWDM | Dense Wavelength Division Multiplexing |
| EO | Electro-optic |
| FFT | Fast Fourier Transform |
| FR | Femtosecond Regime |
| FROG | Frequency Resolved Optical Gating |
| FWM | Four Wave Mixing |
| FWHM | Full-width at Half Maximum |
| GDD | Group Delay Dispersion |
| GVD | Group Velocity Dispersion |
| HC-PCF | Hollow Core - Photonic Crystal Fiber |
| HHG | High Harmonic Generation |
| IC | Inhibited Coupling |
| KLM | Kerr-Lens Modelocking |
| LLBNL | Lawrence Livermore Berkely National Lab |
| Mev | Mega electron-volt |
| MFD | Mode Field Diameter |

| MI | Modulation Instability |
|---|---|
| MIR | Mid-Infrared |
| NIR | Near Infrared |
| NOPA | Non-collinear Optical Parametric Amplifier |
| NPE | Nonlinear Polarization Evolution |
| OCT | Optical Coherence Tomography |
| OPA | Optical Paramteric Amplifier |
| OPCPA | Optical Parametric Chirped Pulse Amplifier |
| OPG | Optical Parametric Generation |
| PBG | Photonic Bandgap |
| PR | Picosecond Regime |
| QC | Quantum Cascade Lasers |
| QWP | Quarter-wave Plate |
| RA | Regenerative Amplifier |
| RIN | Relative Intensity Noise |
| RMS | Root-Mean-Square |
| RT | Round-trip |
| RTP | Rubidium Titanyl Phosphate |
| SC | Supercontinuum |
| SESAM | Semiconductor Saturable Absorber Mirror |
| SHG | Second Harmonic Generation |
| SPA | Single-pass Amplifier |
| SPM | Self-Phase Modulation |
| SRS | Stimulated Raman Scattering |
| TFP | Thin-film Polarizer |
| VSA | Vector Spectrum Analyzer |
| WDM | Wavelength Division Multiplexing |
| XFEL | X-Ray Free Electron Laser |
| ZDW | Zero Dispersion Wavelength |

# Introduction

Generation of the controlled shortest event ever, has always been exciting since the advent of laser and with the discovery of modelocking in 1964. In the past decades, several refining techniques such as dispersion control and Kerr nonlinearities were discovered which led to the development of few-to-sub-optical cycle pulses. In the 90s, with the discovery of the chirped-pulse amplification (CPA) technique and Ti:Sappire (Ti:Sapp) as a gain medium having ultrabroad gain bandwidth, generation of high-energy few-cycle laser pulses have become a reality and is now routinely achieved in many laboratories. Over the past decade, high-energy, few-to-single-cycle laser pulses from Ti:Sapp CPA systems have found its way to a wide range of applications; from fundamental sciences to industry, from telecommunication to medicine etc. These ultra-intense pulses have led to important breakthroughs in studying various attoscience phenomena in fundamental strong-field physics and in particular high-harmonic generation (HHG) [8, 9].

Ultrashort laser pulses enable probing of various phenomena in nature that occur on a $10^{-15}$ $fs$ - $10^{-18}$ $as$ time scale. Just the same way as in a camera with a shutter speed faster than a moving object can freeze or capture its movement, an ultrashort laser pulse whose duration can be as short as $fs$ can freeze the motion of fast moving objects such as molecules or electrons. These pulses has the ability to probe excited molecules in matter with femtosecond time-scales that opens up completely new fields of research in physics, chemistry and biology. Moreover, due to their high

1

intensities they open the study of new regimes in light-matter interaction [10]. A. H. Zewail was the first to probe the complex dissociation dynamics of molecules using a mode-locked laser pulse and was awarded the Nobel Prize in chemistry in 1999. The study of fast dynamical process is limited by the duration of the light pulses available and hence, generation of shorter and shorter pulses are desired. But at the same time broadband frequency tunability is also required so that different optical transitions in resonance occurring at different photon energies in the system can be probed. Hence both frequency tunability as well as shorter pulse duration are important issues to be addressed for these studies.

In the recent years, attosecond technology has emerged as a promising tool for molecular imaging with atomic scale-resolution. Use of this technology envisions real-time three-dimensional (3D) molecular movie with a sub-angstrom of spatial resolution and sub-femtosecond time resolution. The most successful model to explain the generation of attosecond pulses is the three-step model shown in the figure 1.1 [1]. it can be seen in the figure that as an intense is incident on an atom, an electron wavepacket is extracted. Initially, the electrons are pulled away from the atom and later when the electric field reveres, they are pulled back and re-collides during the small fraction of the laser oscillation cycle thereby emitting attosecond radiation. The intensities of these laser pulses reaching $10^{20}$ W/cm$^2$ has an electric field up to $10^{12}$ V/cm, which is hundred times higher than the Coulomb field binding the ground-state electron in a hydrogen atom and in principle can generate a physical environment as those found in interior of stellar planets or close to black holes in the laboratory. For example, the ultrahigh field can drive the electrons to relativistic speed with an oscillating energy of 10 MeV thereby producing extreme light pressure $P$, $(P = I/c)$ in the range of giga-bars, giga-gauss magnetic fields and violent acceleration of $10^{21}$ times gravity. Interaction of these ultra-high intense beam with a relativistic particle like an electron can emit oscillatory energy equal to one Compton wavelength also called as 'quiver energy' ($E_{osc} = M_o\,c^2\sqrt{1 + 2U_P/m_o\,c^2} - 1$) which is equal to twice its rest mass energy ($m_o c^2 = 0.5 MeV$) and can open a completely new era of nonlinear quantum electrodynamics. When these pulses are focused in a gas medium, the high pressure of light can displace the electrons as it propagates, which is then pulled back by the charge gradient after the pulses go off, thereby generating a large plasma wave oscillating at the electron plasma frequency $\omega_p = \sqrt{4\pi n_o\,e^2/\gamma m_0}$, where $n_0$ is the plasma density and $\gamma$ is the relativistic factor. This plasma waves forms a train of accelerating bunches of electrons that can support plasma density
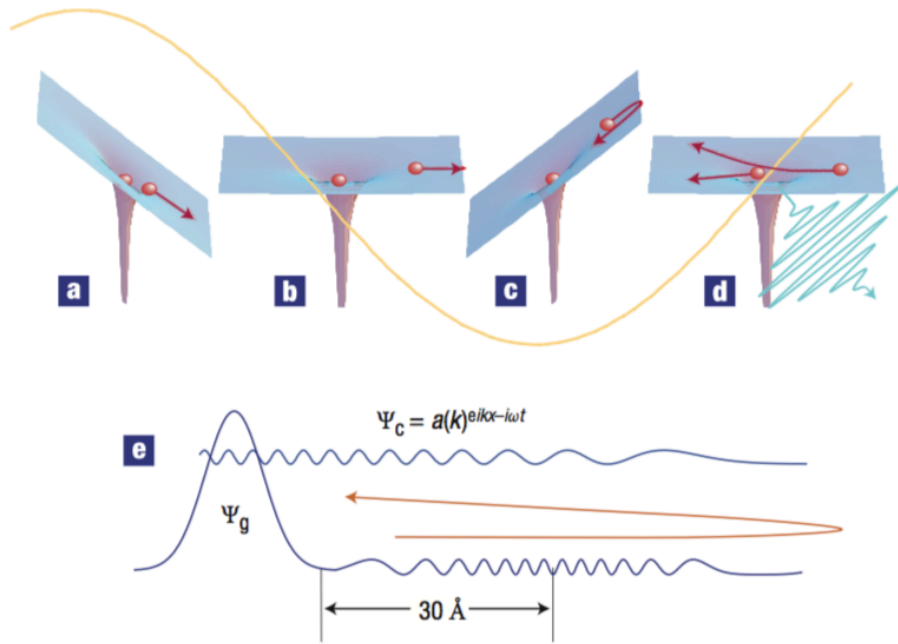
Figure 1.1: Attosecond pulse generation; a-d. An electron wavepacket is extracted from an atom when an intense femtosecond near-infrared light pulse is incident on it. Initially, the electron is pulled away from the atom (a)-(b), which is then pulled back when the field reverses, (c) it eventually re-collides during the small fraction of laser oscillation cycle and (d) thereby emit attosecond radiations (figure reproduced from [1]).

of $10^{18}$ cm$^{-3}$ resulting in accelerating gradient field ($E_0 = mc\,(\omega_p/e) = n_0^{1/2}$) of 100 GV/m in a table-top laboratory, which is three orders of magnitude higher than conventional large-scale facilities like the Linear Accelerator (LINAC) at Stanford. An astrophysical environment governed by hydrodynamics, radiation transport, and gravitational interaction, recreated in a laboratory can bring science fascination to a new horizon [11]. This is being realized by integrating the high peak power lasers with the modern day synchrotrons and accelerators like those at Deutsches Electronen-Synchrotron (DESY), Stanford Linear Accelerator Center (SLAC) or X-Ray Free Electron Lasers (XFEL).

Though, the first femtosecond laser source based on dye laser (*'liquid laser'*) was demonstrated in 1980s, the development in the field was plagued by for several years due to low saturation intensities of the dye molecules, alignment sensitivities, and stability issues. However the next decade witnessed a revolution in the field due to some of the three biggest discoveries in the field: of (1) Ti:sapphire laser crystals, (2) Kerr-lens modelocking and (3) chirped pulse amplification technique leading to complete replacement of liquid dye lasers with the solid state ones.

Ti:sapphire material due to its excellent thermal properties and exceptionally broad gain-bandwidth (from 600 - 1000 nm), attracted huge attention in the laser community. KLM is a powerful technique for passive modelocking to generate sub-100 fs laser pulses in nJ-energy level and CPA provided a tool to boost the energy from nJ to mJ-level leading to a gain of 6 - 8 orders of magnitude.

Due to an extremely wide range of applications of ultrafast lasers, they can be divided in terms of four main categories with respect to its different properties [12]:

- Ultrashort pulse duration: These lasers are used to study fast moving objects such as molecules or electrons and can measure the relaxation process of carriers in semiconductors, semiconductors, chemical reaction and high-speed electronics.

- High repetition rate: Lasers with high rep rate of GHz range are highly used in the telecommunication industry, photonics switching device, optical interconnection, optical clocks and very large scale integrated devices (VLSI).

- Broadband spectrum: The very broad spectrum of an ultrafast laser source is very attractive for optical coherence tomography (OCT) used for non-invasive imaging of internal tissues. The broad spectrum can produce higher longitudinal and spatial resolution up to few micrometers. Due to its high stability of longitudinal modes, it can be used for frequency comb applications and dense wavelength-division-multiplexing (DWDM). The frequency comb can be used in optical metrology applications and can act as a perfect ruler in the frequency domain with which an unknown optical frequency can be determined.

- High peak intensity: The high peak intensity of these lasers can be used to excite higher nonlinear process in a material. They can be used to alter materials by cold ablation process (material undergo phase change directly from solid to gas). The high peak intensity can be used in high-field physics like HHG and laser plasma X-rays generation used in X-ray imaging and microscopy, photoelectron spectroscopy and X-ray diffraction. The ultrashort pulses can be used in medical surgery for better surgical precision that reduces secondary damage effects
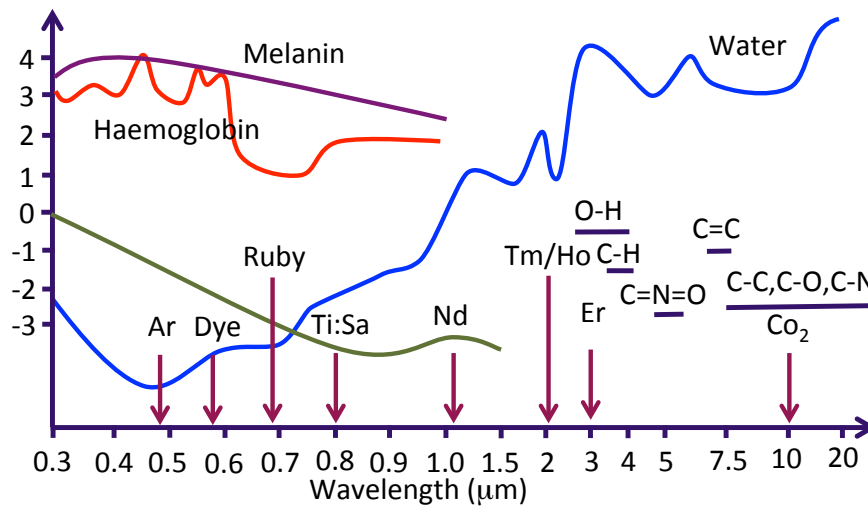
Figure 1.2: Absorption and scattering band of tissue and various important molecules in spectroscopy. Shown by the arrows are the common laser sources at that specific wavelength (figure adapted from [2]).

## 1.1 Why mid-infrared?

In recent years, high-energy ultrashort mid-infrared (MIR) laser sources have experienced rapid technological advancements due to its wide range of applications especially in spectroscopy, environment sensing, life sciences etc. MIR wavelengths are attractive due to the presence of atmospheric transparency window in this range and *'molecular fingerprint'* region, where various molecules have strong roto-vibrational absorption lines. They are of immense importance in bio-medical and biological research due to absorption peaks in a wide range of molecules in the nature. Several important molecules offer resonances at these wavelengths making it an optimum choice for spectroscopy [13]. The absorption band of water and various tissues & molecules that forms the building blocks of life lie in this region [9, 2]. Due to the strong absorption window of water in MIR, pulses at this wavelength can be efficiently used in surgical applications like ophthalmology, neurosurgery and even *'nano-scissors'* [2]. The specific *'molecular fingerprint'* region can also be used for human breath analysis, since the exhaled human breath contains several *'biomarkers'* compounds that are correlated to specific internal diseases and whose absorption peaks lie in this window. Thereby developing noninvasive methods of health screening including deadly diseases like cancer, HIV and other respiratory, kidney and liver issues [2].

MIR laser sources are also of great importance in the fundamental strong-field

study of matter where not only high intensities, but also careful control of both electric field and spectral phase are an important prerequisite. For example, when investigating the fundamental atomic process, there are always competing processes like tunneling and multiphoton ionization. With near-infrared (NIR) pulses, there exists mix of both regimes, however, with MIR pulse that has lower photon energy as compared to NIR, offers better information with clarity by avoiding the multiphoton ionization regimes. Morover, in attosecond pulse generation via HHG, the harmonic cutoff scales with the square of wavelength according to $\hbar\omega = I + 3.17U_p$, where, the ponderomotive energy is given by, $U_p \propto I_P\lambda^2$ [14, 15]. Hence, MIR laser pulses can help in scaling harmonic cutoff thereby yielding shorter attosecond pulses. For example, a ∼4 $\mu$m source can generate harmonic spectra whose photon energy is well above 1 keV, thereby generating pulse duration below atomic unit of time [16, 9]. However, it comes with higher losses and lower yield [17], which can be compensated by better phase-matching [16]. Another requirement of these study comes from the extremely low-yield of harmonics $10^{-6}$ of the drive laser photons (need reference). Due to this low yield, long data collection times are needed which in turn demands higher laser stability, that is not often possible due to the extremely complex nature of the pulse generation process. It is therefore beneficial to have higher repetition rate systems, that can acquire large number of samples in less time. For instance, the experiments which take six days for measurement with a 1 kHz system, can be completed in 90 minutes when using a 100 kHz system. The requirement of stability and repetition rate is a great challenge and has limitations even if today's most advanced technology is used.

Furthermore, carrier-envelope phase (CEP)-stabilized few-cycle (sub-100 fs) laser pulses at long wavelengths are in high demand for complex experiments in attoscience and strong-field physics. The CEP is defined as the offset between the peak of the pulse field envelope and the peak of the underlying electric field. For a multi-cycle pulse, the CEP has typically only a minor impact on strong-field processes but it is important for few-cycle pulses, as the shape of the electric field strongly varies with the CEP value, and it is also important that the shape remains same for successive laser pulses. Even the most advanced systems around the world, with active stabilization, can generate CEP-locking for only several hours. MIR laser pulses are of great advantage here, as it allows the use of seed source with passive CEP stabilization and has been proven to be stable with slow drift up to $> 240$ hours. Hence, these pulses permit the study of several exotic phenomena in the

nature like novel regimes in photo-ionization of gases [18, 19], the breakdown of the dipole approximation [20], the wavelength-dependence of re-collision physics [21], [22], and the investigation of non-perturbative strong-field effects in solids such as the dynamical Franz-Keldysh effect [23, 24] and HHG from Bloch oscillations [25, 26].

However, despite much efforts, scientists have always struggled to find a similarly broadband gain medium at a wavelength longer than Ti:Sapp, and until now there is no direct means (without involving frequency conversion) to generate few-cycle high-energy pulses other than at 800 nm. Today, the state-of-art technology to generate a few-cycle pulse at MIR wavelength is by frequency conversion via optical parametric amplification (OPA) and optical parametric chirped-pulse amplification (OPCPA) optionally followed by nonlinear spectral broadening [27, 28]. The most common method to access ultrashort pulses in MIR is via noncollinear OPA (NOPA) of a white-light supercontinuum or difference-frequency generation (DFG) [29] as a seed source from Ti:Sapp [30] or Yb-based systems [31]. Using these techniques, 25 fs pulse at 3 $\mu$m wavelength and 2 $\mu$J energy was generated [32]. These systems have an advantage of passive CEP stabilization and moderate energy have been achieved. However, the major disadvantage of these techniques are low conversion efficiency and inherent stability issues of the pump lasers. Hence few-cyle pulses are limited in scaling to higher energies especially in MIR where the efficiency is even reduced. Furthermore, most of these systems rely on NIR wavelength pump sources at 800 nm and 1 $\mu$m [18, 19], that has limited their further scaling of wavelength beyond $\sim$4 $\mu$m [33]. These pump sources limit access to the long wavelength region, as most of the oxide crystals used for an OPA are not transparent above 4 - 5 $\mu$m. Also, due to their unfavorable quantum defect at longer wavelength, the quantum efficiency is limited.

Non-oxide crystals like ZGP, CdSiP$_2$ and OP-GaAs, which have a transparency window from 2 - 8 $\mu$m, require long wavelength pumping for efficient parametric generation of broadband MIR pulses beyond 4 $\mu$m due to better phase-matching condition and higher conversion efficiency [34, 35, 36]. When followed by filamentation and pulse self-compression in dielectrics [37, 26, 38] and if properly scaled in pulse energy to the multi-mJ level, IR pulses even permit the realization of bright coherent table-top HHG sources in the water-window and keV soft X-ray region [16]. Hence 2-$\mu$m, mJ-level laser sources with sub-ps duration are preferred to generate stable and coherent white-light supercontinuum for pumping and seeding the non-oxide crystal based OPA and have self-CEP-stable idler [32, 33, 39, 40]. The goal of this

Ph.D. work is to develop few-cycle high-energy pulses in the MIR. In this work, we demonstrate for the first time the generation of few-cycle ultrashort high-energy pulses at 2 $\mu$m without using parametric conversion. We further generate white light in a bulk medium as a MIR seed source. These pulses can be amplified using an OPA and can generate CEP-stable idler up to 7 - 8 $\mu$m.

# 2

# Outline and Scope of the Thesis

I n this dissertation, the initial development towards generation of high-energy and few-cycle MIR pulses are presented, in particular, a novel and robust strong-field few-cycle 2-$\mu$m laser driver based on Ho:YLF amplifier and Kagome fiber compression has been developed. The thesis is divided into four main parts, which are subdivided into eight chapters as summarized in the mind-map below.

The first part of the thesis is focused on the development of 2-$\mu$m high-energy laser source as the front-end pump chain for the OPA. In particular, starting from the challenge of development of Ho:YLF oscillator, its amplification and the problem of gain narrowing are addressed. In Chapter 3, general discussion and comparison of the available technology and gain medium at 2 $\mu$m wavelength are discussed. The advantages, & disadvantages of the available MIR sources are also presented. In particular OPA in general starting from the basics, the need for right pump & seed source, design criteria, proper phase-matching conditions and the nonlinear crystal required to amplify and generate few-cycle pulses at long MIR wavelengths are discussed. In Chapter 4, the development of a low-energy 2-$\mu$m Ho:YLF seed oscillator, to be later amplified with a commercial Ho:YLF amplifier are discussed. However, due to design constraints of the commercially available semiconductor saturable absorber (SESAM), the solid-state oscillator could not be stably mode-locked. Due to this, a joint collaboration with Ingmar Hartl's group at DESY was initiated, for the development of Ho:fiber oscillator. The fiber oscillator generated
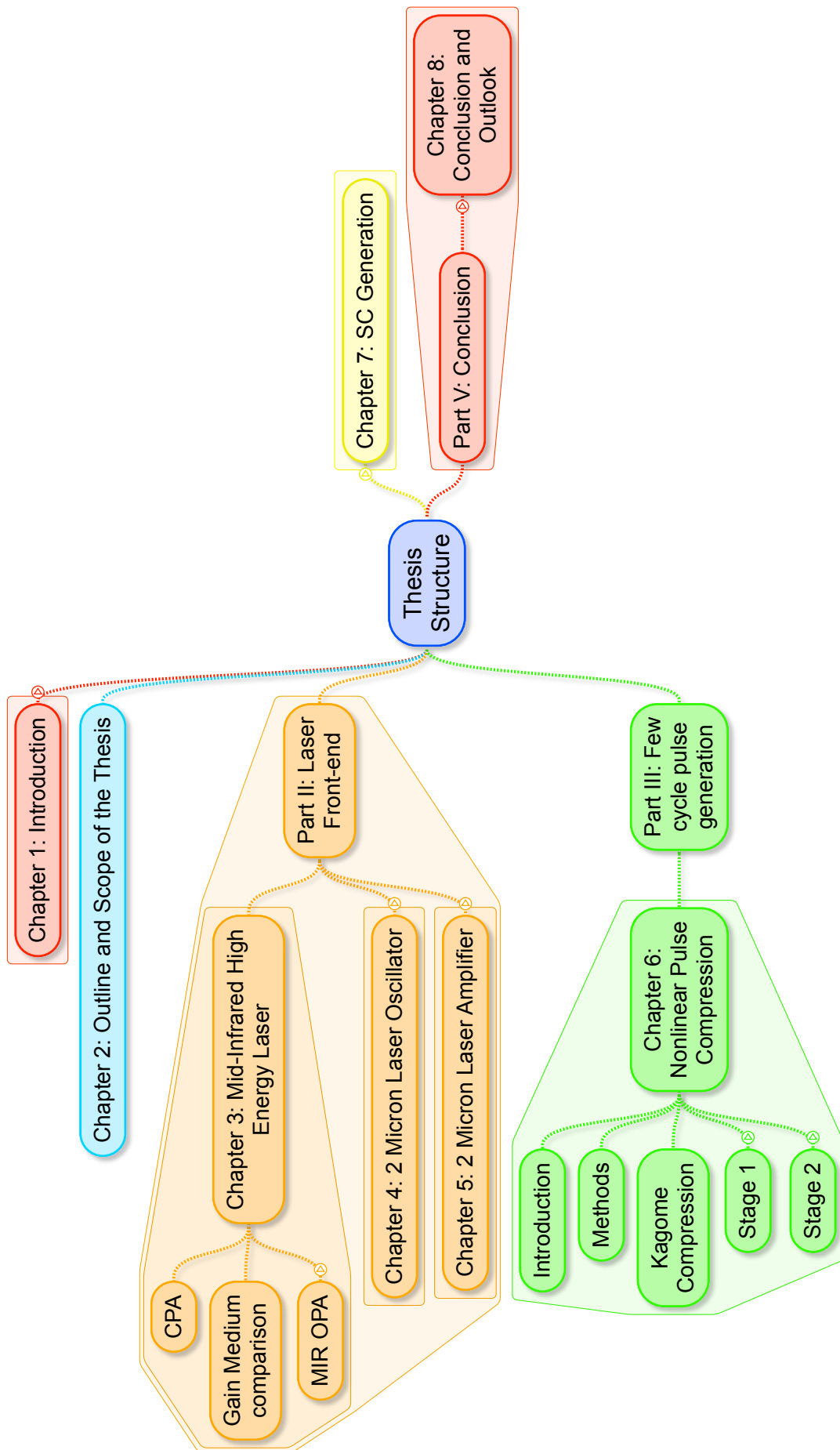
Figure 2.1: Mind-map of the structure of this thesis

stable mode-locked pulses in the *fs*-regime with an output energy of 1-nJ and pulse duration of 160 fs. The low-energy pulses from the seed fiber oscillator was amplified using a commercial Ho:YLF amplifier to the mJ-level. In Chapter 5, the Ho:YLF amplifier chain is discussed. The amplification was done using the conventional CPA system where stretching and compression were carried out using chirped volume Bragg gratings (CVBG). The amplifier consists of Ho:YLF regenerative amplifier (RA) and a booster single-pass amplifier (SPA). After pulse amplification and compression, the pulse energy as high as 2 mJ and duration of 3.4 ps was obtained. In Chapter 6, the effect of gain narrowing in the amplifier and the method to reduce this effect are discussed. An etalon as a frequency-selective filter was employed for intracavity gain shaping inside the RA to reduce the effect of gain narrowing and broaden the output spectrum. By this method, the output spectrum was broadened by ∼50 % and the FWHM spectrum of 2.9 nm was broadened to 5.4 nm corresponding to Fourier limited duration of 1-ps. After amplification of the broadened spectrum in the booster amplifier, a total energy of 2.2 mJ with a pulse duration of 2.4 ps at 1 kHz and pulse-to-pulse root-mean-square (RMS) fluctuations of <1 % was achieved.

In the second part, the generation of few-cycle $\mu$J-level pulses at 2 $\mu$m by utilizing a two-stage nonlinear compression of the ps-pulses from a Ho:YLF amplifier in Kagome fibers are presented. A 70-fold compression of 140-$\mu$J, 3.4-ps pulses from Ho:YLF amplifier to 48 fs and 11 $\mu$J energy was achieved. In Chapter 6, first discuss various nonlinear compression schemes in general and in particular inhibited coupling Kagome fiber based compression are discussed. A small part of the energy of the output pulse from the amplifier chain, discussed in the first part, are spectrally broadened and compressed using gas-filled Kagome-type hollow-core photonic crystal fiber (HC-PCF) in two stages. Later, the experimental and the simulation results are summarized. Spectral broadening is studied for different experimental conditions with variations of gas pressure and incident pulse energies.

In the third part, mainly the seed source generation by utlizing the pump-chain is discussed. In Chapter 7, the principle of supercontinuum (SC) generation is discussed and later the initial results of SC generation are presented. Finally, in the last part, all the results are summarized in conclusion and the outlook is presented. As the outlook the source developed in the thesis, if properly phase matched in a nonlinear crystal ZGP, can produce pulses at 7 - 8 $\mu$m wavelength with the possibility of CEP stable idler, as both pump and seed pulses are derived from the same laser source.

# Part I

# Pump Chain

# Mid-Infrared High-Energy Laser

In this chapter, various laser source technologies available for the generation of MIR pulses are discussed. A comparison of the technologies with their advantages and & disadvantages are presented. In particular, a detailed discussion of OPA is presented. Starting from theoretical formalism of an OPA using Maxwell's equation, gain in an OPA & its relation to the nonlinear co-efficient, design consideration and types of OPA are discussed. Nonlinear crystals used in a MIR OPA and the requirement of pump & seed source are then discussed.

## 3.1   Mid-infrared sources

MIR sources avaiblable fall into the following categories: [41]

- Rare-earth doped lasers (Tm, Ho, Er)

- Transition metal-ion lasers (Cr, Fe)

- Antimonide-based semiconductor lasers

- Quantum cascade lasers

- Optical parametric sources
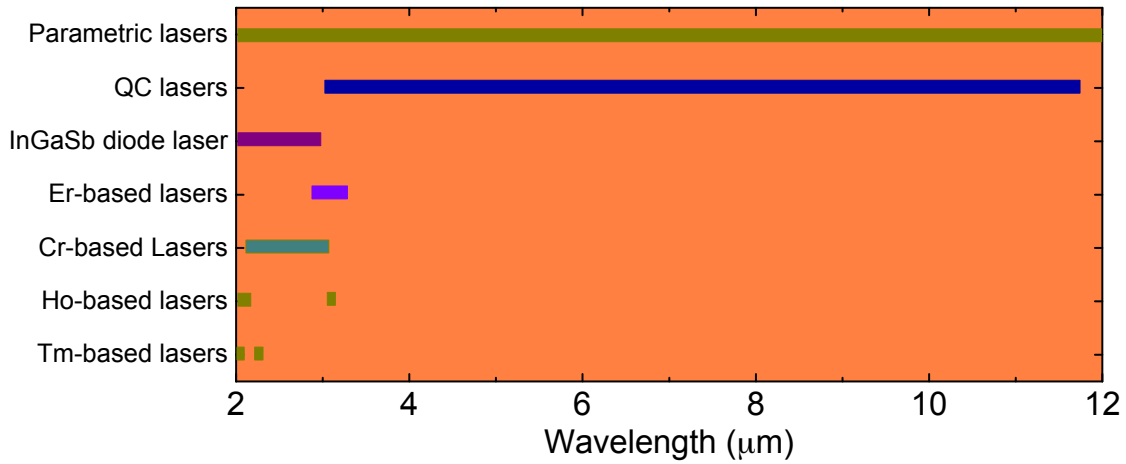
Figure 3.1: Spectral coverage of the various mid-infrared sources.

## 3.1.1 Rare-earth doped lasers (Tm, Ho, Er)

**$Tm^{+3}$ ion based lasers**

$Tm^{+}3$ ions provide the laser transition using $^3H_4 \rightarrow \;^3H_6$ in a quasi-three-level scheme and provide emission in the range of 1.9 - 2 $\mu$m. Cross-relaxation (CR) energy transfer process that exists between the $Tm^{+3}$ ions, helps to achieve very high slope efficiency exceeding the Stokes limit. In a CR process, two ground-level ions are excited to the upper level at the same time, by absorbing only one photon implying that one excited $Tm^{+3}$ ion at $^3F_4$ level produces two $Tm^{+3}$ ions at $^3H_4$ level. However, this process suffers from inefficient thermal removal and thus increased thermal load requiring better cooling methods which in turn limits the maximum energy extraction.

**$Ho^{+3}$ ion based lasers**

Lasers based on $Ho^{+3}$ ions provide emission in the range of 1.95 - 2.15 $\mu$m using $^5I_7 \rightarrow \;^5I_8$ transitions and 2.85 - 3.05 $\mu$m using $^5I_6 \rightarrow \;^5I_7$ transitions. Laser transition $^5I_6 \rightarrow \;^5I_7$ are not very commonly used due to its self-terminating behavior. Laser emission using $^5I_7 \rightarrow \;^5I_8$ transition requires pumping around 1.9 $\mu$m and cannot be pumped using commercial diodes whose availability is limited around 1 $\mu$m. Therefore, either energy transfer process in Tm-Ho co-doping is utilized or $Tm^{+3}$ ion based laser is used separately, to pump $Ho^{+3}$ lasers. In the case of Tm-Ho co-doped system, $Tm^{+3}$ ions act as a sensitizer that absorbs the pump light from
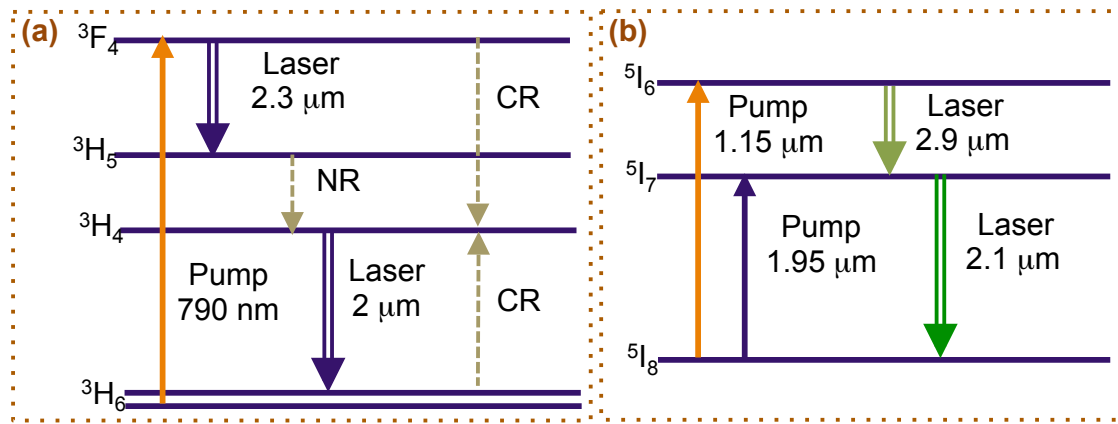
Figure 3.2: Energy level diagram of (a) $Tm^{+3}$ ion with their energy transfer process; NR and CR represents the nonradioactive decay and cross-relaxation process, respectively (b) $Ho^{+3}$ ions.

a commercial diode around 790 nm, and it is then transferred to the active $Ho^{+3}$ ions. However, the thermal load on the system is high due to the up-conversion losses and irreversible transfer of energy between the Tm and Ho ions that severely limits the performance of the laser. Hence, for a high energy system, direct pumping of $Ho^{+3}$ ions from $^5I_7$ level are preferred and are advantageous for several reasons: low quantum defect (1.9 - 2 $\mu$m), no sensitizer ion required, reduced up-conversion loss, high extraction efficiency and reduced temperature dependence on the gain. By using direct pumping schemes, high energy solid-state $Ho^{+3}$ lasers have been achieved. However, Tm-Ho co-doped systems are quite useful for fiber lasers as they allow effective heat dissipation.

**$Er^{+3}$ ion based lasers**

For past few decades, $Er^{+3}$ transition of $^4I_{13/2} \to {}^4I_{15/2}$ emitting at 1.55 $\mu$m have been widely used in telecommunication. However, the transition $^4I_{11/2} \to {}^4I_{13/2}$ that emits at 2.58 - 2.94 $\mu$m was until now unexplored. This emission wavelength is very useful as it coincides with O-H vibration in water which makes it strongly absorbed by biological issues within $\mu$m-range and very attractive for medical applications. And the advantage for these transitions are that they can be pumped directly by commercial 960 nm diodes. However, it also has a drawback that the transition $^4I_{11/2} \to {}^4I_{13/2}$ is self-terminating, however, people have demonstrated efficient operation utilizing this transition.
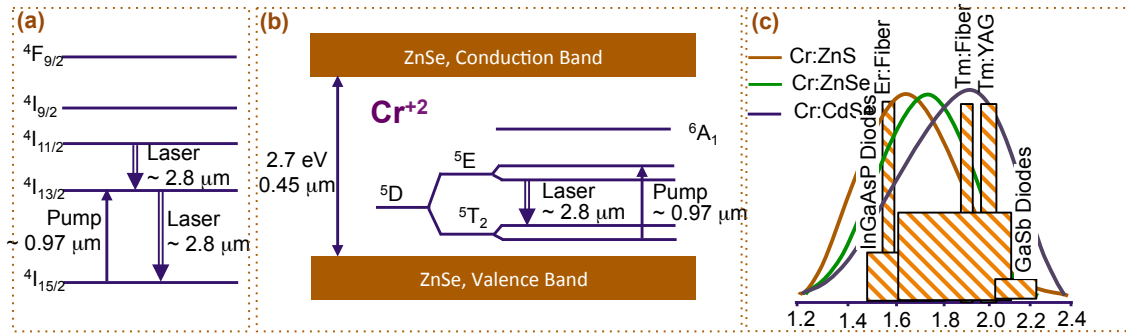
Figure 3.3: Energy level diagram of (a) $Er^{+3}$, (b) $Cr^{+2}$ in ZnSe and (c) absorption spectra of $Cr^{+2}$ doped II-VI media.

### 3.1.2 Transition metal-ion lasers (Cr, Fe)

$Cr^{+2}$ doped II-VI compounds are laser materials that have broad absorption and emission bandwidth in the 2 - 4 $\mu$m range. They belong to a vibronic family and there exists strong coupling between the electric field of the crystal and the electrons of the transition metal in $3d$ level (figure 3.3), which is the cause for broad emission bandwidth. In the figure 3.3, energy levels of $Cr^{+2}$ are shown inside the bandgap of ZnSe as this is the most commonly used host medium. We can see that the lowest $Cr^{+2}$ level $^5D$ due to the crystal field is split into an excited doublet $^5E$ and ground-state triplet $^5T_2$ which are further split due to other interactions like phonon interaction. Due to its very broad absorption band, it can be pumped by several sources like Tm-doped lasers at 1.9 $\mu$m, Er-doped lasers at 1.55 $\mu$m or infrared laser diodes. They have a very small quantum defect and due to its very broad emission bandwidth, it can be used to generate very short pulses and is termed as *'Ti:Sapp of MIR'*. However, output power is limited due to strong thermal lensing and are an ongoing part of research to develop high power Cr:ZnSe lasers. If instead of $Cr^{+2}$, $Fe^{+2}$ are used as a dopant, longer emission wavelength is achieved at 4 - 5 $\mu$m, however, their efficiencies are limited due to the presence of strong multi-phonon quenching at the room temperature.

### 3.1.3 Antimonide based semiconductor lasers

Multiple quantum well semiconductor based on GaIn(As)Sb/AlGaAnSb have been successfully used to generate lasers between 2 - 3 $\mu$m. Since in semiconductor lasers, the selected alloy determines the emission wavelength, wide tunability can be achieved. However, the efficiency decreases drastically beyond 2 $\mu$m due to the

Auger effect limiting the carrier lifetime.

### 3.1.4 Quantum cascade lasers

The laser transitions in quantum cascade (QC) lasers, in contrast to semiconductor lasers occur in the conduction band between the initial and final bands called sub-bands that arises due to quantization of the electronic states. As a consequence, unlike semiconductor lasers, where the emission wavelength is determined by the bandgap arising from the selected alloy, in QC lasers, it depends on the thickness of the quantum well. Thus, the mature III-V compound technology such as GaAs and InP can be used for different emission wavelength. Therefore there exists almost no fundamental limit to the longest possible wavelength and people have used it to generate radiations as far as THz wave. However, the limitation of the shortest wavelength possible arises from the height of the conduction band offset between the heterostructures and is limited to 3.4 $\mu$m for InP based lasers and 8 $\mu$m for GaAs-based lasers. Heat dissipation is also an issue for QC lasers and limits the quantum efficiency.

### 3.1.5 Optical parametric sources

Optical parametric oscillators (OPO), optical parametric generation (OPG), difference frequency generation (DFG) are commonly used optical parametric sources (OPS) based on frequency down-conversion to produce light at the wavelength where direct laser perform poorly. The advantages of OPS include:

- Both CW and pulsed operation at very high rep rate possible

- Very high-energy pulse possible

- Very broad spectral range can be covered

- System can be rugged and compact

Some of the commonly used materials in OPS are shown in the figure 3.4. For wavelength ranging from 2 - 4.5 $\mu$m, crystals like lithium niobate (LiNbO$_3$), potassium titanyl phosphate (KTP), potassium titanyl arsenate (KTA) and lithium tantalate (LiTaO$_3$) are used that can be pumped around 1 $\mu$m wavelength. However, they
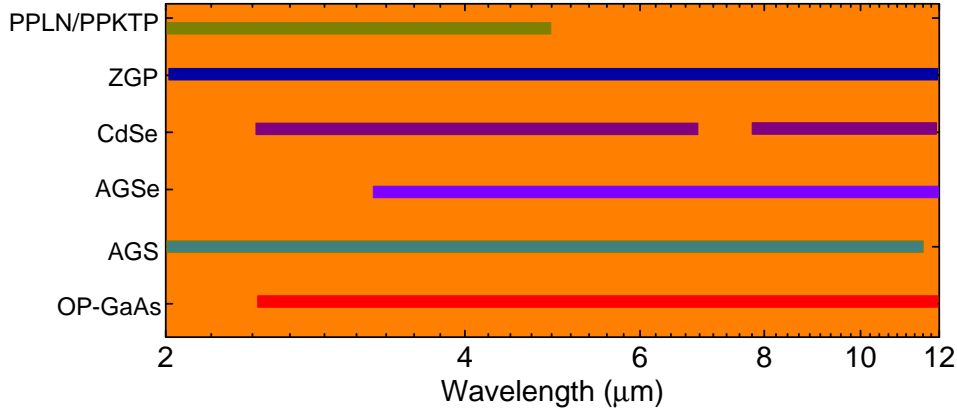
Figure 3.4: Comparison of transmission range of various MIR nonlinear crystals used in an OPA covering from 2 - 12 $\mu$m.

cannot be used for wavelength above 4.5 $\mu$m as they exhibit strong bulk absorption for longer wavelength. For longer wavelength, crystals like zinc germanium phosphide (ZnGeP$_2$ or ZGP), cadmium selenide (CdSe), silver thiogallate (AgGaS$_2$), silver selenogallate (AgGeSe$_2$) or gallium arsenide (GaAs) are used, which cannot be pumped by commonly used 1 $\mu$m laser and longer pumping such as at 2 $\mu$m wavelength is required. Very recently, orientation patterned GaAs (OP-GaAs) or OP-GaP are emerging as promising materials. Figure 3.1 presents various technologies used to generate MIR wavelengths covering the spectral range from 2 - 12 $\mu$m.

## 3.2 Optical parametric amplifier

In order to obtain large bandwidth at high energy that is not supported by the gain-bandwidth of a laser medium, a process known as optical parametric amplification (OPA) involving second-order nonlinear effect is used. OPA is a phenomenon in which a high-frequency and high-intensity beam (pump beam at frequency $\omega_3$) amplifies a low intensity and lower frequency beam(signal beam at frequency $\omega_2$) in a second-order nonlinear crystal and a third frequency $\omega_1$ (idler beam) is generated. In this process, a high-frequency photon $\omega_3$ is absorbed by the virtual level of the material and two photons at a lower frequency $\omega_2$ and $\omega_1$ are emitted [42]. Or in other words, energy is transferred from a high intensity, fixed frequency pump beam, to a low intensity, variable frequency seed/signal beam when they interact in a nonlinear medium and a third idler beam is also generated. Hence, an OPA can amplify a broadband weak signal/seed beam by many orders of magnitude making it suitable
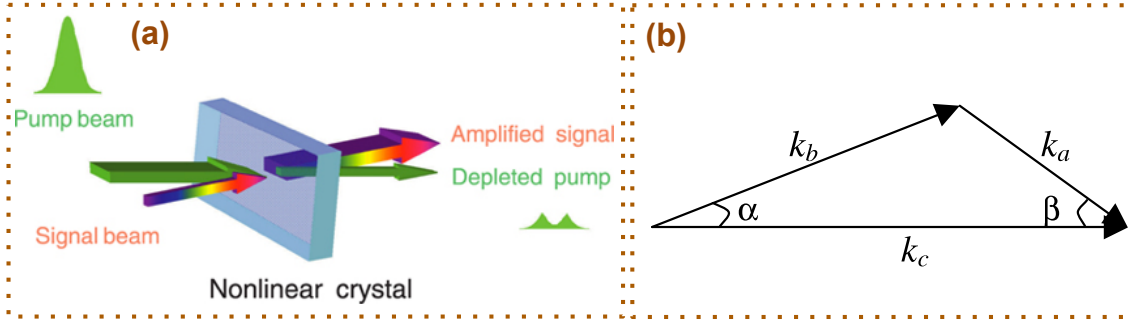
Figure 3.5: (a) Schematic of an optical parametric amplifier with pump & signal beam phase matched in a nonlinear crystal and (b) geometry of a non-collinear phase matching.

for continuously tunable broadband optical amplifier. The frequency conversion satisfies equation 3.1.

$$\hbar\omega_3 = \hbar\omega_1 + \hbar\omega_2 \tag{3.1}$$

$$\hbar k_3 = \hbar k_1 + \hbar k_2 \tag{3.2}$$

### 3.2.1 Theory

To understand the theoretical formulation of an OPA, one needs to solve Maxwell's equation for propagation of waves in a nonlinear medium [43, 44, 42]. If an electric field $E(z,t)$ of a linearly polarized light with a carrier frequency $\omega$ and pulse envelope $A(z,t)$ propagates in z-direction in a nonlinear medium, then the propagation equation can be written as:

$$\frac{\partial^2 E(z,t)}{\partial z^2} - \mu_0 \frac{\partial^2 D(z,t)}{\partial t^2} = \mu_0 \frac{\partial^2 P_{NL}(z,t)}{\partial t^2} \tag{3.3}$$

where $P_{NL}$ is the nonlinear polarization vector, $D$ is the displacement vector and $\mu_0$ is the vacuum permeability. The electric field $E(z,t)$ propagates in the nonlinear medium with a group velocity of $v_g$ whose amplitude varies due to dispersion and the polarization term. In an OPA, there are three beams interacting with each other. Therefore, considering three linearly polarized waves having frequencies $\omega_1$, $\omega_2$ and $\omega_3$ propagating in the nonlinear medium collinearly that satisfy the following conditions:

$$\omega_3 > \omega_2 > \omega_1 \tag{3.4}$$

$$\omega_3 = \omega_2 + \omega_1 \tag{3.5}$$

Then the resulting electric field $E(z,t)$ and nonlinear polarization $P_{NL}$ can be written as:

$$\begin{aligned} E(z,t) =& A_1(z,t)exp[j(\omega_1 t - k_1 z)] + A_2(z,t)exp[j(\omega_2 t - k_2 z)]+ \\ &+ A_3(z,t)exp[j(\omega_3 t - k_3 z)] + c.c \end{aligned} \tag{3.6}$$

$$\begin{aligned} P_{NL} =& 2\epsilon_0 d_{eff} A_1^*(z,t) A_2(z,t) expj[\omega_3 t - (k_1 + k_2)z]+ \\ & 2\epsilon_0 d_{eff} A_2^*(z,t) A_3(z,t) expj[\omega_1 t - (k_3 - k_2)z]+ \\ &+ 2\epsilon_0 d_{eff} A_1^*(z,t) A_3(z,t) expj[\omega_2 t - (k_3 - k_1)z] \end{aligned} \tag{3.7}$$

where $d_{eff}$ is the effective nonlinear coefficient related to tensor $\chi^{(2)}$ with the propagation direction and polarization of the field. Calculating the derivative term $\frac{\partial^2 P_{NL}}{\partial t^2}$ and within slowly varying envelope approximation (SVEA), from equation 3.3, following equations can be derived:

$$\frac{\partial A_1}{\partial z} + \frac{1}{v_{g1}}\frac{\partial A_1}{\partial t} + \frac{1}{2j}D_1\frac{\partial^2 A_1}{\partial t^2} = -\frac{jd_{eff}\omega_1}{c_0 n_1}A_2^* A_3 exp[-j\Delta kz] \tag{3.8}$$

$$\frac{\partial A_2}{\partial z} + \frac{1}{v_{g2}}\frac{\partial A_2}{\partial t} + \frac{1}{2j}D_2\frac{\partial^2 A_2}{\partial t^2} = -\frac{jd_{eff}\omega_2}{c_0 n_2}A_1^* A_3 exp[-j\Delta kz] \tag{3.9}$$

$$\frac{\partial A_3}{\partial z} + \frac{1}{v_{g3}}\frac{\partial A_3}{\partial t} + \frac{1}{2j}D_3\frac{\partial^2 A_3}{\partial t^2} = -\frac{jd_{eff}\omega_3}{c_0 n_3}A_1 A_2 exp[-j\Delta kz] \tag{3.10}$$

where $\Delta k = k_3 - k_2 - k_1$ is known as wave mismatch vector.

Equation 3.8 represents three coupled nonlinear equations and suggests that if the two optical fields are injected into a nonlinear medium, a third field is generated through nonlinear polarization interaction. Due to this interaction two main phenomena arise:

- Sum frequency generation (SFG): In this phenomenon two fields of frequencies $\omega_1$ and $\omega_2$ interact with each other in the nonlinear medium, thereby generating a third frequency $\omega_3$ which satisfies $\omega_3 = \omega_1 + \omega_2$. A special case of this where

$\omega_1 = \omega_2$ is called second harmonic generation (SHG).

- Difference frequency generation (DFG): In this phenomenon two fields of frequencies $\omega_2$ and $\omega_3$ interact with each other in the nonlinear medium, thereby generating a third frequency $\omega_1$ which satisfies $\omega_1 = \omega_3 - \omega_2$. A special case of this, where $\omega_2 = \omega_3$, is called Optical Rectification.

When the strength of the interacting frequencies $\omega_2$ and $\omega_3$ are of comparable intensities then DFG occurs. However, when the strength of the interacting fields are not comparable and the seed beam $\omega_2$ is much weaker than the pump beam $\omega_3$, then OPA occurs. Here, the intense pump beam $\omega_3$ amplifies the signal beam $\omega_2$ by transferring its energy to it and generates an idler beam $\omega_1$. Hence, except for the interacting field intensities, the process of OPA and DFG are quite similar.

Now, by neglecting the pump depletion $A_3 \cong constant$ and assuming an initial signal intensity $A_{20}$ and zero idler intensity i.e. $A_{10} = 0$, if the pump and the signal beam propagate in a nonlinear medium of length $L$, then the above coupled wave equation can be solved for the intensity parametric gain $G$ (for large value of small signal gain $gL \gg 1$):

$$G = \frac{I_2(L)}{I_{20}} = \frac{1}{4}exp(2\Gamma L) \tag{3.11}$$

where, $I_2(L)$ is the signal intensity after the interacting length of $L$ and $I_{20}$ is the initial signal intensity. The nonlinear coefficient $\Gamma$ and the small signal gain $g$ are defined as:

$$\Gamma = \sqrt{\frac{2\omega_1\omega_2 d_{eff}^2 I_3}{n_1 n_2 n_3 \epsilon_0 c^3}} \tag{3.12}$$

$$g = \sqrt{\Gamma^2 - \left(\frac{\Delta k}{2}\right)^2} \tag{3.13}$$

where $n_1$, $n_2$, $n_3$ is the refractive indices at idler, signal and pump wavelength, respectively. $c$ is the speed of light in vacuum, $\epsilon_0$ is the vacuum permittivity and $I_3$ is the pump intensity.

Hence, it is worth noting that within no pump depletion approximation, both signal and idler intensities grow exponentially with pump intensity and an equal number of signal and idler photons are generated. Also, qualitatively this exponential

growth is different from that observed in other second order nonlinear phenomena, like SHG, where the signal grows quadratically. This difference can be understood as following: The seed photon at the signal wavelength in the presence of pump-field, stimulates the generation of an additional photon both at signal and idler wavelength. Similarly, generation of signal photon is simulated by amplification of idler photon due to symmetry. Thus the generation of signal field reinforces the generation of idler field and vice-versa, that gives rise to positive feedback, which is responsible for the exponential growth of the waves. Thus an OPA acts as a real amplifier. However, they have three important differences as compared to the classical laser amplifier:

- It does not store energy

- The gain central frequency is not fixed and can be tunned by varying the phase matching condition

- The gain bandwidth is limited by the phase-matching condition and not by the line-width of the transition.

The coefficient $\Gamma$ depends on the following: 1. Pump intensity 2. Signal and idler wavelengths 3. Nonlinear coefficient $d_{eff}$ 4. Refractive indices at the three interacting wavelength ($\lambda_3$ or $\lambda_p$, $\lambda_2$ or $\lambda_s$ and $\lambda_1$ or $\lambda_i$)

A parameter figure of merit (FOM) is the measure of efficiency of the process involved in any phenomenon. In the case of an OPA, FOM is a measure of the parametric interaction processes involved in a nonlinear crystal that is given by:

$$FOM = \frac{d_{eff}}{\sqrt{\lambda_2 \lambda_1 n_3 n_2 n_1}} \tag{3.14}$$

### 3.2.2 Design consideration

In the previous section general theory of an OPA was discussed. In the following are summarized the important design consideration for an OPA. From the formulation of parametric gain in the previous section, there exist several design criteria;

- $G \propto exp(g)$: Since $g$ depends on $\Delta k$ and is maximum for $\Delta k = 0$, this suggests phase matching is an important condition for gain in an OPA.

- $G \propto exp(d_{eff})$: Since $d_{eff}$ is an intrinsic property of the nonlinear crystal, this suggests that the choice of crystal should be such that it has higher value of $d_{eff}$.

- $G \propto exp(L)$: This suggests that the length of the crystal is also an important factor for parametric gain in an OPA, however, the pulse duration and the group velocities of the interacting pulses restricts the crystal length to an optimum length of interaction in the medium. Also, the damage threshold and the dispersion properties should be taken care off.

- $G \propto exp(\sqrt{I_p})$: Since pump peak intensity depends on pulse duration and pulse energy, it is highly desirable to choose shorter pulse duration and higher pulse energy and at the same time good beam quality is advantageous in order to utilize the entire pump intensities for the conversion process. However, one needs to be careful that the intensity should not high enough to excite other nonlinear phenomena like self-focusing, SPM and the pulse break-up.

- $G \propto exp(\omega_i \omega_s)$: Since the idler frequency depends on the difference of pump and signal frequency, this condition suggests the use higher pump frequencies is advantageous.

***Type-1 and Type-II phase-matching***: The commonly used crystal for femtosecond OPA is negative uniaxial birefringent crystal in which the refractive index of the extraordinary axis is less than that of the ordinary axis ($n_e < n_o$) and the pump is polarized along the extraordinary direction ($e_p$). If the polarization of both signal and idler beam are perpendicular to the pump beam and polarized along the direction of ordinary axis (pump beam is polarized along extra-ordinary direction), then OPA is called Type-I phase-matched ($o_s + o_i \rightarrow e_p$). However, if either of the signal or idler is polarized along the pump direction ($e_s + o_i \rightarrow e_p$ or ($o_s + e_i \rightarrow e_p$) then the OPA is called Type-II phase matched. Depending on the application, Type-I or Type-II phase-matching condition is employed. In general, the application where shortest pulse duration is required, Type-I phase-matching is employed while in the spectroscopic application, where broad tuning range over a narrow bandwidth is required, Type-II phase-matching is employed.

$$\omega_{pe} = \omega_{io} + \omega_{so} \quad || \quad Type - I \tag{3.15}$$

$$\omega_{pe} = \omega_{io} + \omega_{se} \quad || \quad |Type - II \tag{3.16}$$

$$\omega_{pe} = \omega_{ie} + \omega_{so} \quad || \quad Type - II \tag{3.17}$$

where $\omega_{pe}$, $\omega_{se}$ and $\omega_{ie}$ are the pump, signal and idler frequencies respectively along extraordinary axis. $\omega_{so}$ and $\omega_{io}$ are the signal and idler frequencies respectively along ordinary axis.

For Type-I phase-matching, using simple mathematics, the phase matching angle $\theta_m$, that is angle between the wavevector of the propagating beam and optical axis of the nonlinear crystal, can be derived as:

$$\theta_m = arcsin \left[ \frac{n_{ep}}{n_{ep}{}^*} \sqrt{\frac{n_{op}^2 - n_{ep}{}^{*2}}{n_{op}^2 - n_{ep}^2}} \right] \tag{3.18}$$

where $n_{ep}$ and $n_{op}$ are the refractive indices along extraordinary and ordinary axis at pump frequencies.

***Group velocity mismatch (GVM)***: In the above formalism, it is assumed that the waves are monochromatic, however for a real OPA case, the waves are not monochromatic. Hence, similarly, the above formalism can also be treated for an ultrashort pulses having multiple wavelengths. It can be proved that the main limiting factor with such pulses is the group velocity mismatch (GVM), defined as the difference between the group velocities of the interacting pulses. Since the signal and the idler, in this case, travel with different group velocities, parametric interaction stops as soon as the pulses separate from each other temporally. The length after which the parametric amplification stops is called pulse splitting length and hence the crystal thickness used in OPA should not be more than the pulse splitting length. The pulse splitting length can be derived as:

$$l_{sp} = \frac{\tau}{\delta_{sp}} l_{ip} = \frac{\tau}{\delta_{ip}} \tag{3.19}$$

where $\tau$ is the pump pulse duration and $\delta_{jp} = 1/v_{gj} - 1/v_{gp}$ is the GVM between the pump and the signal/idler where $v_g$ is the group velocity.

Since the interaction length depends on the pump pulse duration, an OPA with
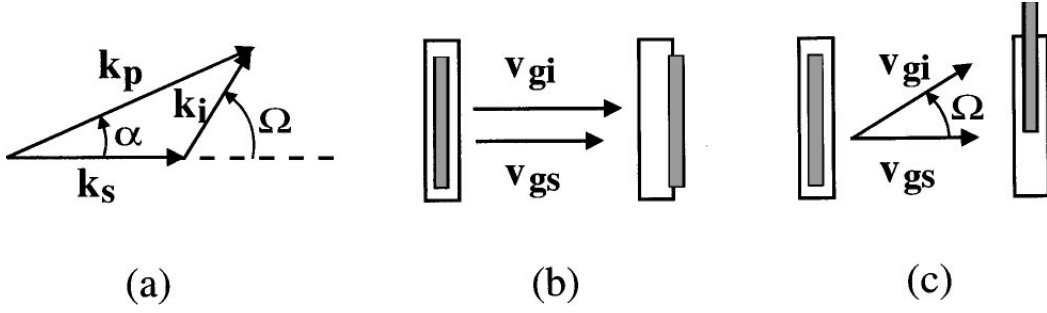
Figure 3.6: (a) Parametric interaction of a non-collinear geometry, (b) representation of signal and idler pulses for collinear geometry and (c) for non-collinear geometry

shorter pump pulse duration requires shorter crystal as compared to that with longer pump pulse duration. In particular, GVM between the pump and amplified beam (signal or idler) limits the usable length of the crystal while GVM between the signal and idler limits the phase-matching bandwidth. GVM depends on the dispersion of crystal or in turn depends on the crystal type, pump wavelength and the type of phase matching. For example, for a BBO based OPA, for a pump wavelength ($\lambda_p$) of 0.4 $\mu$m (left) and 0.8 $\mu$m (right), due to large dispersion at 0.4 $\mu$m, GVM affects the limiting thickness stronger as that compared at 0.8 $\mu$m. GVM effects can be neglected if the crystal thickness is shorter than pulse splitting length, however, if the thickness is larger that the pulse splitting length, then GVM plays a crucial role, and the temporal walk-off must be calculated. For a specific case when $\delta_{sp}\delta_{ip} > 0$, it implies that both signal and idler walk away in the same direction, with respect to the pump, and the gain decreases rapidly as the propagation distance exceeds the pulse splitting length while, if $\delta_{sp}\delta_{ip} < 0$, it implies that signal and idler move in opposite direction with respect to the pump thereby localizing both signal and idler still under the pump pulse preserving the exponential growth of the gain even for longer propagation distance than the pulse splitting length.

*Gain bandwidth*: Under large gain approximation, the bandwidth over which maximum gain exists (GBW) can be derived as:

$$GBW = \frac{2(ln2)^{1/2}}{\pi}\left(\frac{g}{L}\right)^{1/2}\frac{1}{|\frac{1}{v_{g2}} - \frac{1}{v_{g1}}|} \tag{3.20}$$

*Collinear and non-collinear OPA* In an OPA for a given pump and signal wavelength, two configurations can be used to achieve phase matching condition $\Delta k = 0$; Collinear and non-collinear geometry. In collinear geometry, the group

velocities of the signal and idler are fixed and hence (as seen in the equation 3.2.14), the phase-matching bandwidth is also fixed. Due to the different group velocities of the signal and idler, the pulses get quickly separated giving rise to pulse lengthening which in turn limits the bandwidth. Thus to obtain shorter pulse and broader bandwidth, non-collinear geometry is advantageous where an additional degree of freedom can be introduced as shown in the figure 3.6 [42]. In this configuration, the pump, signal, and idler all propagate in the different directions. Therefore, the projection between the group velocities can be chosen such that at a certain angle $\alpha$, the group velocities of the signal and idler are equal, and the idler wave is emitted at an angle $\Omega$ with respect to the signal. Thus, the pulses can stay temporally overlapped for longer distances. In this case, the phase-matching condition can be described as:

$$\Delta k = k_p \cos \alpha - k_s - k_i \cos \Omega = 0 \tag{3.21}$$

$$\Delta k = k_p \sin \alpha - k_i \sin \Omega = 0 \tag{3.22}$$

It is to be noted that the angle $\Omega$ is not fixed and depends on signal wavelength. Furthermore, if the signal frequency increases by $\Delta\omega$, then the idler frequency decreases by $\Delta\omega$ and the following relation can be derived:

$$v_{gs} = v_{gi} cos\Omega \tag{3.23}$$

It is to be noted that, the phase matching can be achieved in non-collinear geometry only if $v_{gi} > v_{gs}$

The angle $\Theta$ between the pump and signal is given by:

$$\Theta = arcsin \left( \frac{1 - \frac{v_{gs}^2}{v_{gi}^2}}{1 + \frac{2v_{gs}n_s\lambda_i}{v_{gi}n_i\lambda_s} + \frac{n_s^2\lambda_i^2}{n_i^2\lambda_s^2}} \right)^{1/2} \tag{3.24}$$

In general, the parametric interaction differs largely for various nonlinear crystal having different $d_{eff}$ at different interacting wavelengths and with the pump & seed angle in non-collinear geometry [42]. Furthermore, FOM reduces with a longer wavelength and therefore the parametric gain reduces at the longer wavelength. Such design details are to be considered while designing an efficient and cost-effective
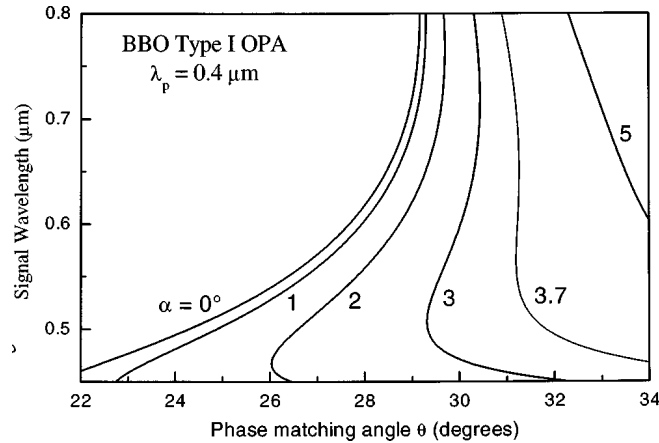
Figure 3.7: Phase-matching curves for a non-collinear type-I OPA as function of pump signal angle $\alpha$ (figure taken from [3])

OPA, since the cost of the nonlinear crystal can increase drastically with slight increase in the thickness. Furthermore, in figure 3.7, phase matching angles $\theta_m$ as function of signal wavelength for different pump-signal angle ($\alpha$) in non-collinear geometry in BBO, are shown. It can be seen that for $\alpha = 0°$, $\theta_m$ shows the strong dependence on the signal wavelength, thus for a fixed crystal orientation, phase matching can be achieved for a narrow signal range. However, with increase in $\alpha$, the dependence on the signal wavelength becomes weaker and becomes optimum for $\alpha = 3.7°$ where phase matching is possible over ultrabroad bandwidth from 0.5 to 0.75 $\mu$m. The nonlinear conversion process often exhibit complicated features in spectral and intensity distribution and hence the gain evolution during parametric amplification can strongly vary different geometries.

Thus the design of an OPA consists of mainly three parts:

- Choice of the nonlinear crystal

- Pump Source

- Seed Source

### 3.2.3 Nonlinear crystal

Due to the limitation of the transparency window, the commonly used oxide crystals for NIR OPA, cannot be used for generation of long wavelength MIR pulses in MIR OPA. Hence, most MIR OPAs use non-oxide crystals for parametric amplification. In the table 3.1, a comparison of commonly used nonlinear crystals for MIR OPA

Table 3.1: Comparison of various non-oxide crystals for MIR OPA

| Crystal | Transparency ($\mu$m) | $d_{eff}(pm/V)$ | Bandgap (eV) | Birefrin- gence | Remark |
|---------|----------------------|-----------------|--------------|-----------------|--------|
| $ZnGeP_2$ | 1.8-11 | 70 at 5.3 | 2 | Yes | - |
| $CdSiP_2$ | 0.5-9 | 84.5 at 4.5 $\mu$m | 2.45 | Yes | - |
| MgO:PPLN | 0.3-5 | 17 at 1 $\mu$m | 4 | Yes | - |
| KTA | 3.7-4.1 | 16.2 at 4 $\mu$m | - | Yes | |
| $AgGaSe_2$ | 0.75-15 | 58 at 1 $\mu$m | 1.77 | Yes | Low Damage threshold |
| $AgGaS_2$ | 0.5-11.4 | 13.7 at 2.5 $\mu$m | 2.7 | Yes | Low Damage threshold |
| GaSe | 0.8-14 | 70-90 | 2.1 | Yes | z-cut only |
| GaAs | 1.6-17 | 119 at 1.5 $\mu$m | 1.4 | No | - |

are presented. From the table we see that GaAs exhibits highest $d_{eff}$ of 119 pm/V with maximum transparency window of 1.6 - 17 $\mu$m. However, it also does not have natural birefringence and hence for better phase matching, very recently orientation-patterned crystals have been developed [36] but with limited apertures. Apart from that ZGP and CSP crystals exhibit high $d_{eff}$ of 70 and 84.5 pm/V, respectively which also exhibits birefringence and can be produced with large apertures sizes [36]. Hence they are quite beneficial for nonlinear parametric interaction for MIR OPAs. However, despite the variety of advantages for these crystals, the MIR OPAs until now, could not be very well developed as the NIR OPAs, due to lack of commercial pump source for these crystals. These crystals come with the drawback that they require pumping at a long wavelength, for instance at 2 $\mu$m. It is for this reason, in this work there exists a challenge for the development of the pump source as well.

### 3.2.4   Simulations

As discussed in the previous section, $ZnGeP_2$ or simply ZGP have immense benefits as compared to other non-oxide crystals:

- Wide transparency window ranging from 1.8 - 11 $\mu$m

- High nonlinear coefficient ($d_{eff}$)

- High damage threshold

- Availability in large size
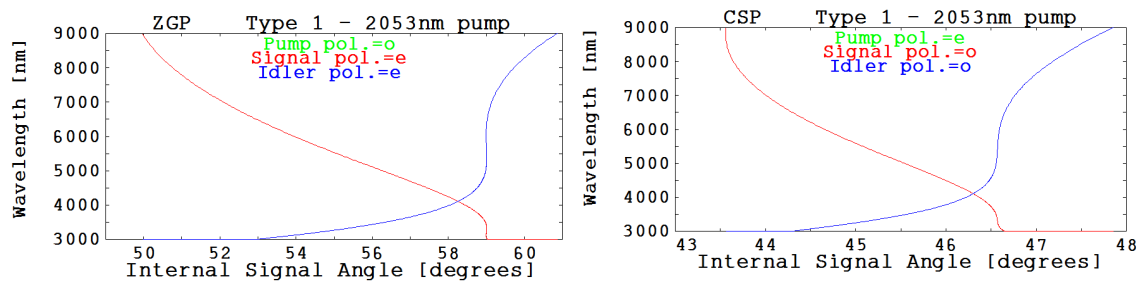
Figure 3.8: (a) Type-I Phase matching curve for nonlinear parametric interaction in (a) ZGP and (b) CSP pumped at 2053 nm

It is for these reasons, it is one of the most widely used crystal, especially, with the recent advancement in the manufacturing of large ZGP crystals. In the figure 3.8, the phase-matching curves for ZGP and CSP crystal obtained using open source software SNLO are shown. The simulation is based on Type-I phase-matching and the pump wavelength is at 2053 nm. The curve suggests that the broadest phase-matching bandwidth can be achieved for an angle of of 59°and 46.6°for ZGP and CSP, respectively.

### 3.2.5   Pump Source

For MIR OPA, due to lack of available proper pump source at 2 $\mu$m, the pump development was an added challenge. Gain medium is the most important part of a laser cavity, and one needs to choose the material carefully taking into account the application and their related properties. $Tm^{+3}$ and $Ho^{+3}$ are the most commonly used dopant for lasing at 2 $\mu$m with YLF and YAG as the common host. The important parameters one need to consider for any solid-state lasers are:

**Energy storage time**

Higher energy storage time in the upper-level allows longer delivery time of the optical pump energy to the output pulse, allowing to achieve higher output pulse energy and amplification.

**Transition metal and lanthanide series**

Most laser gain media are either transition ions or lanthanide ions. In transition ion lasers, the $4s$ and $4p$ levels are completely filled and $3s$ electrons participate in laser

transitions that are strongly exposed to the electric field of the crystal. This makes the laser transitions vibronic in nature thereby emitting a phonon simultaneously with the emission of a photon, and due to wide phononic transitions, the emission spectrum is very broad. However, this is not the case for lanthanide series, where $4f$ levels participate in laser transition and $5s$ and $5p$ are completely filled. Thus the electric field of the crystal has a weak effect on the $4f$ level electrons resulting in narrow absorption and emission. Moreover, due to the wide linewidth of transition ion laser, they have small emission cross-sections or short upper-level lifetimes whereas lanthanide series lasers have larger emission cross-sections or upper-level lifetime.

**Quantum efficiency**

Quantum efficiency (QE) is the probability of an atom being produced in the upper level by non-radiative transitions of an absorbed photon. It is not always necessary that for each absorbed photon an atom is produced in the upper level as it can bypass to some lower level by radiative decay. The QE denoted by $\eta_Q$ is given by:

$$\eta_Q = \frac{1/\tau_{NR}}{1/\tau_{NR} + 1/\tau_{RAD}} \tag{3.25}$$

where $\tau_{NR}$ and $\tau_{RAD}$ are the pump non-radiative and radiative decay lifetimes respectively.

### 3.2.6 Comparison of various gain media at 2 $\mu$m

The most common dopants for lasers operating in the 2 $\mu$m wavelength range are trivalent rare earth ions Tm$^{+3}$ (thulium) and Ho$^{+3}$ (holmium). Table 3.2 shows various Tm and Ho-doped host materials like YLF, YAG, Sc$_2$O$_3$, Lu$_2$O$_3$, Y$_2$O$_3$ etc, used as gain medium with their important material properties. It can be seen that Ho-doped crystals show larger absorption and emission cross-sections and support large gain-bandwidth ($\sim$25 nm) due to their $^5I_7 \rightarrow \ ^5I_8$ transitions. Moreover, the underlying strong absorption band around 1.9 $\mu$m pulses allows in-band pumping from commercial Tm-fiber lasers. The development of Tm-doped lasers, which can be efficiently pumped using commercial diodes, has accelerated recently, but they suffer from the low quantum efficiency. Recently, generation of sub-ps pulses below the mJ level from a Tm:YAP regenerative amplifier (RA) was demonstrated [45].

Table 3.2: Comparison of various gain media at 2 $\mu$m wavelength

| Crystal | $\lambda_{abs}$ (nm) | $\lambda_{em}$ (nm) | $\sigma_{abs}$ $\times 10^{-21}$ $cm^{-2}$ | $\sigma_{em}$ $\times 10^{-21}$ $cm^{-2}$ | $T_c$ $(Wm^{-1}K^{-1})$ | $\tau$ (ms) | $n_2$ $(\times 10^{-20})$ $(m^2/W)$ |
|---|---|---|---|---|---|---|---|
| Ho:YLF ($\pi$) | 1940 | 2051 | 11.9 | 18.4 | 6.3 | 15 | 1.7 |
| Ho:YAG | 1907 | 2098 | 7.5 | 1.2 | 13 | 7 | 8.1 |
| Ho:YAP | 1940 | 2100 | 6 | 8.2 | 11 | 4.8 | - |
| Ho:Sc$_2$O$_3$ | 1992 | - | 5 | 8.4 | 17 | 4 | - |
| Ho: Lu$_2$O$_3$ | 1945 | 2070 | 3.8 | 2.3 | 13 | 10 | - |
| Tm:YLF ($\pi$) | 790 | 1940 | 6.5 | 4 | 6 | 14 | - |
| Tm:YAG | 785 | 2010 | 7.5 | 2.2 | 13 | 9 | - |
| Tm:YAP | 793 | 1940 | 8.6 | 4.33 | 11 | 4 | - |
| Tm:Sc$_2$O$_3$ | 796 | 1990 | 4.5 | 8.4 | 17 | 4 | - |
| Tm:Lu$_2$O$_3$ | 796 | 1990 | 3.8 | 9.8 | 13 | 4 | - |
| Tm:Y$_2$O$_3$ | 796 | 1990 | 5 | 8.8 | 14 | 4 | - |
| Tm:LuAG | 788 | 1960 | 5.4 | 1.6 | 13 | 15 | - |

Moreover, among Ho-doped media, Ho:YLF and Ho:YAG are preferred gain media at 2 $\mu$m for high-energy amplifiers. Recently, there have been several demonstrations of mJ-level, ps-amplifiers based on Ho:YAG and Ho:YLF gain medium. In the figure 3.9, it can be seen that the absorption and emission of Ho:YLF is higher than Ho:YAG. Moreover, the Ho:YLF have larger upper-level lifetime that helps in storing pump energy for a longer duration in the upper level and much lower nonlinear refractive index that helps to avoid accumulation of B-integral.

Hence, in this work we preferred Ho:YLF as the gain medium for the pump source development over Ho:YAG. The advantages of Ho:YLF over Ho:YAG include:

- Natural birefringence that allows generation of linearly polarized light

- Two times lower $dn/dT$ that results in weak thermal lensing

- Two times lower nonlinearity

- Lower quantum defect

- Two times longer upper-level lifetime

- Higher absorption and emission cross-section
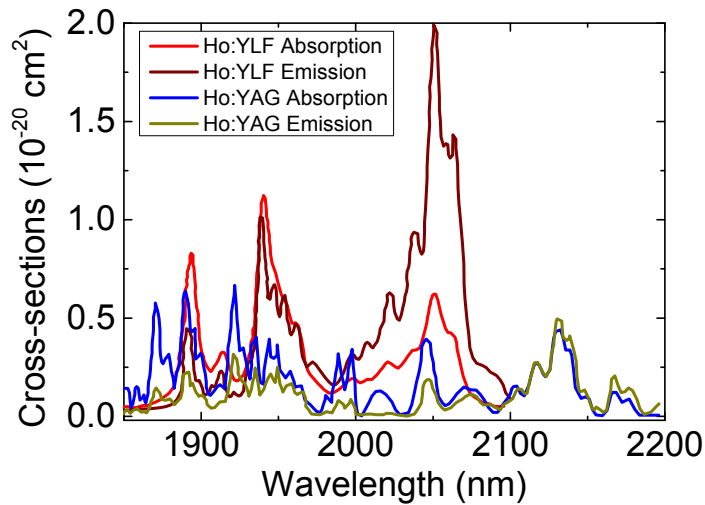
Figure 3.9: Absorption and emission cross-sections of Ho:YLF and Ho:YAG for a p-polarized pump

### 3.2.7   Seed Source

Since the seed beam for an OPA is at a different frequency than the pump beam, a separate nonlinear process is often utilized for its generation. The three common methods for this purpose are:

- Parametric superfluorescence: This is a parametric amplification of the vacuum or quantum noise. Conversely, this is a two-photon spontaneous emission from a virtual level excited by the pump field. The amplification of the noise frequencies is achieved by pumping a nonlinear crystal (usually same as that to be used in OPA stage) at those frequencies for which parametric interaction is phase-matched. However, it has its own pros and cons on the output seed pulse. The advantage is that large amplification thereby higher seed energies are possible but due to the process arising from the noise, higher inherent fluctuations are present with a poor spatial beam quality.

- White-light continuum generation: When an intense ultrashort pulse is focused into a transparent medium, the spectrum of the input pulse undergoes large spectral broadening resulting from the interplay between self-focusing and self-phase modulation. This is one of the most common processes utilized for seed generation for an OPA. With careful consideration of the material and focusing conditions, white light has an excellent spatial beam quality with high pulse-to-pulse stability.
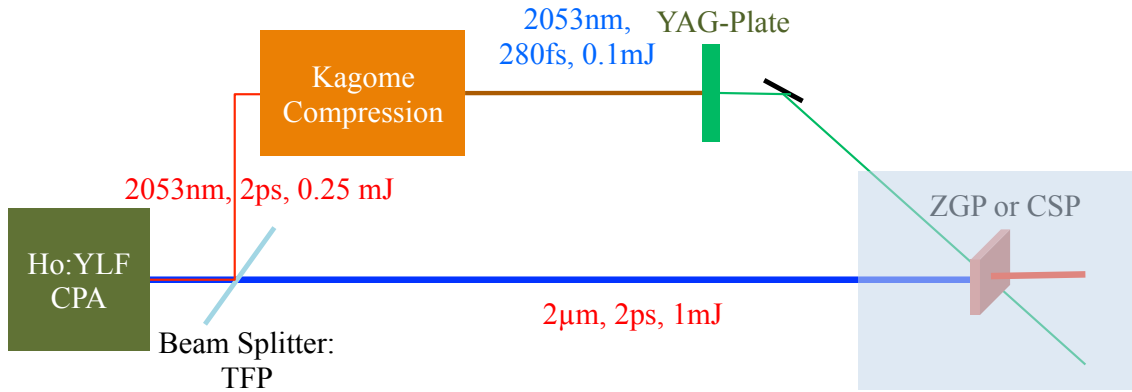
Figure 3.10: Experimental layout for MIR OPA

- Difference frequency generation: In this method, new frequencies are generated by the difference between optical pump frequencies. There exist cascade phenomena between each new frequencies generated, however, their efficiency drops after the generation of each new frequency.

Thus, the front-end for MIR OPA consists of two parts. One is pump and the other is seed source. After the development of the pump source, a small part of the pump can then be later used for seed generation using one of the methods mentioned above. The proposed schematic for the MIR OPA utilizing the pump and seed source is developed in this work is shown in the figure 3.10. The small part of the energy from the Ho:YLF pump chain can be used for SC generation. However, due to long picosecond duration of the pump pulse, they cannot be directly used for SC generation for reason which will be seen Chapter 7. Hence, an external nonlinear compression scheme is employed to first compress the picosecond pulses to femtosecond regime and then these pulses are used to generate white light SC as a seed for OPA.

## 3.3 Conclusions

OPA is the technique to generate ultrabroad high energy pulses. ZGP is the commonly used to nonlinear crystal for parametric amplification which requires pumping at $2~\mu$m wavelength. Hence, first a high energy pump source needs to be developed. Among various Tm and Ho-doped gain media, the Ho:YLF gain medium is found to be very suitable for high-gain amplifiers especially due to its high absorption and emission cross-sections and upper-level lifetime. Hence, in this work, we consider

Ho:YLF gain medium as the amplifying medium in the pump-chain.

# 2 Micron Laser Oscillator

High energy ultrashort pulses can be generated in two steps; first a laser oscillator generates low-energy ultrashort pulses, that is then amplified to high-energy using a laser amplifier. In a laser cavity, due to population inversion in the gain medium, the lasing action occurs. The radiation inside the laser cavity bounces back and forth and interferes constructively and destructively to give rise to a large number of axial or longitudinal modes oscillating in a random direction independent to each other. Ideally, for a continuous wave (CW) case, they interfere such that the power remains constant. In the figure 4.1, interference of few cavity modes are shown. When these modes are forced actively or passively to oscillate with a fixed relation, the laser operates in pulsed operation and is said to be modelocked. Modelocking phenomenon was developed back in the 1980s and is widely used as state-of-art for generating ultrashort laser pulse in the order of ps ($10^{-12}$) to fs ($10^{-15}$) duration. Modelocking is a resonant phenomenon in which multiple axial modes of the laser cavity are locked in the same phase so that the superposition of all the modes represents a pulse with spatial extent much shorter than the cavity. This process is best understood in the time domain. Initially, the pulse is initiated by the weak modulation arising from the roundtrip time of the laser radiation circulating in the cavity which can be made to get shorter with each pass in the resonator cavity. The pulse shortening process continues till the pulse gets so short, that the corresponding spectrum is limited by the gain bandwidth of the
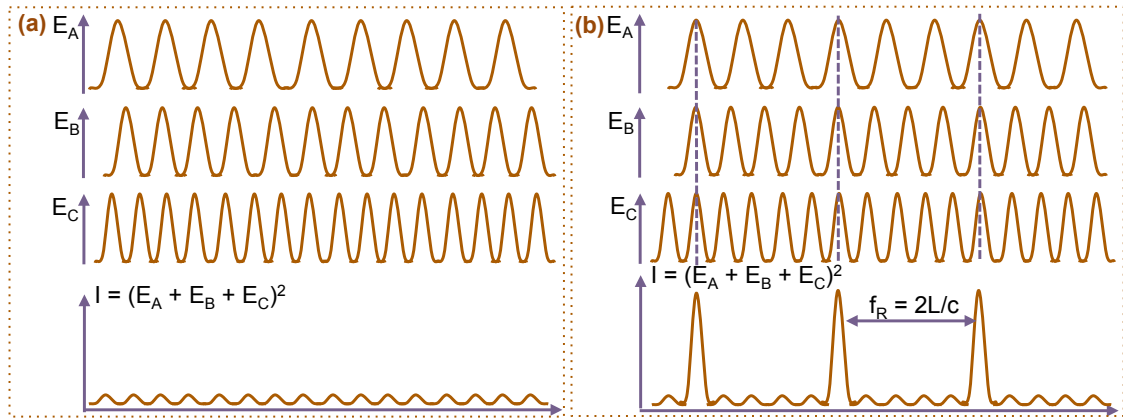
Figure 4.1: Operation of a laser having (a) constant CW output and (b) pulsed output with intense power burst separated by the cavity round-trip time.

laser crystal or the bandwidth of the optical components, or other pulse lengthening process starts [46]. When the gain level in a laser cavity is above its threshold, several axial modes lases in random phase whose central mode is denoted by $\omega_0$ separated by $\Delta\Omega = 2\pi/T_R$, where $T_R$ is the cavity round trip time. Modelocking is achieved by introducing a loss modulator in the cavity which in turn modifies the effective gain in the cavity. The loss modulator can be active or passive. When the loss is modulated by an external device like acousto-optic modulator by applying an external voltage then it is called active modelocking. Whereas if the loss modulation is achieved using a passive device i.e. the optical component in the cavity itself like saturable absorber where the pulse itself acts as a modulator is called as passive modelocking.

In the previous chapter, the need for high energy 2 $\mu$m wavelength laser source was discussed. It was seen that such lasers are an important tool for pumping of non-oxide crystals in OPA for generating long MIR wavelength. A general comparison of various Tm and Ho-doped gain media at 2 $\mu$m were discussed. In this chapter, the generation of low-energy laser pulses from a laser oscillator is discussed. Different modelocking techniques for generation of ultrashort pulses are discussed. First, the theory of modelocking are explained in general, and then active & passive modelocking techniques are discussed. In particular, the development of solid-state Ho:YLF oscillator to generate stable modelocked pulses is presented. Finally, the experimental and simulation results obtained are presented. These pulses are then amplified to high-energy using a laser amplifier, whose results are presented in the next chapter.
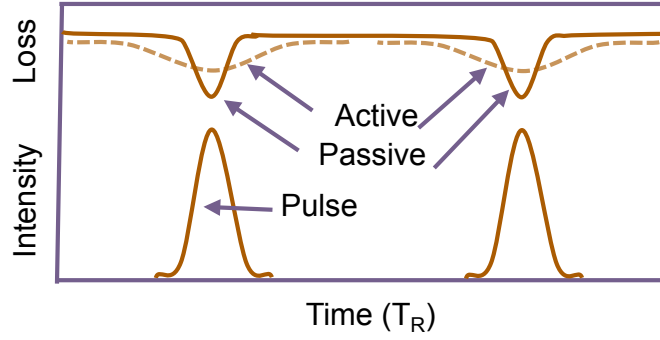
Figure 4.2: Loss modulation in active and passive modelocking scheme. In both the cases, loss introduced is smaller, which opens a net gain window for the pulse.

## 4.1   Modelocking mechanisms

The electric field at a certain point in the space in a laser cavity can be written as the superposition of each monochromatic waves. i.e.

$$\tilde{E}(t) = \frac{1}{\sqrt{2\pi}} \int_{-\infty}^{\infty} E_A(\omega) exp[-i(\omega t + \phi(\omega))]d\omega \qquad (4.1)$$

where $E_A(\omega)$ is the amplitude and $\phi(\omega)$ is the phase offset of the oscillating modes.

This implies that the pulse duration can be altered by changing $E_A(\omega)$ or $\phi(\omega)$. Thus a pulse propagating in a medium that influences either $E_A(\omega)$ though absorption/amplification or $\phi(\omega)$ though the spectral bandwidth of the pulse, pulse duration can be changed. It can also be changed by introducing a frequency dependent path difference. There are two different methods to obtain modelocking i.e. Active and Passive modelocking whose loss dynamics are shown in figure 4.2.

### 4.1.1   Active modelocking: based on active loss modulator

In the case of active modelocking, the loss modulation required for modelocking is achieved by a device which is controlled actively, for example, acousto-optic modulator. The pulse width of the pulses obtained is inversely proportional to the fourth root of the modulator strength, hence it is limited to the speed of electronic signal generator and therefore the curvature of the modulation can never be very strong. The loss modulation achieved using an acousto-optic modulator in a laser cavity is given by $q(t) = M(1 - cos(\omega_M t))$, where $M$ is the modulation depth and

$\omega_M$ is the modulation frequency which needs to be precisely tuned to the resonator round-trip time $2\pi/T_R$ and is shown in the figure 4.2. Due to the tight focusing of the pulses in the gain medium, there also exist nonlinear interaction self-phase modulation which introduces positive chirp to the pulse, that further shorten the pulse and can drive the pulse unstable if it increases beyond a certain level. In order make the system stable, additional second order dispersion needs to be present that can compensate for chirp, present in the system and can lead to soliton formation. The complete analysis requires solving the master equation in the presence of gain medium, self-phase modulation (SPM) and group velocity dispersion (GVD) and can be found in detail in Ref. [46]. Without going into the complete analysis, it can be derived that for large dispersion, the pulse reduction values obtained due to active modelocker, scales with the fourth root of normalized dispersion [4]. This indicates that large negative dispersion is required to maintain stable soliton while suppressing the continuum. This is due to the fact that gain filtering and active modelocker continuously sheds energy from the soliton to the continuum. However, the continuum viewed as the background pulse, does not experience SPM and hence is spread due to GVD. This long continuum, then suffers a much higher loss in the modulator and conversely reduced gain in the gain medium as compared to the short soliton and makes the soliton stable as long as the continuum, and sees less round trip gain than the soliton. It can be derived that the minimum pulse width possible ($\tau_{min}$)in the case of active modelocking is given by:

$$\tau_{min} = \sqrt[6]{\frac{2D_g^2}{9\phi_0 M_s}} \tag{4.2}$$

where, $D_g$ is the curvature of the gain at the maximum of the Lorentzian profile, $M_s$ is the loss modulation, $\phi_0$ is the nonlinear phase shift per round-trip.

The main points related to active modelocking can be summarized as follows:

- The pulse width is proportional to fourth root of the loss curvature.

- The loss curvature in an active modelocking case, can never be very strong as the modulation is limited by the speed of electronics.

- The pulse shortening depends on the $12^{t}h$ root of the dispersion, hence the shortening depends mostly on the gain bandwidth of the material.
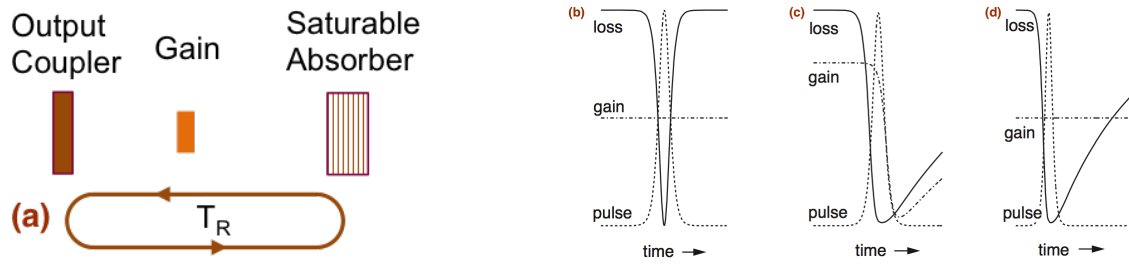
Figure 4.3: (a) Laser cavity with gain medium and saturable absorber. (b) Dynamics of modelocking using slow saturable absorber. Pulse shaping and stabilizing mechanism in passive modelocking, owing to the gain and loss modulation using (c) fast absorber, (d) slow absorber (combination of gain and loss saturation) and (e) soliton formation with a slow absorber in the presence of both SPM and dispersion [4].

## 4.1.2 Passive modelocking: based on saturable absorber

In the case of passive modelocking, the pulse itself modulates the absorption in the cavity, thereby the curvature of the modulation can be very strong, making the net gain window as short as the pulse itself, resulting in a much shorter pulse than that generated in an active modelocking case. Most of the ultrashort laser pulses today are generated using passive modelocking. A saturable absorber is often used for passive modelocking and depending on the ratio of absorber recovery time and the final pulse width, different regimes of operation are defined for the steady state pulse formation as shown in the figure 4.3. These operation regimes also influence the pulse build-up and the pulse instability with respect to Q-switching. The operation regimes can be fast, slow or soliton regime.

If the saturable absorber opens and closes the net gain window, just before and after the pulse, then such absorber is called fast saturable absorber whose recovery time is fast enough so that it can be compared to the pulse duration (figure 4.3 (b)). For example, in solid state laser where the effect of gain saturation per pulse can be neglected, since the saturation energy is much higher than the intracavity energy, a fast absorber is required. The gain in these lasers only saturates with average power. However, in the case of semiconductor lasers where the intracavity energy exceeds the saturation energy, slow absorbers are useful. If the absorber is allowed to bleach faster than the gain medium (for example, by tightly focusing the beam on absorber compared to gain medium) thereby opening the net gain window and closes later with the pulse itself with a saturation of the gain (figure 4.3 (c)). This mechanism is referred as slow absorber modelocking. There exists a third case of

soliton modelocking where a significant net gain window is opened after the pulse (figure 4.3 (d)) and sub-picosecond pulses can be generated using a slow absorber with a recovery of few *ps*. Such pulses can be stable up to a certain limit in the presence of strong soliton formation where the solitary pulse formation occurs due to the presence of SPM and GVD which shapes the pulse to sech-shape pulse despite the open net gain window. From the master equation approach, for the pulse evolution in slow absorber, following relation can be derived:

$$\frac{1}{\tau^2} = \frac{\Omega_f^2 W^2}{8} \left( \frac{q_0}{E_A^2} - \frac{g_i}{E_L^2} \right) \tag{4.3}$$

where $\Omega_f$ is related to the gain bandwidth of the gain medium in terms of dispersion and denotes the filtering action of the medium. $E_A$ and $E_L$ is the saturation energy of the absorber and the gain medium, respectively. $g_i$ is the initial small signal gain and $q_0$ is the non-saturable loss coefficient.

This equation suggests that $q_0$ should be more than $g_i$ that implies that the saturable absorber should saturate more strongly than the gain medium in order to open a net gain window. However, in most solid-state lasers, the intracavity pulse energy are much lower than the saturation energy of the gain medium and a fast absorber is required in order to open a net gain window whose response can be written as:

$$q(A) = \frac{q_0}{1 + \frac{|A|^2}{P_A}} \tag{4.4}$$

Thus there exists essentially three operation regimes: (1) Without GVD and SPM, the pulse are always stable, (2) strong soliton-like pulse shaping arising from GVD and SPM i.e. $\delta_n >> 1$ and $-D_n >> 1$, the chirp is always much smaller than the positive dispersion and the pulses are soliton-like and (3) if $\delta_n = -D_n$, then the pulse is chirp-free. In the case of strong soliton-like pulse shaping, the absorber doesn't have to be fast, as the pulse is shaped by GVD and SPM and the role of absorber is only to stabilize the soliton against continuum. This regime is called soliton modelocking.
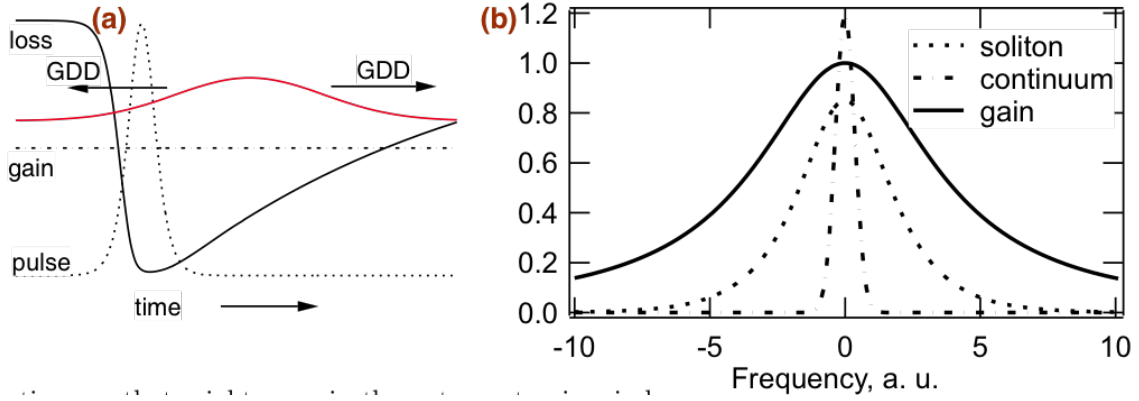
Figure 4.4: (a) The continuum that grows in the open net gain-window, follows the pulse and is spread by dispersion into the regions of high absorption, (b) normalized gain, soliton and continuum. The continuum is the long pulse exploiting the peak of the gain [4].

### 4.1.3 Soliton modelocking

In soliton modelocking, the pulses are modelocked in the presence of strong soliton-like pulse shaping. In these lasers, the absorber does not need to be fast (as seen in figure 4.3) because the pulse is shaped by GVD and SPM and the absorber itself has to stabilize the soliton pulses against instabilities like continuum formation. As can be seen in the figure 4.3 (c), the pulse experiences loss during the saturation of the absorber and the filter losses and in steady state, the saturated gain equals these losses. The loss experienced by the continuum $l_c$ must be higher than the those experienced by soliton to keep it stable [47]. The master equation can be written as:

$$T_R \frac{\partial A(T,t)}{\partial T} = \left[ g(t) + D_f \frac{\partial^2}{\partial t^2} + jD \frac{\partial^2}{\partial t^2} - l - j\delta |A|^2 - q(T,t) \right] A(T,t) \quad (4.5)$$

The response of the slow saturable absorber is described by separate differential equation

$$\frac{\partial q(T,t)}{\partial t} = -\frac{q - q_0}{\tau_A} - \frac{|A(T,t)|^2}{E_A} \quad (4.6)$$

where, $q_0$ is the non-saturable loss, $P_A = E_A/\tau_A$ is the saturation power, $E_A$ is the saturation energy of the absorber and $\tau_A$ is the recovery time. In this case, the pulse shaping due to soliton effects are much larger than the pulse shaping due to the

gain filter and the saturable absorber, hence the steady state pulse will be similar to that in the active modelocking case discussed above, where in steady state, there exists a soliton-like pulse and a continuum. The solution of the master equation can be derived as:

$$A(T,t) = \left( A sech \left( \frac{t}{\tau} + a_c(T,t) \right) \right) exp \left( -j\phi_0 \frac{T}{T_R} \right) \qquad (4.7)$$

The continuum is a long pulse that competes with the soliton for the available gain and in the frequency domain, it has a broad spectrum (as seen in the figure 4.4). Thus the continuum spectrum experiences more gain as compared to the soliton. This extra gain has to be compensated by the absorber response. In a steady state, there exists a balance between the nonlinearity and the dispersion for soliton to exist, but that is not the case with the continuum and thus it undergoes lengthening due to dispersion in the region of high absorption. If the soliton becomes too short as compared to the continuum i.e. too long net gain window arises, the loss of the continuum can be lower than the loss of the soliton (as seen in the figure 4.4) and the continuum can destroy the single soliton. Roughly, the absorber recovery time should not be more than 10 times the pulse width for a stable pulse formation. Since the pulse is continuously phase shifted due to the Kerr-effect, to maintain the stable shape of the soliton, there exists a soliton area theorem given by:

$$|A_0|\tau = \sqrt{2|D|/\delta} \qquad (4.8)$$

where, $\tau$ is the pulse duration, $D$ is the net dispersion, $\delta$ is the net nonlinear phase shift.

Saturable absorber action can be generated using an artificial absorber like Kerr-lens modelocking (KLM) and additive pulse modelocking or real absorbers like semiconductor saturable absorbers (SESAM). In the following section, the most commonly used method of KLM and SESAM are discussed.

### 4.1.4  Artificial absorber: Kerr-lens modelocking

The first femtosecond laser pulse was obtained by KLM, founded by Sibbet and colleagues in 1990. KLM is a non-resonant nature of saturable absorber which is inherently broadband than any other saturable absorber. In KLM type modelocking,

a soft or hard aperture is placed in the laser cavity to assist modelocking. Due to nonlinear refractive index, not only SPM occurs but also self-focusing takes place, which depends on the intensity of the pulse. Thus, there exists a time-dependent mode size variation in the cavity due to self-focusing. If a hard aperture is placed in the cavity, it strips out the wings of the pulse spatially, that effectively leads to its shortening. This has the same effect as that of a saturable absorber in the cavity. However, instead of the hard aperture, the gain medium itself can act as the soft-aperture as the self-focusing leads to change in mode size that eventually leads to increased gain (instead of that arising from saturable absorber). However, to have a better sensitivity of the mode size, the cavity needs to be operated close to the stability boundary and requires sub-mm precision for cavity mirror alignments making the alignment quite difficult. They are also not self-starting, as initially, a small perturbation is needed to increase the laser noise.

## 4.1.5   Real absorber: SESAM modelocking

The discovery of SESAM in the 90's was a major breakthrough in ultrafast laser community. In SESAM, several semiconductor absorber layers like InGaAs quantum wells having intensity dependent absorption are embedded inside a semiconductor wafer-like GaAs/AlAs called Bragg-mirror. The structure of a SESAM is shown below 4.5. When the intracavity photons strike the absorber layer of SESAM, due to absorption, it gives rise to electron-hole pairs which increases with increase in number of photons. However, after a certain point due to a limited number of electron-hole pairs, the absorption saturates and the electron-hole pair recombines non-radiatively. The absorption starts again after the period defined by the recovery time of the SESAM. The wide range of bandgap of a semiconductor allows a broad range of operation from visible to far-infrared spectral region. Moreover, defect engineering of the semiconductor allows recovery times ranging from *ns* to *fs*. The parameters that describe SESAM are the recovery time, modulation depth, bandwidth, saturation fluence and non-saturable losses, obtained by the design of semiconductor mirror device. Their small saturation fluence, integration as a cavity mirror, sophisticated bandgap and defect engineering and epitaxial fabrication makes it good for self-starting modelocking of the ultrashort laser pulse. The Bragg-layers can be designed both in resonance or anti-resonance. In the resonant case, the SESAM can have quite a large modulation depth, but in this case the bandwidth is limited. However, in anti-resonant case, the SESAM can have large bandwidth, but is limited by the

modulation depth. In this case, modulation depth can be increased only at the expense of increased non-saturable losses. Depending on the application, different designs of SESAM are used. For example, in solid-state lasers where the single pass gain is low and very sensitive to losses, low non-saturable loss is preferred. Whereas, in fiber lasers, where the single-pass gain is quite high, the non-saturable loss is less important. In this case, the recovery time of SESAM should be as fast possible, as if it is of the same order as that of the pulse, a chirped pulse can give rise to asymmetric spectra and thereby affecting the pulse dynamics strongly. Long recovery times of SESAM also limits the obtainable pulse duration from a laser cavity. Typically, the short recovery time enables shorter pulse generation while it should be long enough to initiate the modelocking process. Since due to spontaneous emission, the relaxation is limited to ns-range, several techniques during the SESAM design is deployed to obtain fast relaxation time artificially that introduces lattice defects. For example, growth temperature and ion concentration are varied. Very recently, a new kind of absorber is discovered that is based on carbon nanotubes and graphene which offers several advantages over SESAM and other NPE based modelocking in fibers [48, 49, 50, 51]. Their advantages include subpicosecond recovery times, broadband operation, polarization insensitivity, high optical damage threshold, environmental robustness, chemical stability ease of fabrication and integration into all-fiber configuration. It also has the ability to operate both in transmission and reflection mode both. These favorable features of carbon nanotubes staturable absorber makes it quite demanding and is today a very hot topic of research.

### 4.1.6 Q-switching instabilities

An important aspect of modelocking in an oscillator is the tendency of Q-switching i.e. the pulse train suffer from huge modulation in *ns*-time scale (as shown in figure 4.5). Depending on the type of pulse train generated, different states defined are (1) pure Q-switching (2) Q-switched modelocking (3) CW-modelocking.

A Q-switched modelocked pulse resembles a nanosecond pulse with a modelocked fs-pulse underneath the pulse envelope. This tendency is higher in lasers modelocked with SESAM with slow relaxation time or those having large modulation depth and with an increase in nonsaturable losses. To obtain a clean and stable modelocked pulse, the SESAM is operated above saturation by either decreasing the spot size in the SESAM or increasing the intracavity power. Such pulses are called CW
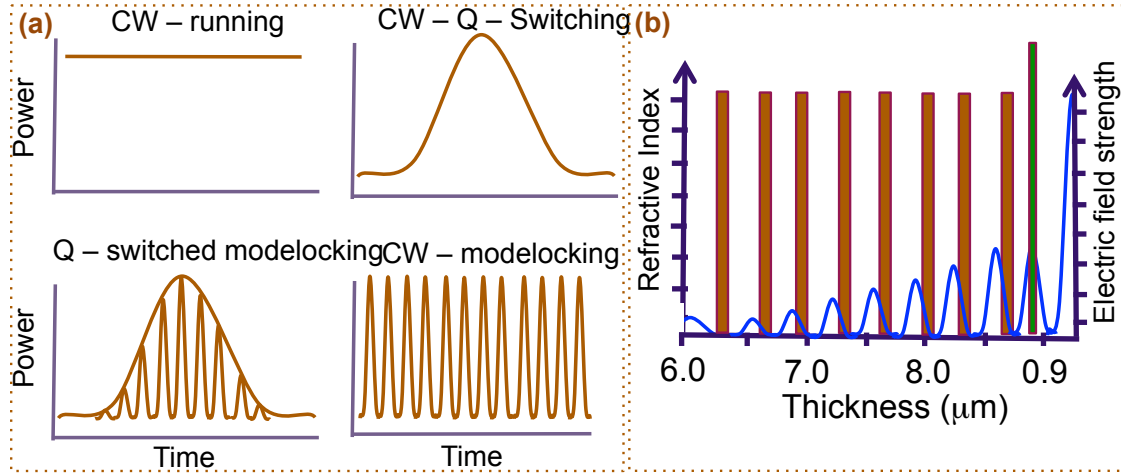
Figure 4.5: (a) Different types of modelocked operation, (b) structure of a typical SESAM. The layer thickness is of the order of quarter wave.

modelocked pulses. The tendency of Q-switching arises due to thermal effects and two-photon absorption. We briefly summarize below the conditions to obtain pure CW-modelocking state. Q-switching can be avoided if the following condition is satisfied:[52]

$$No \quad Q-switching : |\frac{dR}{dI}|I < r\frac{T_R}{\tau_2} \approx \frac{T_R}{\tau_{stim}} \tag{4.9}$$

where $r >> 1$ is the pump parameter determining the number of times laser is pumped above threshold and is related to gain of the laser $g_0$ ($g_0 = rl$ with $l$ being the total loss coefficient), $T_R$ is the cavity round-trip time, $\tau_2$ is the upper-level lifetime, $\tau_{stim}$ is the stimulated lifetime given by $\tau_{stim} = \tau_2/(r-1) \approx \tau_2/r$. Thus, above equation suggests that Q-switching can be easily suppressed for a small slope (i.e. large saturation intensity), large $r$ (i.e. the laser which is pumped much above the threshold with large small signal gain and low losses), large cavity round trip time (i.e. low repetition rate). Moreover, gain medium with large upper-level lifetime, have increased the tendency of Q-switching. Thus, pure CW modelocking state is achieved if the following condition is satisfied:

$$No \quad Q-switch \quad Modelocking : |\frac{dR}{dE_p}|E_p < r\frac{T_R}{\tau_2} \approx \frac{T_R}{\tau_{stim}} \tag{4.10}$$

And this condition can be fulfilled by choosing the intracavity pulse energy $E_p$ as $E_p >> E_{sat}$. This leads to an important conclusion that to get a stable CW

modelocked pulses from a slow saturable absorber, the conditon $E_p >> E_{sat}$ or $F_p >> F_{sat}$. However, the pulse fluence should not be too high than the saturation fluence, as this can lead to reverse-saturable absorption and bleaching of the absorber which eventually lead to multiple pulsing. Typically, to get stable CW-modelocked pulses, SESAM is operated at pulse fluence 3 - 5 times higher than its saturation fluence. This allows maximum modulation and the SESAM recovery time can be 10 - 30 times longer than the pulse duration. More details about this can be found in [47, 52].

## 4.2 Ho:YLF solid-state oscillator

**Challenges**: Ti:Sapp-based lasers are now well-established technology to generate stable modelocked pulses at 800 nm, and despite its discovery in three decades back, the material remains unbeatable due to its ultrabroad gain bandwidth (figure **??**) allowing generation few-cycle pulses directly from the oscillator. However, the scenario is completely different at 2-$\mu$m, where there do not exist a reliable commercial oscillator source. Apart from the challenge of working at this wavelength where it is not only difficult to find the variety of optical components with the right specifications but also it is difficult to work with the beams due to lack of proper viewers. Furthermore, when comparing the cross-sections of Ti:Sapp and Ho:YLF, we see that the gain profile of Ti:Sapp takes Lorentzian-profile while that in the case of Ho:YLF takes non-Lorentzian shape where there exists two emission peaks close to each other (2051 and 2066 nm). This brings a drawback of higher amount of gain narrowing, severely limiting the output spectral bandwidth and thereby the obtainable pulse duration. Therefore the amount of loss modulation required is very small (typically $\sim$1%). But as the SESAM at this wavelength is not very well developed, such a specification is not yet available even till today. Moreover, due to quasi-four-level nature of the Ho:YLF crystal, re-absorption of the emission takes place. All these factors make achieving modelocking in Ho:YLF, much more difficult than in Ti:Sapp at 800 nm. The initial attempt to mode-lock Ho:YLF oscillator was done by Lagatsky et al [53], but they used a custom designed SESAM. In this section, we present the development Ho:YLF oscillator summarizing the successes and failures.
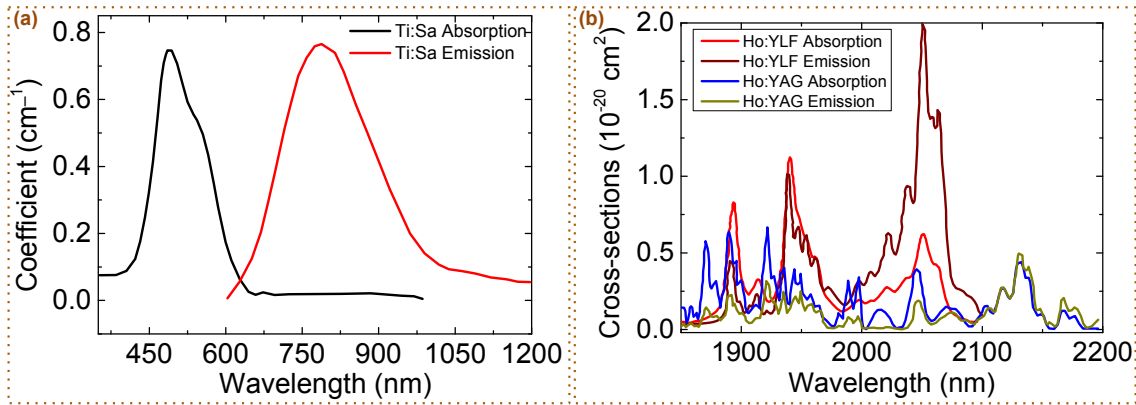
Figure 4.6: Absorption and emission cross-sections of (a) Ti:Sapp and (b) Ho:YLF gain media

## 4.2.1 Simulations

In order to understand the pulse evolution in the laser cavity of the oscillator and the design parameters needed, it is essential to simulate the pulse evolution behavior. We utilize a 1D simulation based on split-step Fourier transform technique in which the linear effects are treated in frequency domain while the nonlinear effects in the time domain. The model was developed in Matlab by Dr. Damian Schimpf. The number of points to represent the simulation grid was 2048, that was enough to represent the pulse both in spectral and time domain at every point in the cavity. Table 4.1 summarizes various initial parameters and the SESAM parameters provided by the manufacturer Batop Inc. is given in table 4.2. The model calculates the small signal gain from absorption and emission cross-section assuming a quasi-four-level for Ho:YLF gain medium with a certain pumping level included as the factor of absorption level. The small signal gain is calculated assuming quasi-four-level system. The linear dispersion was simply included by a certain number, instead of the calculating the complete path difference from the prism pair after each pass. By combining all the individual components, the laser dynamics is modeled as shown in the figure 4.7.

In the split-step method, the gain medium is divided into several thin slices characterized by dispersion, self-phase modulation. The linear pulse shaping via dispersion is first modeled in the frequency domain and then the spectral pulse shape is converted into time domain using FFT to model for the self-phase modulation. The result is then inverse Fourier transformed into frequency domain. This process is
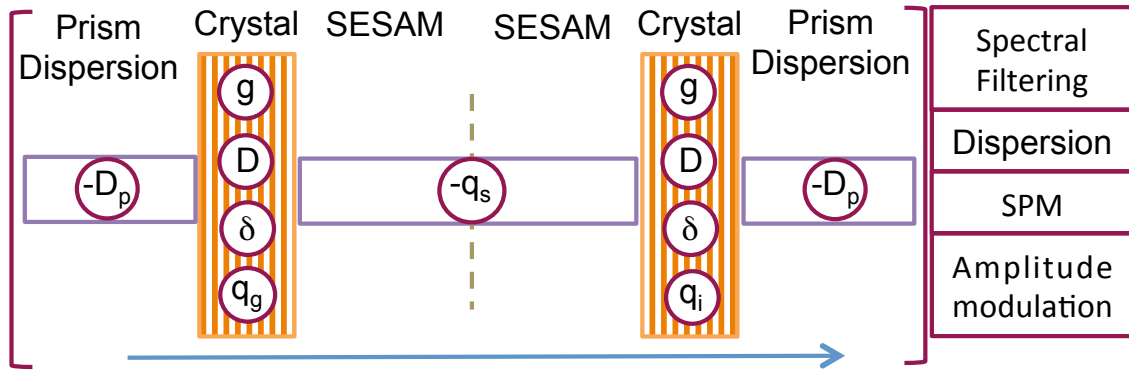
Figure 4.7: Schematic of the numerical modeling of the oscillator that includes dispersion, gain, SPM and loss-modulation due to SESAM.

repeated for each slice of the gain medium. In the model, the initial pulse build-up is not generated by spontaneous emission, rather, its done using an ideal 700 fs-Gaussian pulse and is allowed to propagate repeatedly in the cavity for 500 - 5000 number of round-trips (RT) till the pulse has converged to a steady state solution. When in the steady state, the phase shift of the pulse after every RT should be same and in order to determine this criterion, one needs to monitor root-mean-square (RMS) temporal duration, the RMS spectral width, the mean central wavelength and the pulse energy. The laser will remain in the steady state and emit a stable modelocked pulse if all these parameters reach a stable value within machine precision. However, if the nonlinear phase shift (B-integral) is much larger than $\pi$, this can lead to unstable or noisy solution giving rise to unstable modelocking or even no modelocking.

Due to the non-Lorentzian profile of the emission cross-section and quasi-four-level Ho:YLF medium (Figure **??**), the re-absorption of the emission wavelength causes inversion dependent emission peak between the 2051 and 2066 nm. When the pump inversion is low, even though the gain at 2051 is higher than 2066 peak, the emission wavelength is restrained to 2066 nm, due to the suppression of the gain at 2051 nm owing to the re-absorption. However, when the inversion is high, the re-absorption is not enough to suppress the gain at 2051 nm and the emission wavelength shifts to the 2051 nm from 2066 nm. This is depicted in the figure 4.8 small signal gain coefficient as a function of the pump inversion obtained from the absorption and emission cross-section. The small signal gain coefficient as a function of wavelength is calculated for different inversion of 0.22, 0.25, 0.27 and 0.30. We can see that for lower inversion value, the 2051 and 2066 nm peak are, relatively at the same height, however, with an increase in inversion, the ratio between the two peak increases,

Table 4.1: Simulation parameters of the oscillator used in the simulation.

| Properties | Value |
|---|---|
| Length of crystal | 14.6 mm |
| Doping conc. | 0.5 % |
| Lifetime ($\tau_f$) | 15 ms |
| Nonlinear refractive index ($n_2$) | 0.85 x 10-16 cm$^2$/W |
| GVD of Ho:YLF crystal | -37 fs$^2$/mm |
| Spot size in crystal | 76 $\mu$m |
| Spot size in SESAM | 280 $\mu$m |
| Initial pulse duration (T$_{fwhm}$) | 700 fs |
| Initial pulse energy (E) | 10 nJ |
| Intracavity pulse energy (E$_{intra}$) | 1 $\mu$J |

Table 4.2: SESAM parameters

| Properties | Value |
|---|---|
| Reflection | 96 % |
| Absorbance | 2 % |
| Modulation Depth ($\Delta$R) | 1.2 % |
| Non-saturable loss | 0.8 % |
| Saturation Fluence | 70 $\mu$J/cm$^2$ |
| Relaxation time constant | 10 ps |
| Damage threshold | 4 mJ/cm$^2$ |
| GDD | +1000 fs$^2$ |

giving rise inversion dependent emission wavelength.

Several runs of simulations were carried out to optimize the required amount of GVD introduced, to get a stable state solution and was varied. So in the simulation, the main varying parameter was restricted to GVD in the cavity to vary the effective phase shift of the pulse and the inversion level to vary the gain in the cavity. For inversion level of 0.25, an extra GVD of 3180 fs$^2$ was required to get a stable steady state solution. This was experimentally implemented by placing a pair of prism in the cavity. The pulses were allowed to propagate in the cavity for long 2000 RT, so as to see if any instability occurs for a long operation of the laser. Similarly, the dispersion parameter was scanned for three other inversion level of 0.22 %, 0.27 % and 0.30 % whose results are below in the figure 4.9. It can be seen that, with an increase in the inversion level from 0.22 to 0.35, the spectrum of the output pulses were broadened and the peak wavelength shifted from 2067 nm to 2054 nm. This eventually, resulted in reduction of the pulse duration from 1.2 ps to 0.19 ps. This is
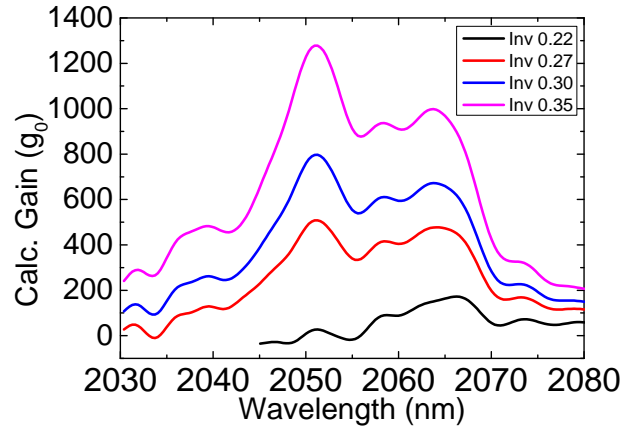
Figure 4.8: Calculated small-signal gain at different pump inversion levels.

likely because at higher inversion, the gain peak shifts to shorter 2051 nm peak (as seen in figure 4.8).
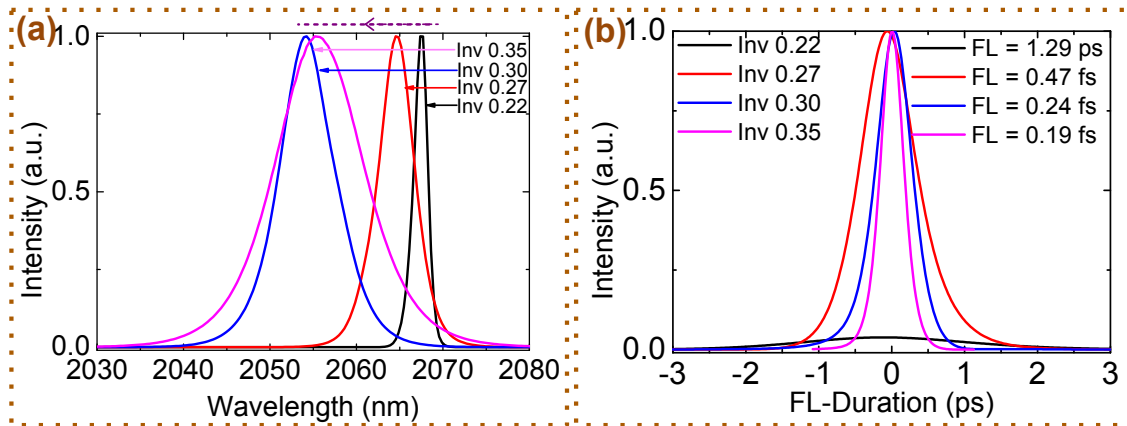


Figure 4.9: Simulation results (a) spectrum and (b) pulse profile obtained for an inversion levels of 0.22, 0.27, 0.30 and 0.35, respectively

## 4.2.2 Experiment

### Cavity design

The very first and important step for the development of any laser system is the cavity design. Distances, curvature, and angles must be carefully chosen such that the cavity supports stable modes to propagate inside the resonator. 2-$\mu$m wavelength adds further difficulty in the alignment procedure as the beam is invisible to eyes and special viewers do not exist to view such beams. The beam can be seen only using thermal cards which are sensitive to heat generated by those beams and not

by the scattered photons, that is usually the case for near-infrared light. A CW laser resonator is a Fabry-Perot cavity, that usually consists of a gain medium, few dielectric mirrors to bounce back and forth the laser radiation arranged in such a way to form a standing wave pattern in the laser cavity. The stable modes and their sensitivity can vary with the distance between the two mirrors and their radius of curvature. The commonly used resonator designs are linear resonator and ring resonator whose geometries. In a linear resonator, the laser radiation goes back and forth between the end mirror while, in a ring resonator, the radiations go in two directions thereby leading to two different beams. Moreover, in the linear resonator, the radiation passes twice through the gain medium every RT while in the ring resonator it passes only once. For practical cases, to get rid of astigmatism the cavity is folded by one or more mirrors in x-type or z-type. There is a minor difference in the geometries. The laser resonator consists of Ho:YLF gain medium with a doping concentration of 0.5 % and various lengths of 8 mm, 11.2 mm, 14.6 mm and 19.4 mm. The cavity was effectively pumped using the commercial diode pumped Tm:fiber laser emitting at 1940 nm narrow band. As the first step, the resonator was designed using the commercial ABCD-analysis. A resonator supports a stable standing mode only if the radii of the end mirrors overlap when laid along the optical axis and the stability criterion is given by:

$$0 \leqslant \left(1 - \frac{L}{R_1}\right)\left(1 - \frac{L}{R_2}\right) \leqslant 1. \tag{4.11}$$

where $L$ is the effective length of the cavity and $R_1$ & $R_2$ is the radius of curvature of the mirrors whose value if satisfies the above inequality, the resonator is stable.

Laser efficiency is the measure of the pump power converted to output power. If $P_{intra}$ is the steady state intracavity power and T is the output coupling efficiency, then the total output power is given by:

$$P_{intra} = P_{sat}\left(\frac{2g_0}{2l} - 1\right) \tag{4.12}$$

$$P_{out} = T.P_{sat}\left(\frac{2g_0}{2l_{int} + T} - 1\right) \tag{4.13}$$

where $2g_0$ is the small signal round trip gain, $P_{sat}$ is the gain saturation power and $2l$ is the power loss per round trip.

**Alignment**

The cavity needs to the precisely aligned to get a clean Gaussian mode at the output with minimum losses. The cavity distance for a stable resonator was determined using a commercial software Paraxia. After the distance was calculated, a big challenge was the alignment. Usually, for 800 nm and 1 $\mu$m laser, it is easy to align a laser cavity using an alignment laser beam at 632 nm, which is sent from the counter-propagating direction. But in our case, this method is not very reliable due to the far-off wavelength of the alignment beam, leading to different refraction from the gain medium. And this large wavelength difference will lead to a different path. To familiarize oneself with the working of low power 2 $\mu$m beam, first a two mirror cavity was aligned. In our case, the small part of the unabsorbed pump beam accompanying the fluorescence signal from the Ho:YLF medium was helpful. The detection of the fluorescence signal required to align the mirrors was made possible only using the NIRQuest spectrometer from Ocean Optics Inc. Initially, the spectrometer was aligned for the 1940 nm pump beam by using several dichroic mirrors as a filter, to reduce the pump intensity on the spectrometer.

### 4.2.3   Results and discussions

**CW characterization of 2-mirror cavity**

The laser was characterized for the linear losses and output power using the crystal of four different length of 8 mm, 11.2 mm, 14.6 mm and 19.4 mm and two different output couplers with transmission of 2 % and 5 % for each crystal length. The slope efficiency curves for laser power v/s pump power and absorbed power for each output coupler are shown in the figure 4.10. The maximum slope efficiency achieved was 40 %. The efficiency curve for all the measurement are shown in the figure 4.10. It can be seen from the figure that the slope efficiency of 11 %, 25 %, 34 % and 40 % was achieved for crystal length of 8 mm, 11.2 mm, 14.6 mm and 19.4 mm, respectively. It is to be noted that the slope efficiency for a certain crystal length remained same irrespective of the output coupler of 2 % and 5 % used even though the loss dynamics in the cavity changes with change in output coupler. This mainly because of shift of the emission wavelength to the high-gain part of the gain spectrum i.e. towards 2051 nm peak.
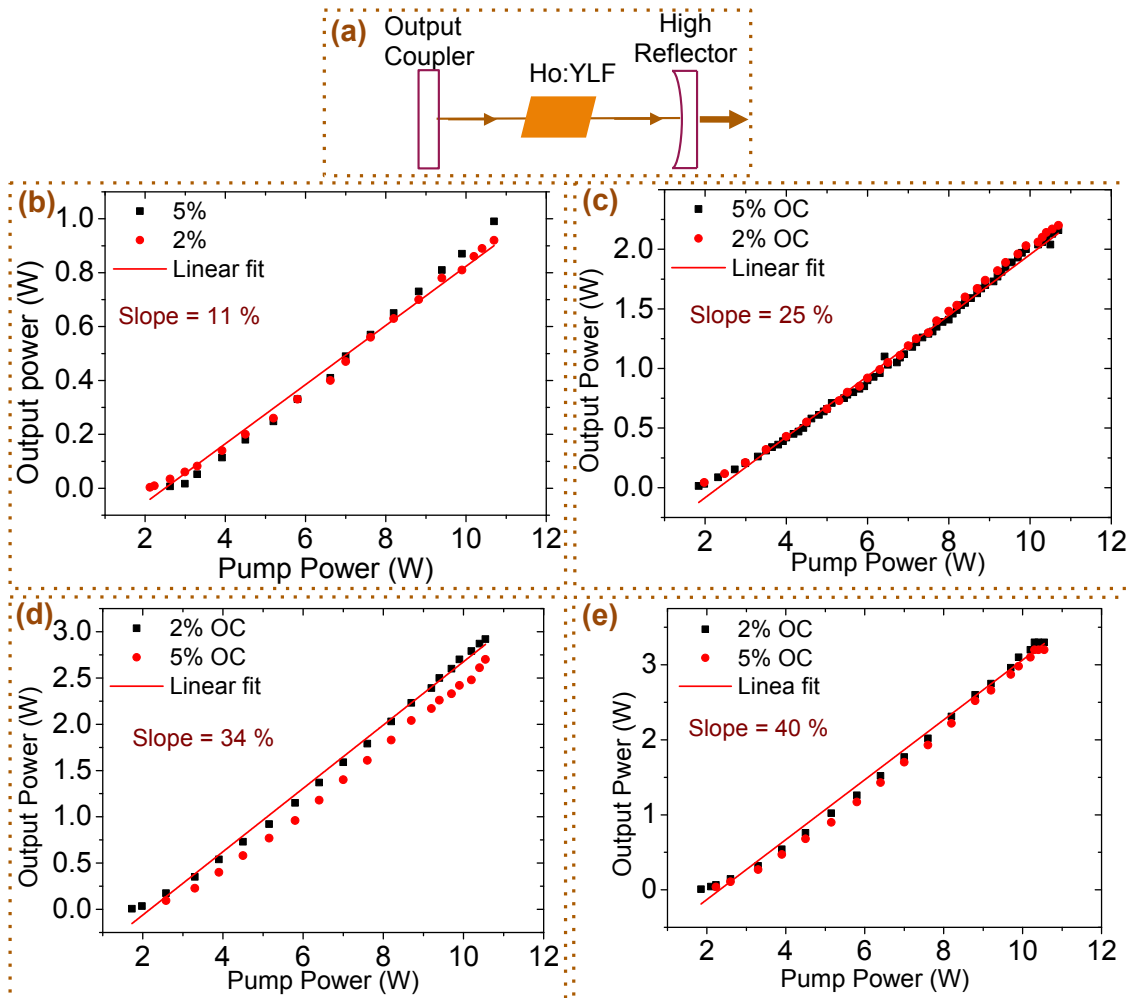
Figure 4.10: (a) Schematic of a 2-mirror cavity and (b)-(e) are the slope efficiency curves obtained for different crystal length of (b) 8 mm, (c) 11.2 mm, (d) 14.6 mm and (e) 19.4 mm, respectively.
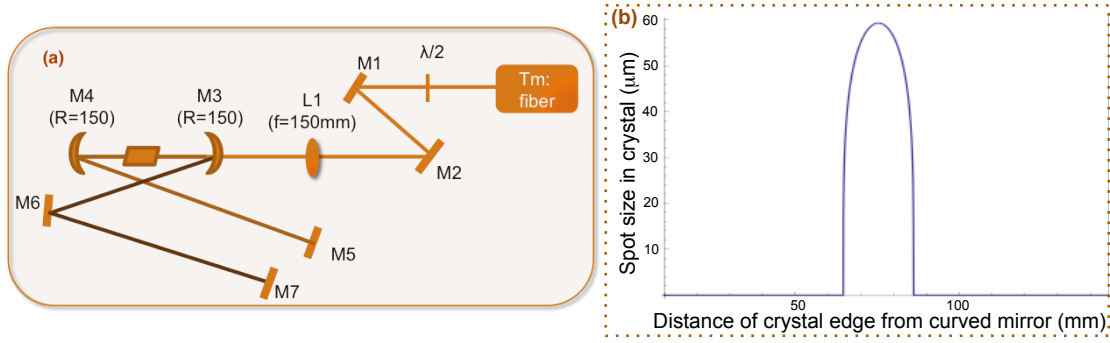
Figure 4.11: (a) Schematic of the astigmatism compensated 4-mirror x-cavity and (b) the stability curve of the mirror distances in the cavity

**Characterization of 4-mirror cavity**

After characterizing the two mirror cavity, a more practical, folded, four mirror astigmatism compensated cavity was aligned. The schematic design of the laser cavity is shown in the figure **??**. The pump laser was focused through lens $f = 100\,mm$ to a focused spot size (diameter) of $\sim$73 $\mu$m. The laser cavity was a standard astigmatism compensated z-cavity consisting of dielectric coated curved mirror $M_3$ and $M_4$ ($R = 100$ mm) and two flat end mirror ($M_7$ and $M_5$) shown in the figure **??**. $M_3$ is the anti-reflection coated mirror at 1940 nm, to reject the non-absorbed pump out of the cavity making it a single pumping cavity. $M_5$ being a high reflecting mirror and $M_7$ the output coupler. Output couplers 1 %, 2 %, 5 % and 11 % were used in the experiment. The arm lengths of 54 and 58 cm was chosen leading to a laser spot size (diameter) of 80 $\mu$m. The distances were chosen such that the pump and the laser mode is well matched. The Rayleigh length ($z_R = \pi\omega^2/\lambda$) of the laser spot was 10 mm. Due to long distances, one of the arms was folded using high reflector $M_6$. The arm length was also chosen to take into account the repetition rate requirement for Pockels cell, used in the later stage during amplification. Ho:YLF crystal cut at Brewster angle of 55.6° to avoid reflection losses and length 14.6 mm was placed between the curved mirrors $M_3$ and $M_4$. Total absorption in the crystal was 60 % at 1938 nm. The stability curve of spot size versus distance of the curved mirror is shown in the figure **??**. To compensate for astigmatism, the angle $\theta$ for the folding mirror was calculated according to equation 4.2.3:
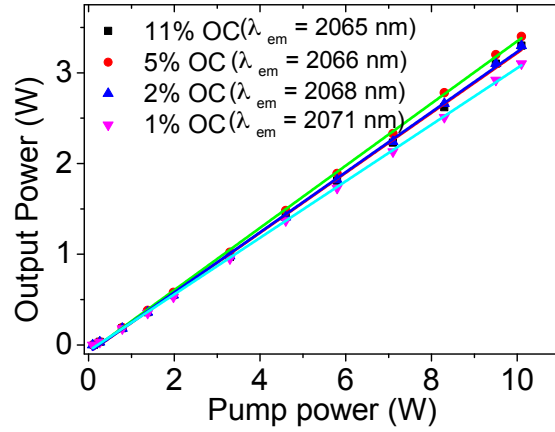
Figure 4.12: (a) Slope efficiencies of the astigmatism compensated 4-mirror x-cavity with different output couplers of 1 %, 2 %, 5 % and 11 % transmission.

$$N_{c-axis} = \sqrt{n_{eo}^2 + 1} \frac{n_{eo} - 1}{n_{eo}^4} = 0.443 \qquad (4.14)$$

$$\theta = ArcCos^{-1}\sqrt{1 + \left(\frac{N_{c-axis}t}{2R}\right)^2} - \frac{N_{c-axis}t}{2R} = 7.54^0 \qquad (4.15)$$

Once the laser cavity was aligned, CW characterization was done for linear losses and output power for crystal length 14.6 mm and one of the end mirror as the output coupler of 1 %, 2 %, 5 % and 11 %. The slope efficiency curves are shown in the figure **??** for laser power versus pump power and absorbed power for each output coupler. The estimated loss calculated from standard Finley-Clay method was 2 % and slope efficiency of 34 %. It should be again noted here that the irrespective of the transmission of the the output coupler, the slope efficiency remained same. This is for the same reason as mentioned in the 2-mirror cavity case, i.e. due to the shift of the emission wavelength.

**Modelocking using SESAM**

As discussed earlier, the intracavity beam intensity on the SESAM must be 2 - 3 times higher than the saturation intensity to avoid Q-switching instability. Hence it requires a second focus in the cavity. The modified design of the cavity is as shown in figure 4.14. Also, the stability curve of this new design according to which the distance between the mirrors was chosen, are shown.

**Dispersion management**: Since ultrashort pulses contain broadband spectrum

and each spectral components propagate at a different speed in a medium causing it to change its shape, proper dispersion management is important to keep all the frequencies intact to transform limited pulse. If $\phi(L, \omega)$ is the spectral phase given by:

$$\phi(L, \omega) \equiv \omega P/c = \omega L n(\omega)/c \tag{4.16}$$

where $P$ being optical path length given by $P = Ln(\omega), n(\omega)$ is the frequency dependent refractive index given by Sellmeier coefficient of the material. The spectral phase can be expanded using Taylor's series as:

$$\phi(\omega) \approx \phi_c + (\omega - \omega_c)\frac{d\phi}{d\omega}_{\omega_c} + \frac{1}{2}(\omega - \omega_c)^2\frac{d^2\phi}{d\omega^2}_{\omega_c} \tag{4.17}$$

Hence, the group delay dispersion due to the path difference is given by:

$$GDD(\omega) = \left(\frac{d^2\phi}{d\omega^2}\right)_{\omega_c} \tag{4.18}$$

$$GDD(\lambda) \equiv \left(\frac{-\lambda^2}{2\pi c}\right)\left(\frac{d}{d\lambda}\right)\left[\left(\frac{-\lambda^2}{2\pi c}\right)\left(\frac{d\phi}{d\lambda}\right)\right] \equiv \left(\frac{\lambda^3}{4\pi^2 c^2}\right)\left[2\left(\frac{d\phi}{d\lambda}\right) + \lambda\left(\frac{d^2\phi}{d\lambda^2}\right)\right] \tag{4.19}$$

And the new pulse duration due to the above GDD is stretched to $\tau_{out}$ given by:

$$\tau_{out} = \tau_{in}\sqrt{1 + \left(\frac{4ln(2)GDD}{\tau_{in}}\right)^2} \tag{4.20}$$

For soliton modelocking, as discussed earlier, negative GDD is required in the cavity, so that the phase shift introduced is compensated and thus the pulse maintains the shape of the soliton. The GDD can be introduced in the cavity by two means; by the material of the optical components in laser cavity itself or by introducing additional component like prism-pair or double-chirped mirrors (DCM). We introduce GDD using prism-pair in the cavity under Brewster's angle. The amount of negative dispersion required to overcome the Kerr-effect and maintain the soliton shape of the pulse is related to the soliton area theorem given by [46]:

$$D = \frac{\tau \delta E_{intra}}{4} \tag{4.21}$$

The amount of negative GVD introduced due to prism can be controlled by insertion length and distance between tip-to-tip of the prisms. The net GDD introduced by a prism pair is given by:

$$\frac{d^2\phi}{d\omega^2}\bigg|_{\omega_c} = \frac{\lambda_c^3}{2\pi c^2}\left[L_g\frac{d^2n}{d\lambda^2}\bigg|_{\lambda_c} - \left(4L + \frac{L_g}{n^3}\right)\left(\frac{dn}{d\lambda}\bigg|_{\lambda_c}\right)^2\right](for \quad single \quad pass) \tag{4.22}$$

where $L_g$ is the insertion length of the prism in the beam path, L is the distance between the prism, $(d^2n)/d\lambda^2$ is related to Sellmeier's equation.

Also, the material dispersion of YLF and prism material can be calculated using Sellmeier's equation whose coefficients are given as follows:

$$YLF : n(\lambda) = \left(1.31021 + \frac{0.84903\lambda^2}{\lambda^2 - 0.00876} + \frac{0.53607\lambda^2}{\lambda^2 - 134.9566}\right)^{1/2} \tag{4.23}$$

$$FS : n(\lambda) = \left(1 + \frac{0.69617\lambda^2}{\lambda^2 - (0.06840)^2} + \frac{0.40794\lambda^2}{\lambda^2 - (0.11624)^2} + \frac{0.89748\lambda^2}{\lambda^2 - (9.89616)^2}\right)^{1/2} \tag{4.24}$$

In order to avoid Q-switching instabilities, the absorber must be saturated enough and the intracavity energy must satisfy the following relation [52].

$$E_{intra}^2 > E_{(sat,L)}E_{(sat,A)}\Delta R \tag{4.25}$$

where $E_{intra}$ is the intracavity energy, $E_{(sat,L)}$ and $E_{(sat,A)}$ is the saturation energy of the gain medium and the absorber, respectively. $\Delta R$ is the modulation depth of the absorber.

The table 4.13 shows the required dispersion to compensate for SPM for different intracavity pulse energies expecting pulse duration of 1 ps, calculated from the above equations. The spot size (diameter) in crystal was considered to be 76 $\mu$m and that on SESAM to be 280 $\mu$m and the coefficient of nonlinear refractive index $n_2$ was taken as $0.5 \times 10^{-20}$ m$^2$/W. There was no available literature for measurement of $n_2$ at 2 $\mu$m and hence the exact value could easily deviate from this value by a factor of

| O/P Cou pling (%) | Po ut (W) | Pint ra (W) | Eintr a (nJ) | Flue nce in sesa m | Disp req. for SPM comp. (fs²) (RT) | | | Disp SESA M (RT) | Disp YLF (RT) | Net −ve GVD required (fs²) (RT) | | | Required prism separation (mm) | |
|---|---|---|---|---|---|---|---|---|---|---|---|---|---|---|
| | | | | | t=500f s | t=1p s | t=2p s | | | t=500f s | t=1ps | t=2ps | t=1ps | t=2ps |
| 1% | 0.2 | 20 | 200 | 325 | 715 | 1430 | 2860 | + 1000 | -1100 | 615 | 1330 | 2760 | 6 | 57 |
| | 0.3 | 30 | 300 | 487 | 1072 | 2145 | 4290 | + 1000 | -1100 | 972 | 2045 | 4190 | 31 | 105 |
| 2% | 0.3 | 15 | 150 | 243 | 537 | 1075 | 2150 | + 1000 | -1100 | 437 | 975 | 2050 | 1 | 31 |
| | 0.4 | 20 | 200 | 325 | 715 | 1430 | 2860 | + 1000 | -1100 | 615 | 1330 | 2760 | 6 | 57 |
| | 0.5 | 25 | 250 | 406 | 895 | 1790 | 3576 | + 1000 | -1100 | 795 | 1690 | 3476 | 18 | 82 |
| 5% | 0.5 | 10 | 100 | 162 | 357 | 715 | 1430 | + 1000 | -1100 | 257 | 615 | 1330 | 1 | 6 |
| | 0.6 | 12 | 120 | 195 | 430 | 860 | 1720 | + 1000 | -1100 | 330 | 760 | 1620 | 1 | 16 |
| | 0.7 | 14 | 140 | 227 | 500 | 1000 | 2000 | + 1000 | -1100 | 400 | 900 | 1900 | 1 | 26 |

Figure 4.13: Dispersion management for soliton modelocking to obtain a soliton pulse of 1-ps duration

2, which changes the amount of dispersion required. The table shows that as the intracavity energy increases i.e. with increase in fluence on the SESAM, the net amount of negative dispersion required for a stable modelocked pulses also increases.

Taking into account the above conditions, the laser cavity was further extended by replacing $M_5$ with a high reflecting curved mirror and semiconductor saturable absorber (SESAM) $M_8$. The cavity was further modified with dispersion compensation accounting for the right GDD as calculated from the table 4.13. GDD introduced in this case was $\sim 2500 fs^2$ and was introduced using fused silica prism pair $P_1$ and $P_2$. To avoid Fresnel reflection losses the prisms were placed at Brewster angle of $55°$. The schematic of the laser cavity with prism pair for dispersion compensation and SESAM is shown in the figure 4.14. Also the stability curve of the new cavity with spot size versus curved mirror distance are shown in the figure 4.15.

This modified layout of the laser with SESAM and fused silica prism was then characterized for the linear losses in the cavity. Figure 4.16 shows the slope efficiency curves of the modified cavity for three different output coupler of 1 %, 2 %, and 5 %. The dotted curves are the actual measurement while the solid lines are the linear fit. The slope efficiencies obtained are 3 %, 4 % and 10 % for 1 %, 2 % and 5 % output coupler respectively. Wavelength tuning curve is shown in the figure 4.16 which was measured using a single prism inside the cavity and the mirror $M_7$ was tuned horizontally to align the cavity for each wavelength of the spectrum. The maximum tuning bandwidth of foot-to-foot bandwidth of 52 nm was obtained.

By carefully optimizing the alignment and the GVD from the prism pair, we could get the laser modelocked whose spectrum and oscilloscope pulse train are shown in
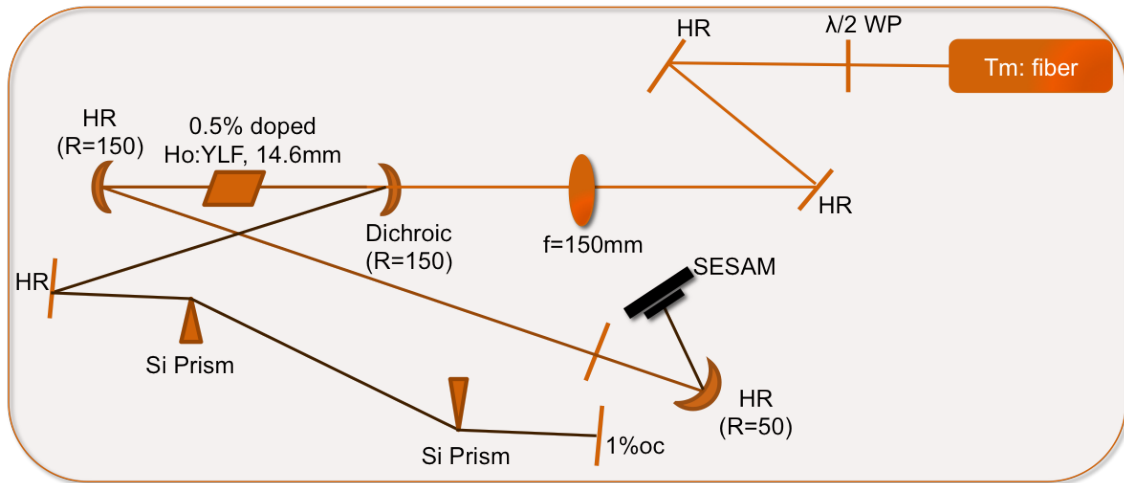
Figure 4.14: Schematic of the 6-mirror cavity with SESAM and prism pair in the cavity
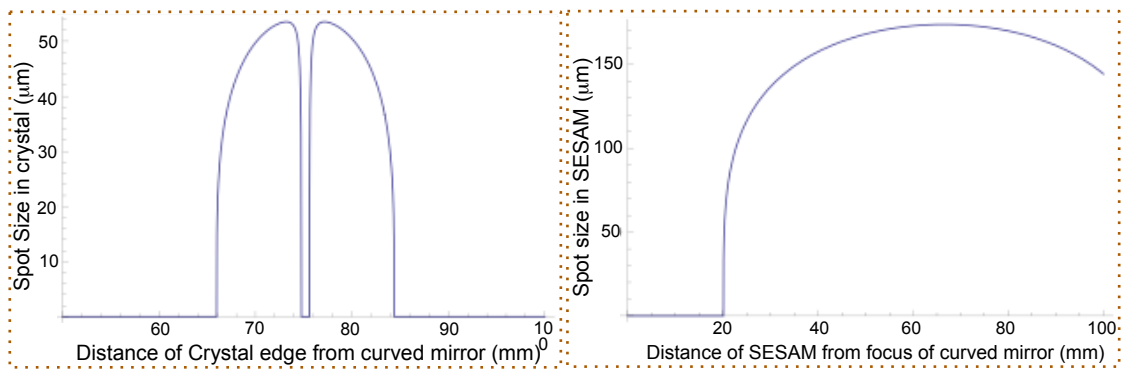


Figure 4.15: Stability curve of the 6-mirror cavity including SESAM
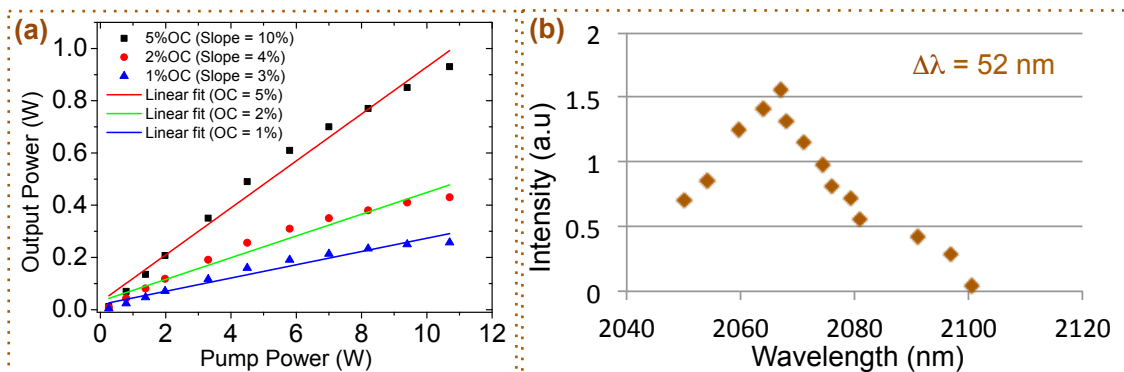


Figure 4.16: (a) Slope efficiency of 6-mirror cavity with SESAM and (b) wavelength tuning curve obtained at pump power of 10W from the oscillator
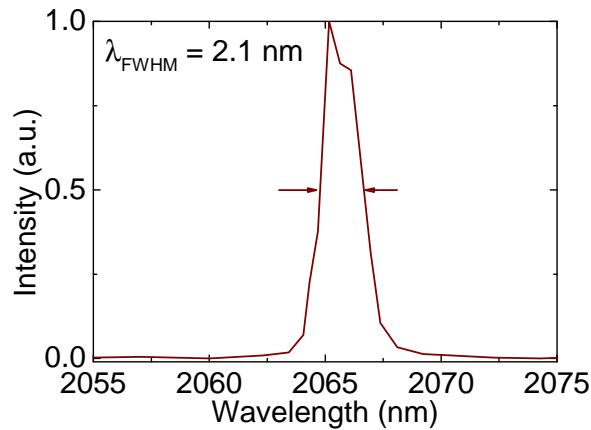
Figure 4.17: Optical spectrum of the modelocked pulse obtained from a NIRQuest spectrometer
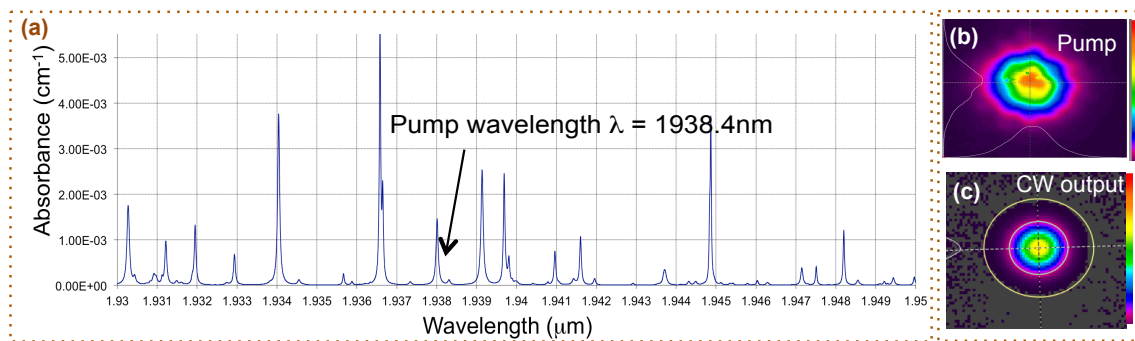


Figure 4.18: (a) Air absorption lines taken from Hitran database and (b) mode-profile of the Tm:fiber pump laser
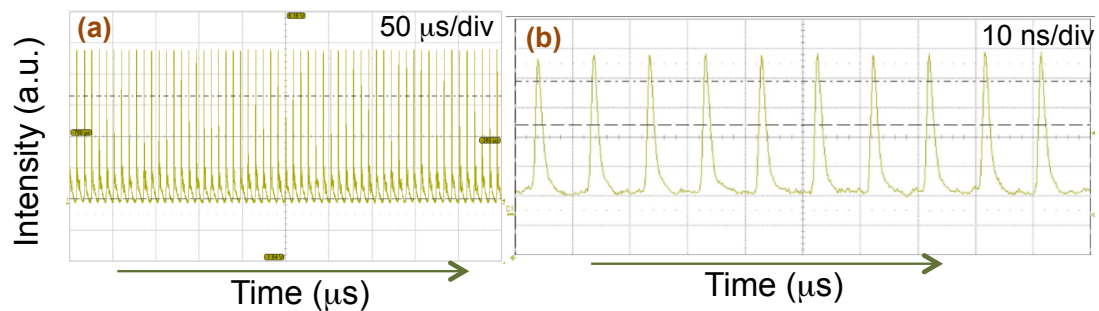


Figure 4.19: Trace of the modelocked pulses obtained from an oscilloscope
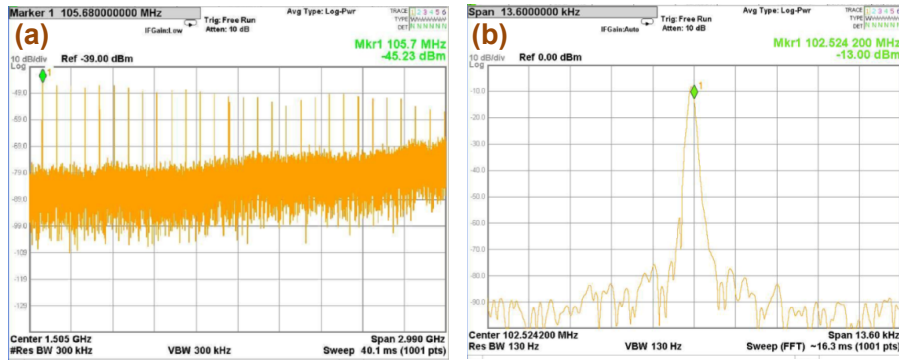
Figure 4.20: RF spectrum of the modelocked pulses obtained from a RF spectrum analyzer

the figure 4.17 and 4.19, respectively. Moreover, there was small oscillation on top of the pulses and the modelocking state was not stable due to which the pulses could be modelocked for a very short time. These instabilities can be attributed to several factors like improper SESAM design having a fast relaxation time, instability arising from the Tm:fiber pump source whose mode profile was not stable enough (figure **??**) and was very sensitive to the delivery fiber movement. Furthermore, the pump wavelengths are very close to the air absorption lines shown in the figure **??**, taken from Hitran database. Hence a slight shift in the wavelengths could lead to large loss fluctuations leading to instability in the modelocked pulses.

### 4.2.4   Conclusions

In conclusion, we demonstrated development of Ho:YLF based laser oscillator. It was characterized for various configuration. Fused silica prism pair were used to introduce the required dispersion in the cavity for soliton modelocking. However, the modelocking state was not very stable and requires the better design of the SESAM. Hence it was not possible to use this oscillator for further development of the MIR laser. We therefore utlized Ho:fiber oscillator as the seed laser for later part of the project, and its amplification is discussed in the next chapter.

# 2 Micron Laser Amplifier

I n the previous chapters we discussed the importance of 2-$\mu$m laser source for MIR pulse generation and various technology available for its generation. We demonstrated working of a Ho:YLF seed oscillator, the results obtained and the issues were presented. Due to the stability issues of the Ho:YLF solid-state oscillator, we decided to seed the amplifier system using a Ho:fiber oscillator which was developed in a joint collaboration with Ingmar Hartl's group at DESY. The fiber oscillator emitted broadband laser pulses at 2060 nm central wavelength and energy of 1 nJ at 160 fs duration [54]. In this chapter, we present the amplification of this low energy pulses to mJ-level using Ho:YLF amplifier. As discussed in Chapter 3, a regenerative amplifier (RA) is a common method to amplify such low energy pulses to mJ-level. We purchased a prototype amplifier system from Q-Peak Inc. based on Ho:YLF gain medium. The design details of this RA and the seeding results with the Ho:fiber oscillator are presented here.

## 5.1    Various amplification techniques

High-energy laser pulses can be generated using several techniques depending on the applications and energy requirement as shown in the figure 5.1. Since the discovery of the very first laser in 1960, the laser peak power advanced in several leaps and within each leap the peak power increasing with three orders of magnitude occurring

due to the reduction in pulse duration by three orders of magnitude. The evolution of laser intensity at differnet time period starting from its invention in 1960 is shown in the figure 5.1 [5]. Initially, people developed lasers in a kW range having pulse duration of $\mu$s which jumped to MW range with the discovery of Q-switching process, thereby reducing the pulse duration to ns. In the next leap, with the discovery of the mode-locking process, the pulse duration could be reduced to ps-level thereby increasing the peak power to GW range. However, at this power density, the intensity dependent refractive index change known as Kerr effect, kicks-in. This results in central part of the beam seeing larger index than the sides, leading to a lensing effect inside the cavity thereby distorting the overall beam quality. Therefore, it became fundamentally impossible to increase the peak intensity of the laser system beyond GW-level, which is the main cause of the plateau in the figure 5.1. In the late 80s came the discovery of CPA, which became the work-force and it remains the state of the art till today, to generate intense laser pulses. In this technique, instead of amplifying the pulse directly, it is first stretched temporally using a grating to several orders of magnitude, that reduces the peak intensity of the amplified pulse in the cavity, thereby avoiding the intensity dependent nonlinear index change. After amplification in the cavity, the pulse is finally compressed to very high peak intensity. By using this technique, storage of extremely high energy in the gain medium was possible thereby making feasible the design of big facilities like Lawrence Livermore, Berkeley (LLBNL) for laser fusion experiment. This led to the major advent of high peak power lasers, as the pulse intensity which was earlier generated using large scale facilities could now be generated in a small scale university laboratory. It is to be noted that it was also around this time, the Ti:Sapp as a laser gain medium, which supports ultrabroad gain bandwidth was invented, combining it with a CPA system led to the real boom in the entire laser field enabling mJ-level few-cycle laser pulses.

Since a laser medium can store energy in its upper level for a period equal to its lifetime, it is possible to pump the medium for a time shorter than the lifetime and then the medium is inverted to store the energy of pump pulse on to the seed pulse. If the seed pulse arrives at the gain medium in a time much shorter than the lifetime, it can extract the energy stored from the pump pulse as it propagates along the medium and thus gets amplified (as shown in 5.2). Typically, for the medium with a lifetime of ms, the Q-switch time for the seed pulse is ∼100 ns. It is desired to have the repetition rate of the seed pulse much higher than the upper lifetime so that the energy is extracted without loosing efficiency. The amplifier can be modeled
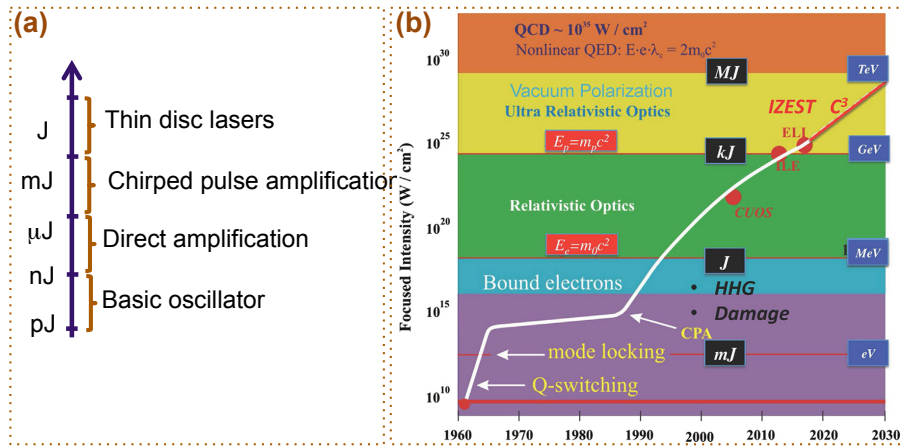
Figure 5.1: (a) Various pulse amplification techniques with their achievable energy and (b) historical evolution of laser pulse energy (figure reproduced from [5]).
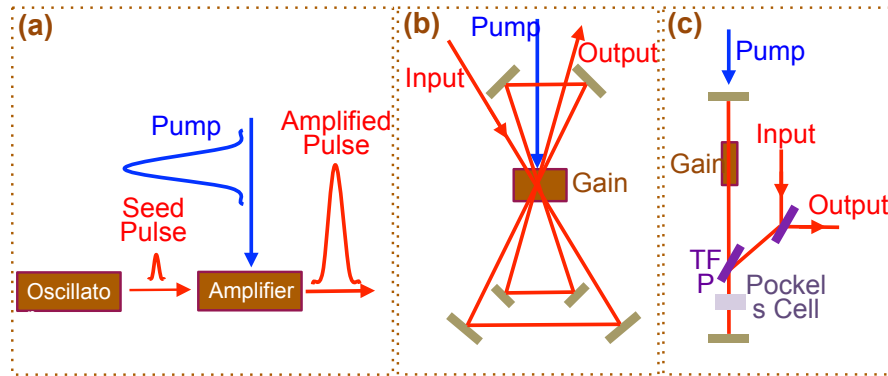


Figure 5.2: Schematic of a (a) amplification of a low energy seed pulse in a laser amplifier, (b) in a multipass amplifier and (c) in a regenerative amplifier.

using the famous Frantz-Nodvik model [55] that will will be discussed in later part of the chapter. There are mainly two configurations of an amplifier shown in figure 5.2. Multi-pass amplifier and regenerative amplifier (RA). The mechanism involved in both multi-pass amplifier and RA are similar, such that the low energy seed pulses passes multiple times in the gain medium thereby extracting the pump energy and amplification occurs. The only difference between the two is that the number of passes in the gain medium is fixed in the case of multi-pass amplifier while that can be actively controlled in the case of an RA.

## 5.1.1 Chirped pulse amplifier

The chirped pulse amplification (CPA) technique is the most common approach of today's advanced high-energy laser system. In this technique, the laser pulse that is
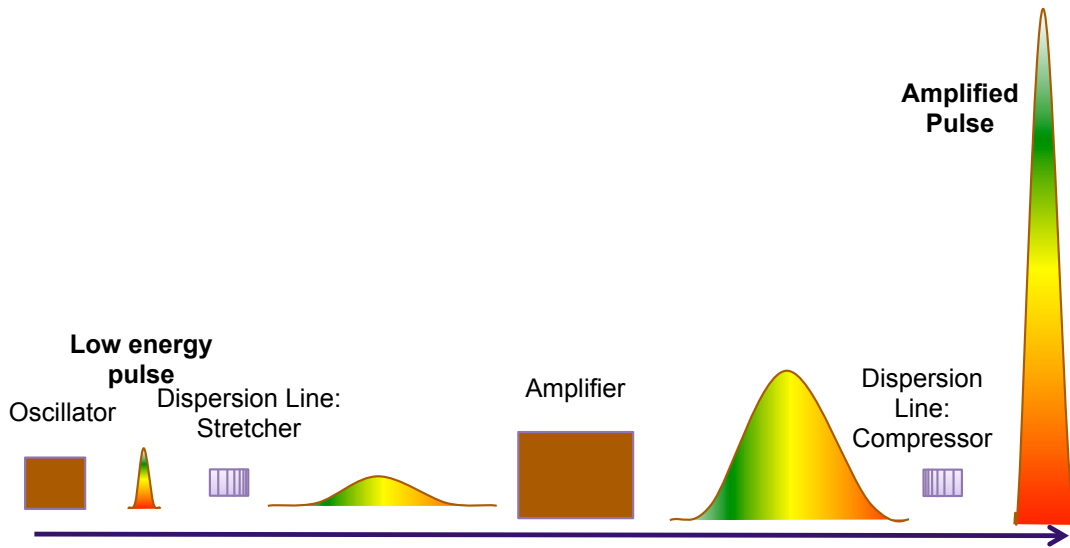
Figure 5.3: Principle of a chirped pulse amplifier.

to be amplified, is first stretched in time and then amplified. After amplification, the pulse is re-compressed back, thereby reducing the peak intensity by 3 - 4 orders of magnitude in the laser cavity and avoiding damage of the optical component. The stretching is achieved using a pair of gratings that introduces a frequency dependent path difference such that the low-frequency component of the pulse travels a shorter path than the high-frequency part. Thus the high-frequency part lags behind the low-frequency thereby creating positive or up-chirp on the pulse, that has a longer pulse duration by 3 - 4 orders of magnitude. Likewise, the compression is achieved by reversing the process, i.e., arranging the grating pair such that the high-frequency part travels shorter path than the low-frequency part and creating negative or down-chirp thereby compensating the overall chirp and finally generating amplified Fourier-limited pulse. The complete process is depicted in the figure 5.3. It is to be noted that the complete process can be done vice-versa as well, i.e. down chirp before amplification and up chirp after amplification. However, there are certain limitations for this technique as well, that mainly arise from the requirement of large stretching/ compression ratio and broad spectrum amplification.

## 5.2    Regenerative amplifier

Regenerative amplifier (RA) is the most commonly used amplifier nowadays, to amplify pulses by 7 - 8 orders magnitude, where amplified spontaneous emission (ASE) does not affect the amplification to a large extent (common limiting factor for
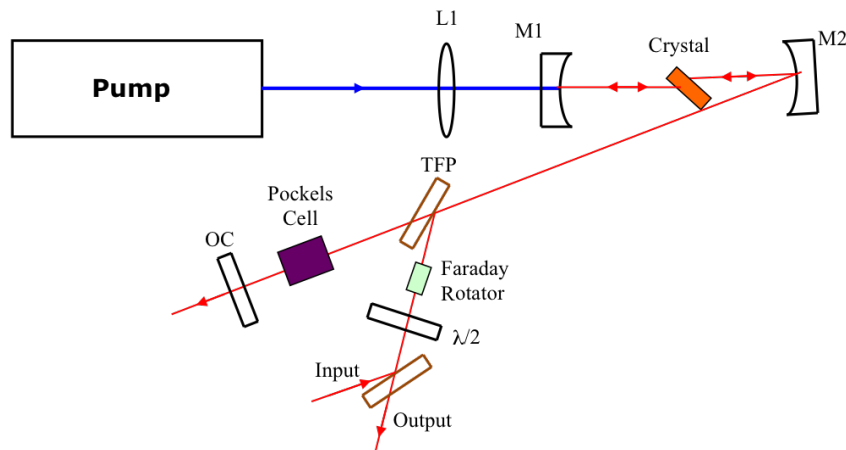
Figure 5.4: Schematic of a regenerative amplifier

a multipass amplifier). Another advantage of a RA over multipass amplifier is that the number of passes for amplification in the amplifier can be actively controlled in an RA, which is fixed in the case of a multipass amplifier and requires changing of the laser geometry itself for changing the number of passes. In an RA, the gain medium whose gain spectrum matches that of the seed pulse is placed in an optical resonator and the laser pulse to be amplified is coupled in and out using an optical switch operated by an electro-optic Pockels cell in combination with a polarizer [56].

**Principle of operation**

RA is an advanced amplifier, in which an optical resonator provides multiple passes of the seed pulse, gain medium pumped by another pump laser provides amplification, and the electro-optic switch acts as a valve for injection and rejection of the seed pulse and extraction of the amplified pulse. In the figure 5.4 the principle of an RA is shown. Here, the pump pulse should be shorter than the upper-level lifetime. The seed/signal pulse arrives at the medium after pumping and it is well within the life-time of the medium, to extract the stored energy before it is lost due to relaxation. The cavity is similar to that of a Q-switched laser whose Q-factor is controlled by an electro-optic switch which comprises of a Pockels cell, quarter waveplate and a polarizer. The RA is operated in two states: low-Q and high-Q. When no voltage is applied to the Pockels cell then the intracavity losses are high i.e. the RA operates in low-Q state and no lasing occurs and due to continuous pumping, population inversion builds up in the gain medium. This is called pump cycle. When the voltage is applied to the Pockels cell for some pre-set time, the intracavity losses are low and

the cavity operates in the high-Q state. In this state, the seed pulse is injected in the resonator and gets amplified extracting the stored energy in the gain medium. The intracavity energy grows until the gain becomes equal to the intracavity losses after which the pulse energy decays and at this point the Pockels cell voltage is switched off and the amplified pulse is ejected out of the cavity. This is called amplification cycle. Now the system is back to the low-Q state and the depleted part of the inversion is restored by the continuous pumping and returning the system to the initial state. This process iterates and becomes interdependent, leading to an instability between the pumping and amplification cycle for high-repetition-rate systems, i.e., when the pump cycle is comparable or less than the upper-level lifetime. This leads to complicated instability chaotic pattern of the pulse evolution.

**Theory of RA dynamics**

In order to understand the energy extraction process and under certain conditions occuring chaotic pattern of an RA, the rate equation analysis needs to be understood. The detailed analysis was presented by Grishin et al [56], part of which is presented here. Without going into all the details of the complete analysis, the gain and energy for such system can be written in the form of the following coupled differential equations:

$$\frac{dg(t')}{dt'} = -\epsilon(t')g(t') + \frac{1 - g(t')}{\tau_1} \tag{5.1}$$

$$\frac{d\epsilon(t')}{dt'} = \epsilon(t')[g(t') - g_t] \tag{5.2}$$

where $t' = tG_0/T_0$ is the normalized time, $T_0$ is the cavity round-trip time, $g = N\sigma L_a/G_0$ is the normalized gain, $G_0 = R_p T_1 \sigma L_a$ is the steady-state gain coefficient per pass, $\epsilon = \phi\sigma/A_a G_0$ is the normalized energy, $\tau_1 = T_1 G_0/T_0$ is the normalized relaxation time, $g_t = T_0/T_c G_0$ or $g_t = -ln(1-l)/G_0$ is the normalized threshold gain with $l$ being the loss coefficient. $N$ is the population inversion parameter, $\phi$ is the photon number, $R_p$ is the pumping rate, $T_1$ is the upper-level lifetime, $\sigma$ is the emission cross section, $T_c$ is the photon decay lifetime that accounts for the losses in the cavity, $V$ is the mode volume, $L_a$ is the length of the gain medium, $A_a$ is the active beam area in the gain medium, $c$ is the speed of light.

Considering first the low-Q pumping phase (no lasing case $\epsilon = 0$), the gain after

a certain pump phase duration $T$ can be derived as:

$$g_{pf} = 1 - (1 - g_{pi})exp(-\frac{T}{T_1})$$

(5.3)

where $g_{pi}$ and $g_{pf}$ is the initial and final gain, respectively, during the pump phase.

Similarly, considering high-Q or amplification phase, due to the short build-up time with respect to pump phase duration and upper-level lifetime, the inversion level change caused by pumping is much smaller in comparison to that the inversion depletion by amplification. Hence, in equation 5.1, the spontaneous decay and pumping term can be neglected. Now assuming, that the seed energy is much less than the stored energy and applying all the assumptions made so far, the analytic solution of 5.1 can be derived as:

$$g_{af} = \frac{g_{ai}}{1 + \frac{\epsilon_s}{g_{ai}}exp(g_{ai}\tau)}$$

(5.4)

$$\epsilon_f = \frac{g_{ai}}{1 + \frac{g_{ai}}{\epsilon_s}exp(-g_{ai}\tau)}$$

(5.5)

where $g_{ai}$ and $g_{af}$ are the initial and final gain at the end of the amplification phase, $e_s$ and $e_f$ are the initial and final seed energy, $\tau = T_0 G_0$ is the normalized amplification time after which the process is terminated. $\tau$ represents the total multi-pass small-signal gain factor. In the above equation, $g_{af}$ and $e_f$ is the final gain and energy obtained at the end of first amplification cycle. Similarly, by applying the theory of one-dimensional discrete time analysis, $n$ number of iteration can be made to this pulse. If $g_{ai}(1)$ and $g_{af}(1)$ are the initial and final gain after the first amplification cycle and if $g_{pi}(1)$ is the gain in the subsequent pump cycle, then $g_{af}(1) = g_{pi}(1)$, since the gain in the subsequent pump cycle will start from the same value as that from the last amplification cycle. Hence the boundary condition within $k_{th}$ cycle is $g_{af}(k) = g_{pi}(k)$ and for the subsequent cycle it is $g_{pf}(k) = g_{ai}(k+1)$.

Similarly, the corresponding time boundary conditions can be written as:

$$t_{ai}(k) = (k-1)\left(\frac{\tau T_0}{G_0} + T\right)$$

(5.6)

$$t_{af}(k) = k\left(\frac{\tau T_0}{G_0} + (k-1)T\right)$$

(5.7)

By carefully mapping the gain terms after each cycle, the net gain evolution can be derived as:

$$1 - (1 - g_1)exp\left(\frac{T}{T_1}\right) = \frac{g_1}{1 + \frac{\epsilon_s}{g_1}exp\left(g_1\tau\right)} \tag{5.8}$$

The right-hand side of the above equation gives the gain transformation function during the amplification while the left-hand side represents an inverse function of the gain recovery during the pump phase. Due to the continuity of the boundary conditions, both the curves $g_{af}$ vs $g_{ai}$ and $g_{pi}$ vs $g_{pf}$ can be combined, which gives a better understanding of the RA dynamics and the chaotic behavior. More qualitative insights regarding this chaotic regime is discussed in the later part of the chapter.

## 5.3 Ho:YLF amplifier

### 5.3.1 Design details

The RA cavity was a conventional standing wave linear cavity whose main component consists of a gain medium, Faraday isolator and an electro-optic cell whose schematic is shown in the figure 5.5. The electro-optic cell was used to control the number of round-trips (RT) of the pulses in the cavity through the gain medium. The optical length of the resonator was ~184 cm utilizing 0.5 % doped 40-mm long Ho:YLF crystal and it is end pumped by a continuous wave (CW) Tm:fiber laser (IPG Inc.) at 1938 nm delivering randomly polarized output up to ~50 W of power. The pump beam was polarized using a polarizing beam splitter (PBS) and the power was split between RA and the post single-pass amplifier (SPA), thereby leading to maximum available linear polarized output on each amplifier is 25 W. The small signal absorption of the RA crystal is 93 % for p-polarization. For pulse injection and rejection, an electro-optic (EO) RTP Pockels cell with a quarter-wave voltage of 1.05 kV in combination with a quarter wave plate (QWP) and a thin film polarizer (TFP) were used. After RA, a booster single pass amplifier (SPA) was present which also comprised of Ho:YLF gain medium. Due to the presence of atmospheric absorption lines around the operating wavelength of the pump laser, the amplifier system was purged using dry nitrogen gas to a relative humidity of < 2 %. The temperature of the laser crystals is kept at 20˚C via thermoelectric cooling. The complete details of
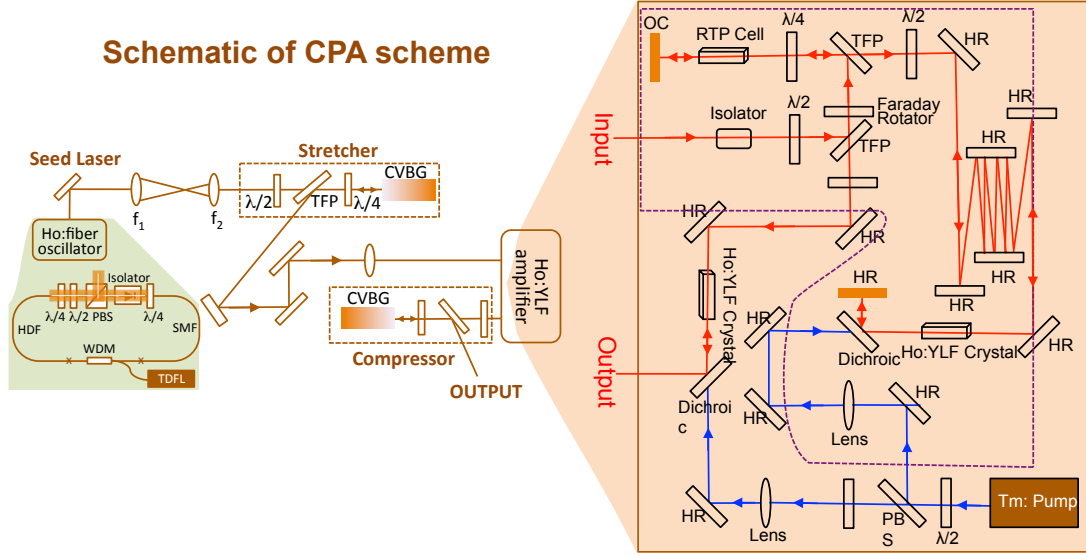
Figure 5.5: Schematic of the RA cavity and the single-pass amplifier

the amplifier system are described in Ref. [57].

## 5.3.2   Experiment

The experiment consists of a conventional CPA system based on the Ho:fiber master oscillator, prototype Ho:YLF RA followed by a SPA (Q-peak Inc.) and CVBG. The Ho:fiber oscillator consited of a unidirectional ring cavity with nonlinear polarization evolution (NPE) mode-locking scheme delivering optical pulses of 1 nJ energy at 34 MHz repetition rate. The fiber oscillator was pumped by another CW Tm-fiber laser (IPG Inc.) emitting linear polarized output power of 10 W. The pump beam was coupled into the cavity using a wavelength division multiplexer. The intracavity dispersion was introduced using small core HNLF and exhibited slightly normal dispersion regime. NPE was utilized to initiate and stabilize the modelocking of pulses. The rejection port of the polarizing beam splitter was used as the output port of the oscillator which was then coupled into a non-PM single mode fiber to make the oscillator output as fiber coupled output. The complete design details Ho:fiber seeder can be found in Ref. [58]. Fiber-coupled output is advantageous for beam pointing and delivery. The schematic details of the oscillator is shown in figure 5.5. The output pulse duration as characterized from FROG was 160 fs with Fourier-limited duration of 145 fs. To characterize the amplitude noise of the laser pulses, relative intensity noise (RIN) was performed on the oscillator output after stretching and on the pump beam at different power level using InGaAs PIN
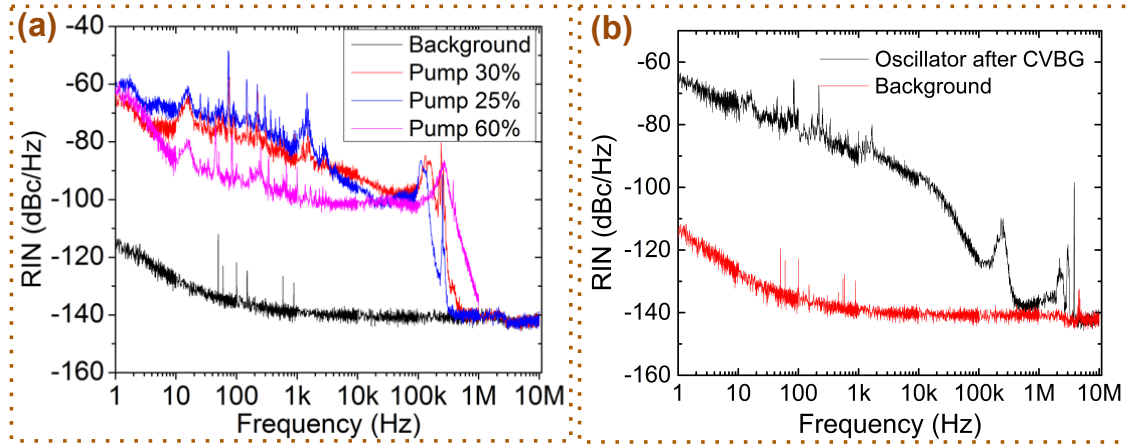
Figure 5.6: RIN measurement of the pump and the seed pulses of the RA

photodiode followed by a trans-impedance amplifier for a frequency range from 1 Hz to 10 MHz. Vector spectrum analyzer (VSA) with a 1.9 MHz low pass filter was used to measure the power spectral density for the range 1 Hz to 100 kHz while due the larger dynamic range, an RF analyzer was used for the range 100 kHz to 10 MHz and the results are shown in the figure 5.6.

The oscillator seed pulse before seeding into the RA for amplification, was temporally stretched using CVBG to the pulse duration of ~300 ps over the foot-to-foot bandwidth of 18 nm as measured by a 12.5 GHz detector and a sampling oscilloscope. The seed beam size was adapted to the CVBG aperture using a telescope. CVBGs were employed for pulse stretching and compression for compactness and robustness against external disturbances. The CVBGs used were anti-reflection coated centered at 2050 nm and designed for a foot-to-foot spectral bandwidth of 18 nm with a linear chirp rate of ~19 ps/nm. They exhibit a square transverse aperture of 5 mm × 5 mm and a clear aperture of 85 %. The CVBG length was 34 mm with a diffraction efficiency of ~88 %. The reflected beam from the CVBG was picked-up using a QWP and a TFP in combination, to minimize the incidence angle on the CVBG thus avoiding astigmatism on the beam (as shown in the figure 5.5). Figure 5.7 shows the optical spectrum of the oscillator pulses before (black), after (red) the CVBG stretcher and (blue) the amplified spectrum. As seen, there is a severe reduction in the seed spectrum due to the limited bandwidth of the CVBG, which leads to the FWHM spectrum of 8.2 nm. The seed energy is reduced from 1 nJ to 60 pJ. To avoid feedback to the oscillator, Faraday isolators were used and then the stretched pulses were seeded in the RA. To better mode-match the pump and seed pulses in the RA cavity, the seed beam was first collimated to a size of 2.5 mm and
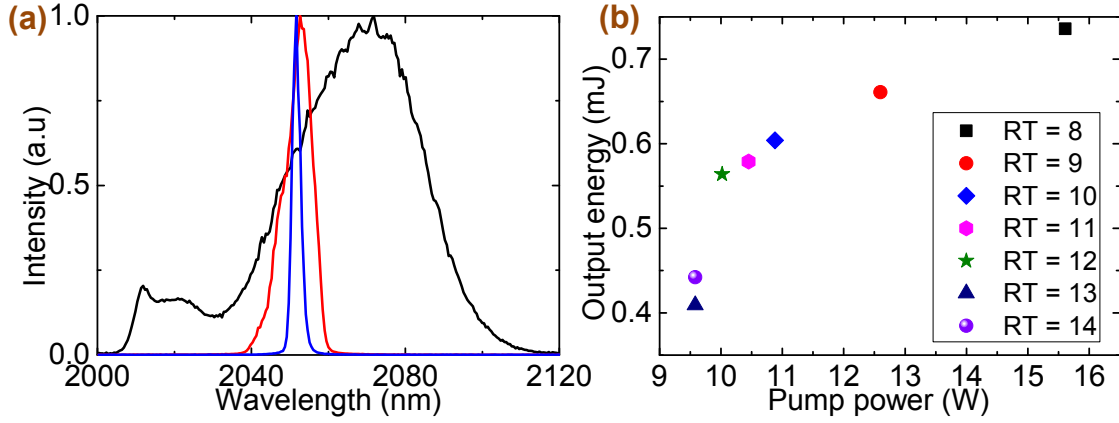
Figure 5.7: (a) Seed spectrum before (black) and after (red) CVBG stretcher while the amplified spectrum after RA + SPA is shown in blue, (b) output energy of the RA vs. pump power at different RT

then a long focal length lens was placed before the cavity, whose focus position was located at end mirror of the cavity. Though the available pump power was up to 25 W, only ∼13 W were used, to keep the output energy fluctuations low and avoid optical damage.

### 5.3.3   Results and discussions

The Pockels cell was gated between 102 ns - 174 ns, which correspond to 8 - 14 RT inside the RA cavity. The corresponding output energy was measured for different pump powers for each gate width and the results are shown in the figure 5.7. With an increase in the number of RT, pulse-to-pulse fluctuation increases, as the chaotic regime of bifurcation kicks in earlier [59, 56], limiting the output energy. With higher pump power, maximum possible energy with minimum fluctuations were obtained for lowest RT number of 8, that corresponds to gate width of 102 ns and with cavity RT time of 12 ns. For the higher number of RT, the pump power could not be increased furthermore, since the operation regime of RA went into a chaotic regime leading to increased fluctuations eventually resulting in damage of the optics [59, 60]. In the case of a lower of RT, it was necessary to pump the gain medium with higher power to reach a similar output pulse energy as that in the case of higher RT, which shifts the lower energy limit of the bifurcation point to even higher output pulse energies. This allows pumping the gain medium with increased pump power that result in low energy fluctuations, hence without damaging the optical components. To avoid any optical damage arising due to a chaotic regime, the RMS fluctuations
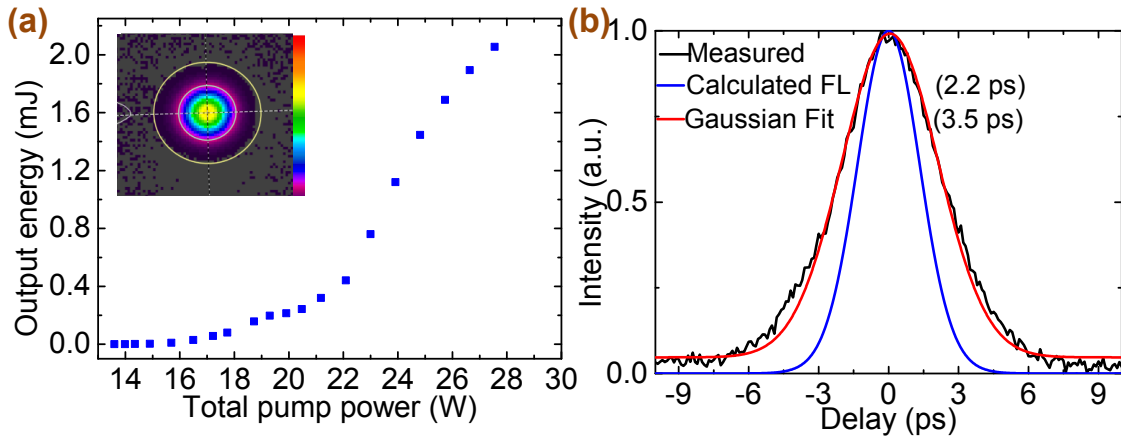
Figure 5.8: (a) Slope efficiency of RA + SPA for 8 RT inside the RA, (b) AC trace (black) with Gaussian fit (red) and the corresponding calculated AC of FL pulse.

of the pulses is not allowed to exceed 2 % during the measurement. In the case of 8 RT, pulse energies up to 730-$\mu$J was obtained directly from the RA for an absorbed pump power of 12 W. However, this limit comes due to the stretching conditions, by going to the double pass configuration in CVBG and stretching the pulse twice the present level can increase the damaging threshold of the RA and yield higher output energy. The pulse-to-pulse RMS fluctuations was $\sim$0.6 %, as recorded both by photodiode and energy meter.

The RA output was subsequently amplified in a single-pass booster amplifier (SPA). It also comprises of a 0.5 % Ho-doped crystal but with a length of 70 mm and small signal absorption of 99 % for p-polarization. It is pumped using the same Tm pump laser as that of RA from the second port of the PBS. It is to be noted here that the pumping the SPA with higher power and extracting more energy at the output is possible. But the mechanical design of the amplifier does not allow for independent regulation of the pump power in RA and SPA, separately. Hence the pump power limit in SPA was coupled by the RA itself. With a total of 27 W pump power into the RA (at gate width of 102 ns for a pulse repetition rate of 1 kHz) and SPA, a net output pulse energy of 2 mJ was achieved leading to a total gain of $\sim$107. Assuming a linear slope at higher power levels, a slope efficiency of 25 % was obtained (figure 5.8).

The pulses were then compressed using a second identical CVBG with a reversed chirp as that of the stretcher. With a compression efficiency of 88 %, output energy of 1.76 mJ and an average power of 1.76 W was obtained. The output beam profile was characterized using a pyroelectric camera (Pyrocam III, Ophir-Spiricon Inc.) and

exhibits Gaussian profile (inset in figure 5.8(a)). Autocorrelation (AC) measurements of the output pulse at a maximum output of 1.76 mJ are shown in figure 5.8 (b). The black curve shows the measured AC trace with a Gaussian fit (red) giving a FWHM of 3.4 ps. The blue curve shows the corresponding FL duration of 2.2 ps calculated from the spectrum. The residual chirp might originate from a mismatch of the CVBGs. Due to the gain narrowing in the amplifier, the output spectrum narrows down from a FWHM bandwidth of 8.2 nm (red curve) to 2.3 nm (blue curve) as shown in the figure 5.7. In the next subsequent sections, different schemes to reduce the gain narrowing effect and enhance output spectral bandwidth are discussed.

## 5.3.4 Bifurcation in Ho:YLF RA

One of the important aspect of high gain and high repetition rate RA design is its susceptibility to output pulse energy fluctuations attributed to pump fluctuations and other inherent noise sources [61]. Moreover, for the repetition rates close to or more than the inverse lifetime of the gain medium $1/\tau_{gain}$ , the output pulse energy can fluctuate periodically between two or more value differing by large factor and is called bifurcation regime of the RA operation as shown in the figure 5.9 (a) [60]. This is caused in high repetition rate RA operated below gain saturation due to disturbed equilibrium in the gain for the consecutive pump and amplification cycles (figure 5.9 (b)). It is possible to suppress the bifurcation regime even at high repetition rate by pumping the RA at increased power [62] [60] (figure 5.9 (c)). However, the onset of bifurcation is also affected by the seed energy. By increasing the seed energy, the bifurcation can be suppressed. An important question arises that whether it is possible to find a single-energy regime after the bifurcation point? First insight into this direction was presented in [60] for a Nd:YVO4 based RA. It was only recently, such regimes were studied for Ho:YLF RA [63]. A thorough simulation was presented in Ref. [64]. Some of the important results presented there are summarized in this section. It was found that there exists four different operation regimes that show different output pulse characteristics as shown in the figure 5.9. Regime ① demonstrates low repetition rate operation where no bifurcation instability exists. In regime ②, though bifurcation starts, the highest pulse energy is still in the single-energy regime. Regime ③ is completely in bifurcation regime where the highest pulse energy is in the instability regime and therefore limits the highest extraction energy possible. Regime ④, represents the region where bifurcation has been overcome and the single-pulse highest pulse energy appears before the onset

of bifurcation. The simulation results suggest that it was possible to shift regimes ① and ② to higher repetition rate, for increased pump intensities and higher seed fluences. These results indicate that the common knowledge about bifurcation i.e. the knowledge that the onset of bifurcation kicks in for repetition higher than the inverse lifetime ($1/\tau_{gain}$), is simply a limiting case of RA operating at low pump intensity and low seed fluence.
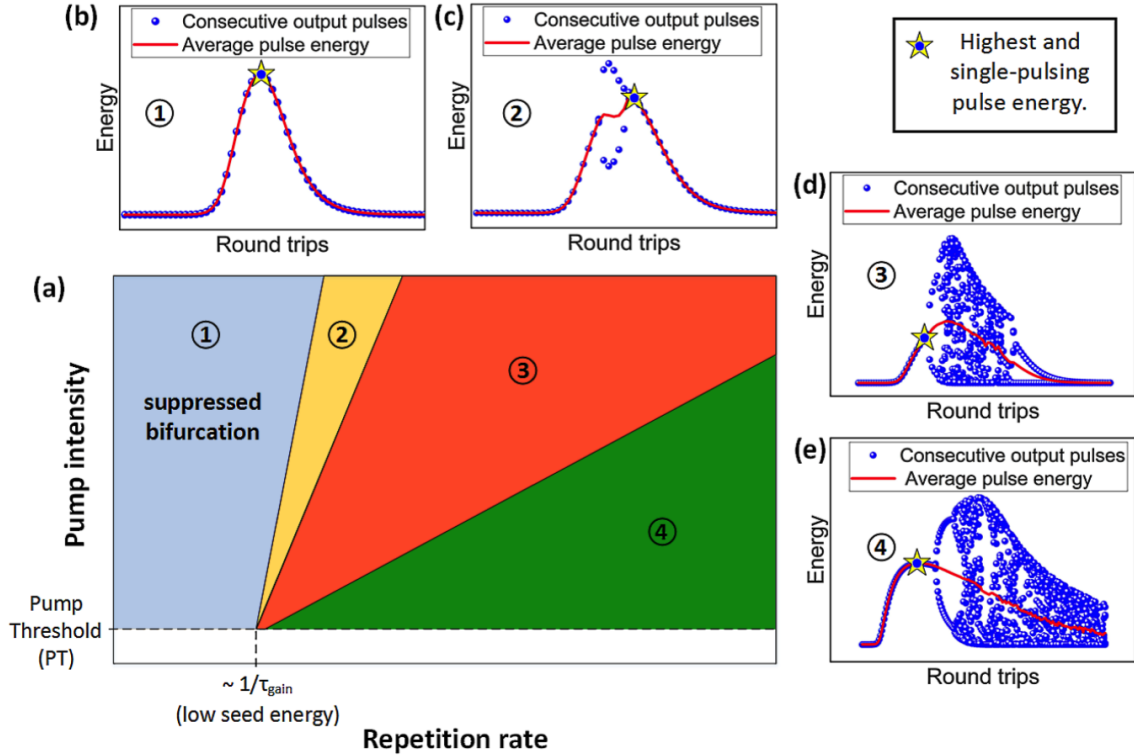


Figure 5.9: Regimes for RA operation depending on the repetition rate and pump intensity. Regime ① represents a bifurcation-free regime. In regime ②, high pulse energies an be extracted by operation beyond the bifurcation instability. In regime ③, the maximum pulse pulse energy at a single-pulsing RT is limited by the onset of the pulse instability. In ④, the maximum pulse energy at the single-pulsing RT can be extracted before the pulse instability. The bifurcation threshold separating regimes ① and ② coincides with $1/\tau_{gain}$ for low pump powers and low seed energies.

## 5.4  Intracavity gain shaping

In the previous section, we saw that the amplification of pJ-level femtosecond pulses to a mJ-level, led to reduced spectrum and lengthening of the pulse to picosecond at the output. Any Gaussian pulse, due to Heisenberg uncertainty principle has a minimum time-bandwidth product $\Delta\nu.\tau \geq 0.4$, where $\Delta\nu$ is the spectral bandwidth

and $\tau$ is the pulse duration at FWHM. Hence to amplify the pulse, each spectral components needs to be amplified equally by several orders of magnitude. However, any gain material has a finite gain spectrum which is not flat over its entire bandwidth, rather often has Lorentzian-shape linewidth. Therefore, the central frequencies of the spectrum sees higher gain than the frequencies in the wings, which causes the central frequencies to grow much faster than the wings, resulting in the narrower spectrum than the actual gain spectrum, thereby limiting the overall bandwidth leading to increased pulse duration at the output (figure **??**). This process is called gain narrowing. Gain bandwidth of a laser medium exhibiting Lorentzian profile, can be derived as [65]:

$$G(\omega) = exp\left[\frac{g_0}{1 + \left(\frac{2(\omega - \omega_0)^2}{\Delta\omega_a}\right)}\right] \tag{5.9}$$

where $g_0$ is the small signal gain given by

$$g_0 = \Delta N \sigma_{max} L = ln(G_0) \tag{5.10}$$

where $\Delta N$ is the population density, $\sigma_{max}$ is the peak of the emission cross-section as a function of $\lambda$, $L$ is the length of the gain medium and $G_0$ is the gain at the central frequency.

Therefore, gain bandwidth at FWHM can be written as:

$$G(\Delta\omega/2) = G_0/2 \tag{5.11}$$

where $\Delta\omega$ is the FWHM spectral bandwidth and substituting it in the equation 5.9, $\omega$ can be derived as

$$\Delta\omega = \Delta\omega_0\sqrt{\frac{ln(2)}{ln(G_0/2)}} \tag{5.12}$$

Therefore, all high gain amplifier systems suffer from gain narrowing thereby limiting the output pulse duration. An estimate of this gain-narrowed spectrum can also be obtained simply by exponentiating the frequency dependent gain profile by an amount equivalent to the total gain of the amplifier. This can be calculated
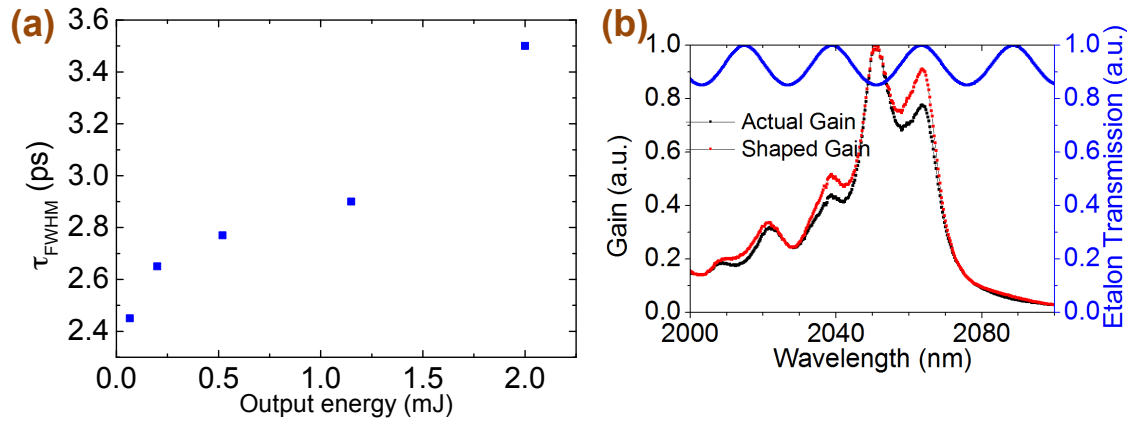
Figure 5.10: (a) Measured AC traces at different gain settings in the amplifier demonstrating the gain narrowing effect, (b) concept of intracavity gain shaping using matched transmission of etalon after every RT. Etalon transmission (blue) for 4 % etalon and 150 $\mu$m thick, measured single pass gain (black) and simulated etalon matched gain (red).

numerically or obtained experimentally from the unseeded amplified spontaneous emission (ASE) of the amplifiers as well. The measured AC trace from the Ho:YLF RA at different pumping level for a fixed RT number are shown in the figure **??** and in the legend is mentioned the obtained pulse duration assuming sech$^2$ shape and the pulse energy. As seen, an increase in pump power (i.e. increase in total gain) leads to an increase in gain narrowing leading to the longer pulse duration. For different output energy of 0.066, 0.2, 0.52, 1.15 and 2.0 mJ, we obtained the pulse duration (FWHM) of 2.45, 2.65, 2.77, 2.9 and 3.4 ps, respectively. The pulse duration increased from 2.4 ps at low energy to 3.4 ps at the maximum energy of 2 mJ, with the gain narrowing severely limiting the output spectrum.

### 5.4.1   Methods to reduce gain narrowing effect

**Pre-shaping of the seed spectrum**

One of the commonly used technique to reduce the effect of gain narrowing is by pre-shaping the seed pulses. In this method, the low energy seed spectrum is shaped in spectral domain using mechanical pulse shaper at the specific center wavelength where the gain is high in the amplifier. Thus during amplification in the amplifier, this part starts with lower seed energy and thus it undergo less amplification as compared to other parts of the spectrum. This leads to an overall effect of reduced

gain narrowing. This has been demonstrated at 800 nm wavelength several years back. Recently, this was shown in Ho:YAG RA at 2 $\mu$m delivering sub-ps, mJ-level pulses [39]. In this case, the gain narrowing was compensated by using mechanical pre-shaping of the seed pulse and thereby compressed the pulse duration from 3.5 ps to 530 fs. Spectral pre-shaping was demonstrated for RA with a total gain of 2 - 3 orders of magnitude less than in the system presented here. In the case of a high-gain system, spectral pre-shaping is not easy to implement, as the spectral attenuation required is also very high and thus precise control of the attenuation coefficient is limited.

**By spatially dispersive element**

It was proposed by Christov et al [66] that gain narrowing can be reduced by spatially dispersing the beam in the gain medium. This reduces the competition between each wavelength as they experience different path length for each wavelengths, and hence each wavelength sees an independent gain from each other. This can be achieved by using two prisms as a dispersion line and a one-to-one telescope that makes a Fourier plane at the crystal. This introduces a spatial distribution of the pump beam in the gain medium. The benefits of this approach include dispersion control, effecient cooling of the gain medium, large mode area resulting in better extraction efficiency. This method have also been exploited only for Ti:Sapp systems at 800 nm [67].

**Intracavity gain shaping**

Since amplification in any amplifier occurs in discrete steps through multiple passes in the gain medium, the amount of gain narrowing depends on the number of passes through the gain medium. Hence, though the net amplification in these amplifiers is large ($\sim 10^8$), amount of amplification after every RT is typically small ($\sim 2 - 4$). Therefore, the amount of gain narrowing after any one RT is also small and the net gain narrowing can be controlled using a frequency dependent filter that selectively attenuates and re-shapes the pulse spectrum after each RT. In the next section, the descriptive study of intracavity gain shaping method for Ho:YLF RA are presented.

## 5.4.2   Intracavity gain shaping

This method of spectral shaping is more elegant and simple to use as compared to the pre-shaping of the seed-pulse, that in any way is not feasible for a high-gain system. Moreover, it also offers precise control of the attenuation for every frequency and was first proposed by Barty et al in 1996 [65]. The frequency filter can be a birefringent filter or an etalon. A thin Fabry-Perot etalon with a moderate modulation depth is a good choice. In the etalon approach, since the shaping occurs every RT, only a small amount of attenuation is required, hence there exist better control over etalon parameters and thus better control of the shaping. The control parameters accessible with an etalon are, its thickness that controls free spectral range, the angle that controls the positioning of maxima and minima of the etalon transmission and surface reflectivity that controls the attenuation coefficient. Birefringent filter has been used by Leng et al in Ti:Sapp system as well [68]. However, there has been previously no study of such shaping in Ho:YLF amplifier at 2 $\mu$m. In this work, we employ spectral filters based on etalon for the first time inside the 2-$\mu$m Ho:YLF RA to reduce the effect of gain narrowing.

## 5.4.3   Simulations: Optimum etalon parameters

In order to identify the optimum etalon parameters needed to reduce or suppress the effect of gain narrowing, simulations were performed by Peter Kroetz. In this section, the simulation model according to which the etalon parameters were chosen are presented. The complete details of the model can be found in Ref. [69]. The simulations were based on adapted chromatic Frantz-Nodvik equations considering the spectral effects in the amplifier. In this model, the pump and the seed fluence was sliced into several small slices and the propagation of each slice in the gain medium was simulated consecutively for each pass until the pulses were switched out. The schematic of the model is shown in the figure 5.11. In the spectral domain, for $i_{th}$ slice, the single-pass gain, the cross-sections, and fluences can be expressed as:

$$G_{i-1}(\lambda) = exp(\sigma_{g,i-1}(\lambda)NL) \tag{5.13}$$

$$\sigma_{g,i-1}(\lambda) = \beta_{i-1}(\sigma_{em}(\lambda) + \sigma_{abs}(\lambda)) - \sigma_{abs}(\lambda) \tag{5.14}$$

$$J_i(\lambda) = J_{sat}(\lambda)T(\lambda)ln(1 + G_{i-1}(\lambda)exp\left(\frac{J_{i-1}(\lambda)}{J_{sat}(\lambda)}\right) - 1) \tag{5.15}$$
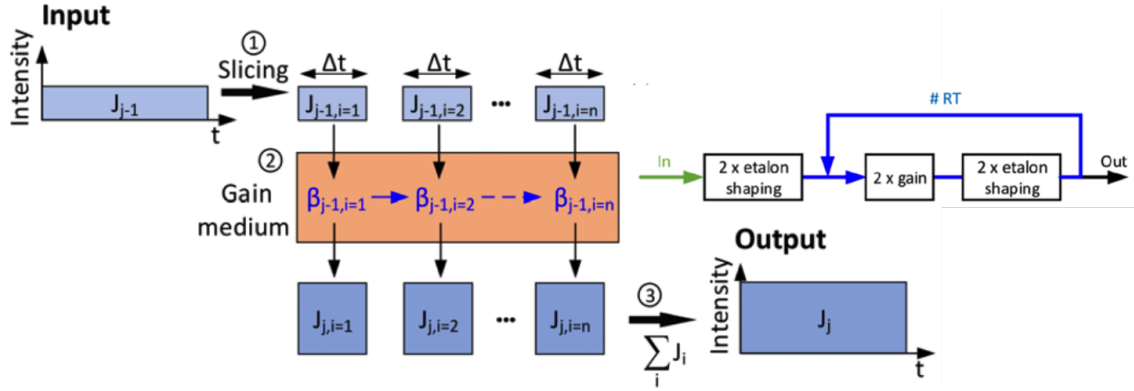
Figure 5.11: Schematic of the simulation model for a single-pass of fluence $J_{i-1}$ through the gain medium. The incoming fluence sliced into $n$ equal fluence slices and each slice passes consecutively through the gain medium in which the inverted fraction $\beta$ is updated after each pass. Finally, total output fluence is obtained by summing up each fluence slices

where $J_{sat}$ is the saturation fluence given by:

$$J_{sat}(\lambda) = \frac{hc}{\lambda(\sigma_{abs}(\lambda) + \sigma_{em}(\lambda))} \tag{5.16}$$

$\beta_{i-1}$ is the average global inverted fraction, $\sigma_{em}(\lambda)$ and $\sigma_{abs}(\lambda)$ are the absorption and emission cross-section, $N$ is the density of dopant ion, $L$ is the length of the gain medium, $c$ is the speed of light, $h$ is the Plank constant, $T(\lambda)$ is the single pass transmission loss. Since the model is based on updating the inverted fraction $\beta$ instead of updating gain, the above equation can be converted to:

$$\beta_i = \beta_{i-1} - \frac{\int \left[ \lambda \left( \frac{J_i(\lambda)}{T(\lambda)} - J_{i-1}(\lambda) \right) \right] d\lambda}{hcLN} \tag{5.17}$$

And in order to account for the inversion decay losses for CW pumping, inverted fraction can be written as:

$$\beta_i^* = \beta_i exp \left( -\frac{\Delta t}{\tau_{gain}} \right) \tag{5.18}$$

where $\tau_{gain}$ is the upper level lifetime, $\Delta t$ is the time duration of the sliced fluence.

The wavelength dependent etalon transmission $T_{etalon}(\lambda)$ is modeled as a function of the surface reflection $R$, the etalon thickness $L$ and the etalon angle $\theta$ [70]

$$T_{etalon}(\lambda) = \frac{1}{1 + \frac{4R}{(1-R)^2}sin^2\left(\frac{\pi}{\lambda}nLcos(\theta)\right)} \tag{5.19}$$

where $n$ is the refractive index of the etalon material and $\theta$ is the etalon angle.

The consecutive order sliced fluences, the amplifier gain and the etalon filtering is shown in the figure 5.11. In the model, first, the beam passes through the etalon two times, and two times through the gain medium corresponding to two passes in one RT and then finally two times again through the etalon before it is ejected out. The modeling needs to be carefully optimized for the position where the etalon is placed in the cavity. As seen in the equation 5.19, the transmission function of an etalon is sinusoidal in nature whose period depends on thickness. The frequency of the etalon can be tuned by the thickness of the etalon, while the modulation depth can be controlled by the surface reflection. By tuning the angle of incidence, the wavelength position of the attenuation can be tuned. Therefore, if the reflectivity and thickness are carefully chosen such that the single pass gain at the peak wavelength can be compensated for the gain narrowing effect after each RT, the output spectrum can be broadened. Theoretical realization of this concept is shown in figure **??** (b). The black curve shows the measured single pass gain from the RA while the blue curve shows etalon transmission. The incident angle of the etalon is tuned such that the highest attenuation point coincides with the gain maximum at 2051 nm i.e. the transmission dip matches the gain peak (figure **??** (b)). The simulation results for different thickness of etalon and angle of incidence are shown in the figure 5.12. Figure $b$ and $c$ shows the vertical cut and as seen in $c$, the spectral FWHM periodic with etalon thickness and for every 0.7 $\mu$m, there exists a maximum and the width of each period is very narrow (0.1 $\mu$m). Hence thus manufacturing the etalon with such tolerance level is not feasible. However, as also seen by tuning the angle of the etalon, the spectral peak can be shifted making it possible to align the etalon of any thickness and still obtain the right spectral peak.
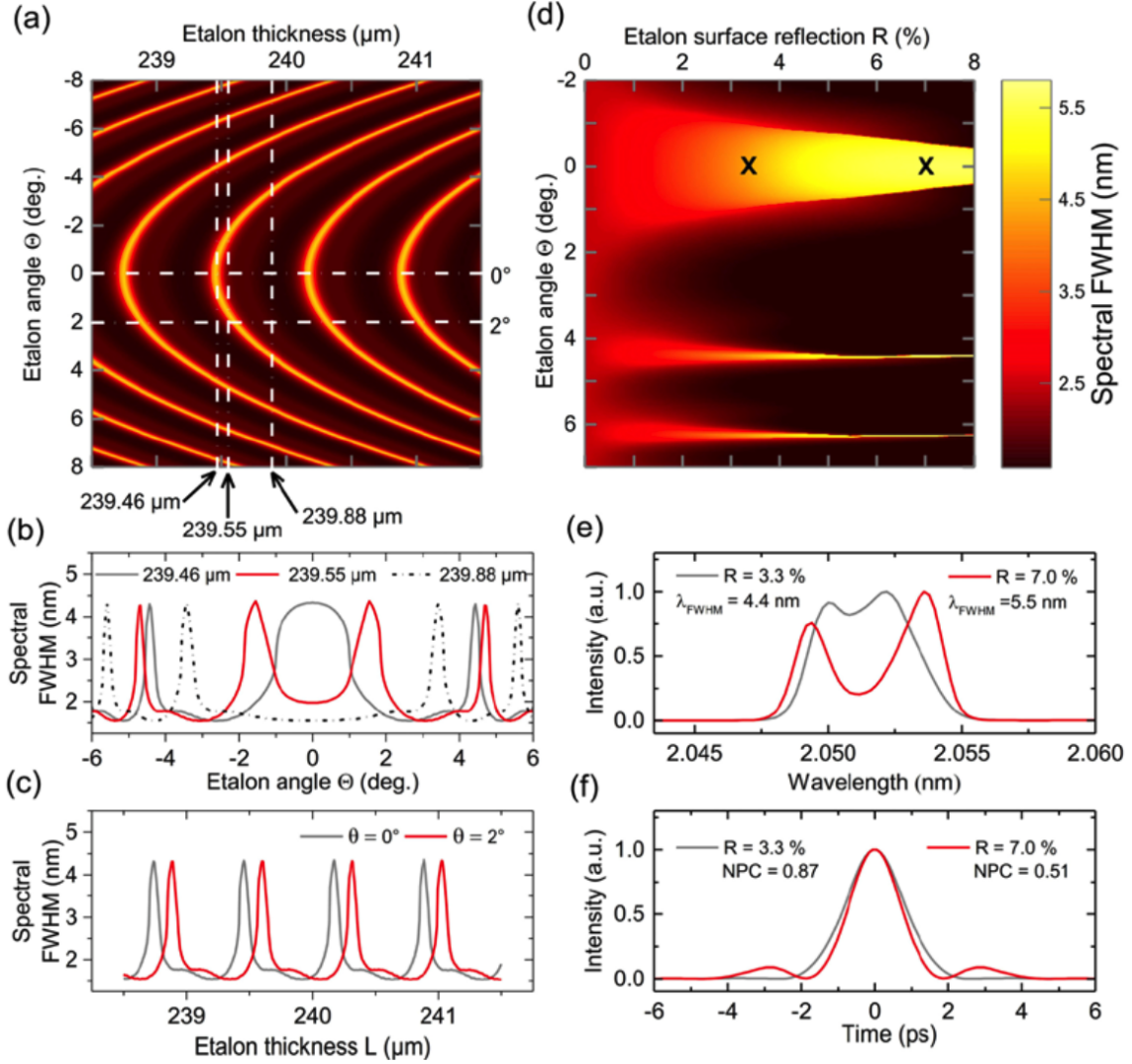
Figure 5.12: Simulation results for etalon parameter scan over thickness $L$, angle $\theta$ and surface reflection $R$. (a) Etalon thickness versus angle for $R = 3.3$ %, (d) surface reflection versus angle for $L = 239.46$ $\mu$m, (b) and (c) presents the cut through (a) for etalon angle and thickness, respectively, (e) shows the spectra at the two position of cross mark in (d) and their corresponding calculated FL duration in (f)

## 5.4.4 Experiment

To reduce the effect of gain narrowing effect during amplification in the RA, an etalon E was inserted in the cavity as shown in the figure 5.13. To experimentally realize this concept, initial angle alignment was done by looking at the fluorescence spectra before lasing threshold, and tuning the etalon angle for off-resonance. This enhances the effective gain bandwidth at the expense of reduced gain. However, as seen from the simulation results the etalon angle is very sensitive to the alignment, hence the final tuning was done in real time, while monitoring the output spectrum
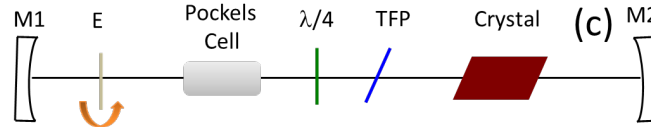
Figure 5.13: Schematic of an RA cavity with Etalon (E) placed close to the end mirror

during RA operation. Though, one needs to be very careful during this fine tuning as the intracavity losses are very sensitive to this tuning effect and might lead to damage of the amplifier. The free-running spectrum of the RA cavity was 2.9 nm. During the etalon tests, the number of RT in the RA was kept constant to RT number 8 and the pump intensity was adjusted such that the RA produced $\sim$500 $\mu$J energy pulses without running into the bifurcation regime or any damage. Since the surface reflection of a material depends on its refractive index, we used three different materials UVFS, n-SK$_2$, n-BaSF$_2$, whose refractive indices ($n$) were 1.448, 1.583, 1.631 and the corresponding surface Fresnel reflections at normal incidence were 3.3 %, 5.1 % and 5.75 %, respectively. We also tested the effect of different thickness for UVFS of 200 $\mu$m, 0.24 $\mu$m and 300 $\mu$m

## 5.4.5   Results and discussions

To study the effect of modulation depth on the effective emission spectrum, etalons of different reflectivities were tested. These etalons were chosen to give broadest spectra based on the numerical simulations presented the previous section. The measured output spectrum (solid lines) and simulated spectrum (dotted lines) with and without etalons of different reflectivity are shown in the figure 5.14 (a), which closely matches for all cases. In each plot, the angle of the etalon is tuned at maximum pump power such as to give the broadest spectrum and least dip in the spectrum, as this eventually can result in the smallest wings in their corresponding temporal profile. For all configurations, the best flat-top spectrum without any dip was obtained with the etalon of $R = 3.3$ % gives. The dip increases for higher reflectivities, as the modulation depth increases. The corresponding measured AC traces for each reflectivity are shown in figure 5.14 (b) along with their calculated FL (dotted lines). Clearly, UVFS with $R = 3.3$ % gives the broadest spectrum with a FWHM of 5.4 nm without any spectral wings (black curve in the figure 5.14 (a)) whose AC trace (black curve in the figure 5.14 (b)) with Gaussian fit gives a FWHM of 2 ps without any wings. Hence the pulse from the RA (without SPA) of FWHM of 3.4 ps was
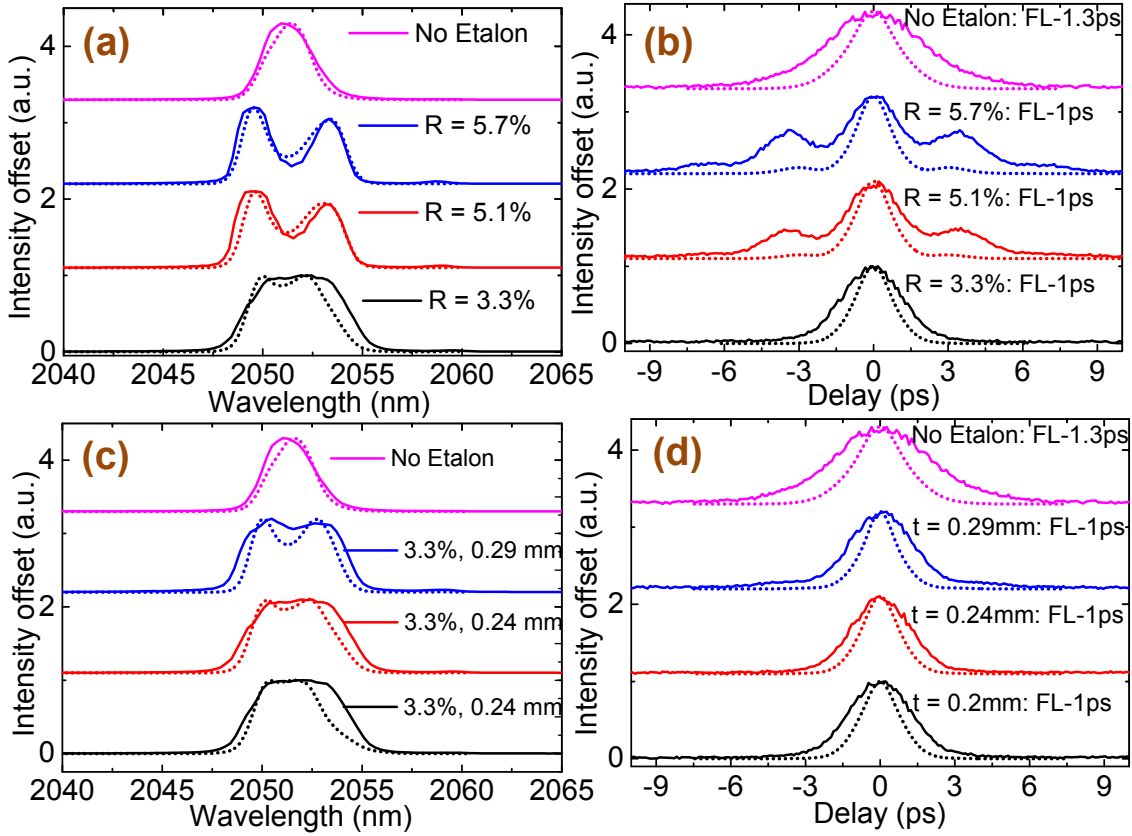
Figure 5.14: (a) Measured (solid) and simulated spectra (dotted) without etalon and with etalon of reflectivity 5.7, 5.1, 3.3 %, (b) AC traces for the spectra in (a) and their calculated AC of the FL pulse, (c) measured (solid) and simulated spectra (dashed lines) for R = 3.3 % and thickness of 0.2, 0.24 & 0.3 mm, respectively, (d) AC trace for the spectrum shown in (c) and the calculated AC of the FL pulse.

compressed down to 2 ps thereby reducing the pulse duration by 30 %. It should be noted here that the FL duration in all cases remains the same i.e. ∼1 ps as the spectral bandwidth is the same for all reflectivities, though the wings start to appear for higher reflectivities. We also studied the effect of etalon thickness on the output spectrum for a fixed reflection, which in this case was $R = 3.3$ %. Figure 5.14(c) shows the measured optical spectra for UVFS etalons with thickness 0.2, 0.24 and 0.3 mm and the corresponding AC traces in the figure 5.14 (d). Here again, the maximum spectral FWHM obtained was 5.4 nm. The calculated AC of the FL is also shown as dotted lines (figure 5.14 (d)). It can be seen that irrespective of the thickness, the output pulse did not change.

With the etalon ($R = 3.3$ % and $t = 0.29$ mm) in the RA cavity, the output pulse was seeded into the SPA where the spectrum was again subject to gain narrowing. Due to increased gain narrowing, the etalon angle, which was aligned initially only
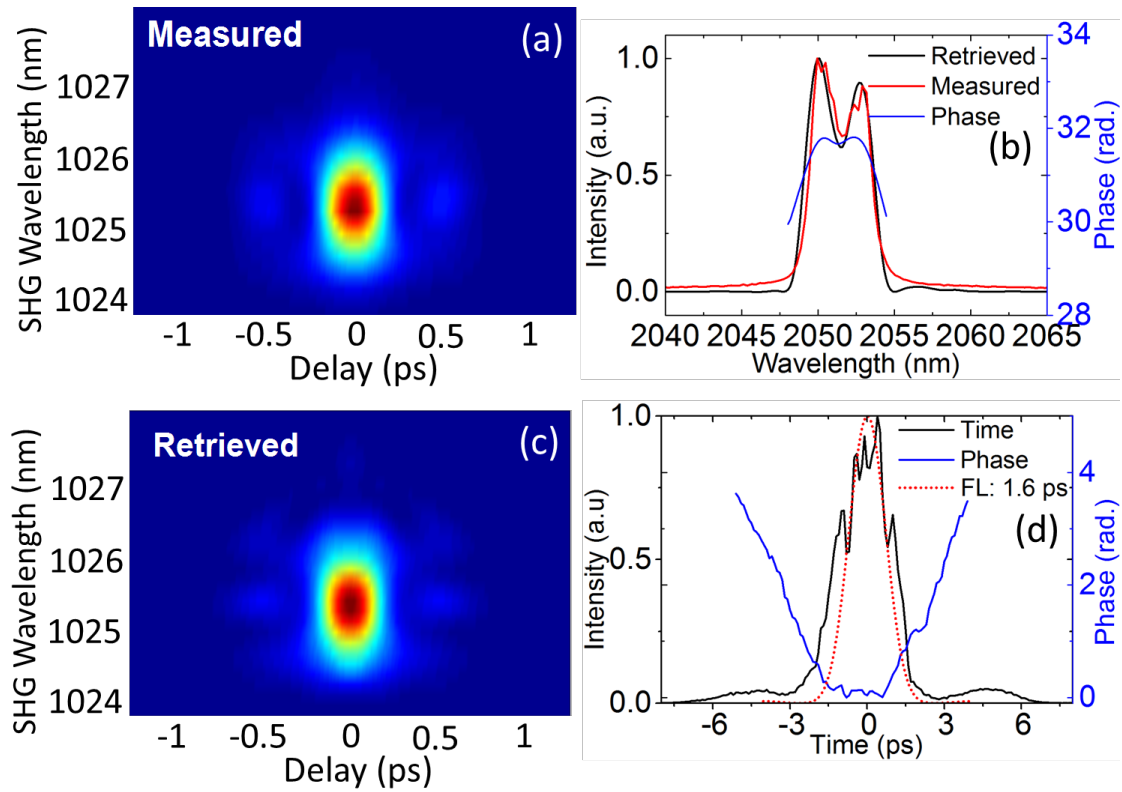
Figure 5.15: (a) & (c) Measured and retrieved FROG trace, (b) measured (red) and retrieved (black) spectrum with spectral phase (blue), (d) retrieved temporal profile (black) and corresponding phase (blue)

for RA cavity was detuned later to optimize for the broadest output spectrum of the SPA with minimum wings. AC reveals that the pulse duration increased from 2 ps (in RA) to 2.4 ps (RA + SPA). Due to the etalon-induced losses, a higher pump power was required to compensate for this loss to keep the output energy same at a fixed number of RT. Furthermore, this lead to an increased pump power in the SPA thereby extracting higher total output energy of 2.2 mJ. However, due to unstable bifurcation regime, the system was not optimized for higher gain and hence the dip in the spectrum could not be compensated for 5.1 % and 5.7 % etalon. Furthermore, this approach can also be applied to RAs with higher gain thereby overcoming the losses induced due to the etalon at 2051 nm.

The final output was characterized using a home built second harmonic generation frequency - resolved optical gating (SHG-FROG) setup. The results are shown in figure 5.15. The electric field reconstruction was carried out on a $256 \times 256$ grid size which converged to a FROG error of $5 \times 10^{-3}$. Figure 5.15 (a) and (c) shows the measured and retrieved FROG traces that match well. The validity of FROG reconstruction was also checked with independently measured spectrum (red) shown

in figure 5.15 (b), revealing that the FROG retrieval (black) is in good agreement with the measurement. The retrieved smooth spectral phase (blue) suggests that there exists remaining chirp, arising due to mismatch of the CVBG used for stretcher and compressor. Due to the flat spectral phase at the output, an extra loss-less prism compressor can be used in addition to the CVBG, to compensate for the remaining chirp and compress the pulse to FL duration. Alternatively, the same CVBG can also be used to stretch and compress the pulse, thereby avoiding any temporal mismatch of the CVBG's. Figure 5.15(d), shows the retrieved temporal profile (black) with the phase (blue), and the FL (dotted) of the measured spectrum. The FROG retrieved pulse duration after RA + SPA was 2.4 ps and the calculated FL duration was 1.6 ps.

### 5.4.6 Conclusions

In conclusion, we presented in this chapter, a compact seeding and amplification of low energy pJ-level energy to mJ-level from Ho:YLF based regenerative amplifier and single pass amplifier at 2 $\mu$m wavelength. The system was seeded with a home-built seed oscillator having a pulse energy of 60 pJ. The 60 pJ seed energy was amplified to 0.5 mJ in the RA. The stretching and compression using CVBG provided reliability and compact seeding. The output was further amplified via SPA to 2.2 mJ and after compression in CVBG, we obtained the pulse duration of 3.4 ps at 1 kHz repetition rate and < 1 % RMS fluctuations. Using intracavity gain shaping with an etalon in the RA cavity, we were able to increase the spectral bandwidth from 2.9 nm to 5.4 nm that supports a minimum of 1 ps Fourier Limit (FL) duration. Together with SPA, we achieved 30 % reduction in the pulse duration from 3.4 ps to 2.4 ps beyond the gain narrowing limit. This has been the record result for the shortest pulse duration achieved from Ho:YLF RA together with a SPA both without gain shaping i.e. 3.4 ps and with gain shaping i.e. 2.4 ps.

# Part II

# Few-Cycle Pulse Generation

# Nonlinear Pulse Compression

## 6.1   Introduction

When an ultrashort pulse propagates in an optical fiber, due to high intensity several nonlinear effects are excited, like self-phase modulation (SPM), stimulated Raman Scattering (SRS), four wave mixing (FWM). In combination with dispersive effects, several other novel phenomena arise, like soliton formation and supercontinuum generation. These processes give rise to new frequencies and with proper dispersion management, shorter pulses than at the input can be generated. This method of pulse compression which involves a nonlinear process for spectral broadening followed by dispersion management is called nonlinear pulse compression. Nonlinear pulse compression in a waveguide is a common approach for the generation of femtosecond pulses whose spectrum is limited by the gain-bandwidth of the amplifier system. Ideally, SPM can be induced, simply by focusing an intense light beam into a bulk nonlinear medium, however, it also gives rise to self-focusing and small instabilities that can make the pulse not usable. Moreover, the energy conversion efficiency of new frequencies are low. These issues can be avoided by SPM in a waveguide or fibers. Despite the fact that silica material, commonly used for fibers, exhibits 2 - 3 orders of magnitude lower nonlinear refractive index than other commonly used nonlinear medium, fibers are advantageous due to the possibility of confining light into a small core and guide it

to a long distance. Due to small a mode size and extremely low loss of these fibers, it is possible to increase the effective length in which the nonlinear interaction takes place by several orders of magnitude. Figure of merit (FOM) is a measure of the performance or the efficiency of any process, hence for comparison, let us consider the figure of merit $FOM_{bulk}$ and $FOM_{fiber}$ for both bulk and fibers, respectively.

$$FOM_{fiber} = I_0 L_{eff} = \left(\frac{P_0}{\pi w_0^2}\right)\frac{\pi w_0^2}{\lambda} = \frac{P_0}{\lambda} \tag{6.1}$$

$$FOM_{bulk} = I_0 L_{eff} = \int_0^1 I_0 exp(-az)dz = \frac{P_0}{\pi w_0^2 a}(1 - e^{-al}) \tag{6.2}$$

where, $I_0$ is the input intensity, $L_{eff}$ is the effective length of the medium, $P_0$ is the peak intensity, $\lambda$ is the wavelength, a is the absorption coefficient, $w_0$ is the beam waist size. Hence the FOM of the fiber improves in comparison bulk medium by a factor of:

$$\frac{FOM_{fiber}}{FOM_{bulk}} = \frac{\pi w_0^2 a}{\lambda} \tag{6.3}$$

The spectral broadening phenomena in fibers can be broadly categorized into two different regimes depending on the input pulse duration: *femtosecond regime (FR)* and *picosecond regime (PR)*. Although SPM plays a significant role in both these regimes, fundamentally different higher-order effects become significant depending on the pump pulse and fiber parameters. In FR, when pumping in normal group velocity dispersion (GVD), spectral broadening is dominated by SPM, while in anomalous GVD, soliton fission and Raman interactions dominate. However, in PR spectral broadening cannot be solely explained in terms of SPM and soliton-fission. Though, under PR, in normal GVD, SPM still dominates. In the case of anomalous GVD, as the input pulse duration increases, a phenomenon called modulation instability (MI) and the FWM process play significant roles in the initial dynamics of pulse propagation in the fiber, where the fast modulation on the pump pulse in the time domain can subsequently lead to break-up of the pulses leading to a train of femtosecond soliton-like pulses. It has also been shown that Raman-soliton self-frequency shifting and dispersive wave generation are also present and it can be said that the soliton related dynamics in anomalous GVD range are similar in both FR and PR. An elaborate review about this can be found in Ref. [71].

Nonlinear spectral broadening can be achieved using various solid-core step-index

fibers, but the input energy is limited to nJ-level and the possibility of FWM restricts the spatial and temporal quality of pulse compression. Spectral broadening can also be achieved in noble gas-filled hollow capillaries where the gas acts as a nonlinear optical medium and the hollow capillaries acts as a waveguide with a leaky mode. However, due to low transmission coefficient, they require large core diameters ($\sim$200 $\mu$m) and hence high input peak power ($\sim$GW) is required for a significant amount of spectral broadening, and reducing the core size have the drawback of reduced throughput efficiency. Gas filled hollow-core photonic crystal fiber (HC-PCFs) offers significant down-scaling of core-size and at the same time offers low transmission loss with broad transmission bandwidth.

HC-PCFs first demonstrated by Cregan [72], mainly consist of optically guiding air-filled hollow core surrounded by an arrangement of micro-scaled silica tubes running along their length. However, they exhibit large optical field overlap with the silica core-surround, which limits their pulse energy handling capacity to a few 10's of micro-joule. HC-PCFs are mainly based on either photonic bandgap (PBG) or inhibited coupling (IC) [73]. In the last decade, new light guidance mechanism in HC-PCFs have emerged, namely, IC [74]. In PBG-guiding the core guided optical modes are prevented from coupling to the cladding via absence of the cladding modes at the frequencies and effective indices of the core modes (i.e. existence of photonic bandgap). Whereas, in IC-guiding HC-PCF also known as Kagome fiber, the non-coupling of core-guided light with the cladding, relies on the strong reduction of the optical field overlap between the modes residing in the core and those residing in the cladding. This strong core-clad coupling inhibition is a result of a strong transverse mismatch between the core and cladding modes and a tighter confinement of the silica cladding modes within the silica web structure. This also eventually results in enlarged fiber core diameter, low dispersion and broad transmission bandwidth [75, 76]. Thus, IC-based HC-PCFs are of beneficial over both hollow-capillaries and PBG-based fibers, guiding light over a large bandwidth at an energy of much higher damage threshold. In recent years, these fibers have demonstrated a dramatic reduction in transmission loss and record-breaking pulse-energy handling and compression [77] of up to 1-mJ 600-fs Yb laser beam handling [78]. Furthermore, these fibers filled with gasses also support a variety of nonlinear optical interactions other than SPM that includes third-harmonic generation [79] and extreme nonlinear phenomena like HHG [80, 81].

## 6.2   Pulse propagation in optical fibers

To understand the quantitative picture of these nonlinear process, one needs to start with Maxwell's equation. The following analysis is adapted from Ref. [82]. Assuming a simple case of pulse propagation in a nonlinear medium, i.e. a linearly polarized wave in x-axis, propagating in solid core fiber, the electric field takes the form of:

$$E(r,t) = \frac{1}{2\pi} \int_{-\infty}^{\infty} \widehat{x} F(x,y,\omega) \overline{a}(0,\omega) exp(i[\beta(\omega)z - \omega t] d\omega) \qquad (6.4)$$

where, $\widehat{x}$ is the unit vector along x-axis, $\omega$ is the frequency, F represents the spatial distribution of the fiber at x and y co-ordinates. $\beta(\omega)$ is the propagation constant that can be expanded using Taylor series as:

$$\beta(\omega) = \beta_0 + (\omega - \omega_0)\frac{d\beta}{d\omega} + \frac{1}{2}(\omega - \omega_0)^2 \frac{d^2\beta}{d\omega^2} + ..... \qquad (6.5)$$

Higher order terms can be included depending on the pulse bandwidth. This suggests that due to the frequency dependence of the propagation constant $\beta(\omega)$, each spectral component of the input field acquires different phase shift. By combining the above equation and applying the slowly varying approximation, electric field can be written as:

$$E(r,t) = \widehat{x} F(x,y,\omega_0) A(z,t) exp(i[\beta_0 z - \omega_0 t]) \qquad (6.6)$$

By using Maxwell's equation and including both Kerr and Raman contribution to the nonlinear polarization induced by light under slowly varying pulse envelope, and neglecting fiber losses $\alpha$, the nonlinear Schrödinger (NLS) equation can be written as:

$$i\frac{\partial A(z,T)}{\partial z} - \frac{\beta_2}{2}\frac{\partial^2 A(z,T)}{\partial T^2} + \gamma|A|^2 A \qquad (6.7)$$

where $T$ is the transformed time given by $T = t - \frac{d\beta}{d\omega}z$, parameter $\beta_2$ is related to dispersion and $\gamma$ is related to nonlinearity given by:

$$\beta_2 = \frac{d\beta}{d\omega} \tag{6.8}$$

$$\gamma = \frac{\omega_0 n_2(\omega_0)}{cA_{eff}} \tag{6.9}$$

In this context, $N$-parameter called as soliton number is usually defined which is related to the ratio of linear (dispersion) and nonlinear length given by:

$$Linear \quad Length \quad (L_D) = \frac{T_0^2}{|\beta_2|} \tag{6.10}$$

$$Nonlinear \quad length \quad (L_{NL}) = \frac{1}{\gamma P_0} \tag{6.11}$$

$$N = \sqrt{\frac{L_D}{L_{NL}}} = \sqrt{\frac{\gamma P_0 T_0^2}{|\beta_2|}} \tag{6.12}$$

For simplified solution of the NLS equation, if the dispersion length is quite long as compared to nonlinear length, dispersive effects can be neglected and equation 6.7 can be solved analytically and its solution can be derived as:

$$A(z,T) = \sqrt{P(z,T)}exp(i\phi(z,T)) \tag{6.13}$$

where $P$ and $\phi$ is the power and phase of the pulse can be derived as:

$$P(z,T) = P(0,T)exp(-\alpha z) \tag{6.14}$$

$$\phi(L,T) = \phi(0,T) + \gamma P(o,T)L_{eff} \tag{6.15}$$

Hence because of the nonlinear term $\gamma$, the pulse modifies its own phase that depends on the peak intensity and the process is called SPM. This gives rise to new frequencies whose instantaneous frequency $\delta\omega$ is given by:

$$\delta\omega(T) = -\frac{\partial\phi_{NL}}{\partial T} \tag{6.16}$$

where $\phi_{NL}$ is the nonlinear phase phase shift resulting from SPM given by:
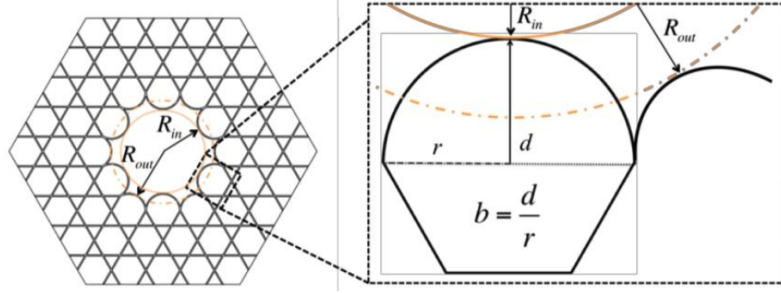
Figure 6.1: (a) Structure of a hypocycloid-like HC-PCF, (b) definition of the parameters quantifying the curvature of the core arc (figure reproduced from [6])

$$\phi_{NL}(L,T) = f_P(T)\left(\frac{L_{eff}}{L_{NL}}\right) \tag{6.17}$$

Here, $f_P(T) = P(0,T)/P_0$ determines the shape of the pulse in time and $P_0$ is the peak power at central frequency $\omega_0$, $\delta\omega$ is the frequency chirp that suggest, as the pulse propagates along the fiber, new frequencies are generated continuously leading to chirped broadened spectrum at the output, keeping the pulse shape unchanged.

However, when dispersive effects are present, as mostly is the case for real fibers, both the spectrum and pulse shape change, as the pulse propagates along the fiber. In the case of normal dispersion ($\beta_2 > 0$), the pulse broadens while in the case of anomalous dispersion ($\beta < 0$), optical solitons are formed. This is true for the special case to the solution of equation 6.7 with $0.5 < N < 1$ and fundamental solitons are formed. However, if $N > 1.5$, the input pulse is split up into higher order solitons whose shape and spectrum reproduce with a soliton period of $\pi/2$. Lastly, if the soliton number $N > 10$ in a highly nonlinear fiber, then the input spectrum undergoes extreme broadening and is called supercontinuum (SC) generation.

## 6.3   IC based HC-PCF: Kagome fiber

In the figure 6.1, the hypocycloid-core contour of Kagome lattice is shown. The hypocycloid-core contour whose curvature is quantified as $b$-parameter is a result of missing cells of triangular arrangement (which in is this case is 7) of circular tubes. The core-contour is formed by two alternating arcs, resulting in two circles of radii $R_{in}$ and $R_{out}$. The circle of radius $R_{in}$ is tangent with 6 most inward arcs while the circle of radius $R_{out}$ is tangent with 6 most outward arcs. The curvature $b = d/r$, where $d$
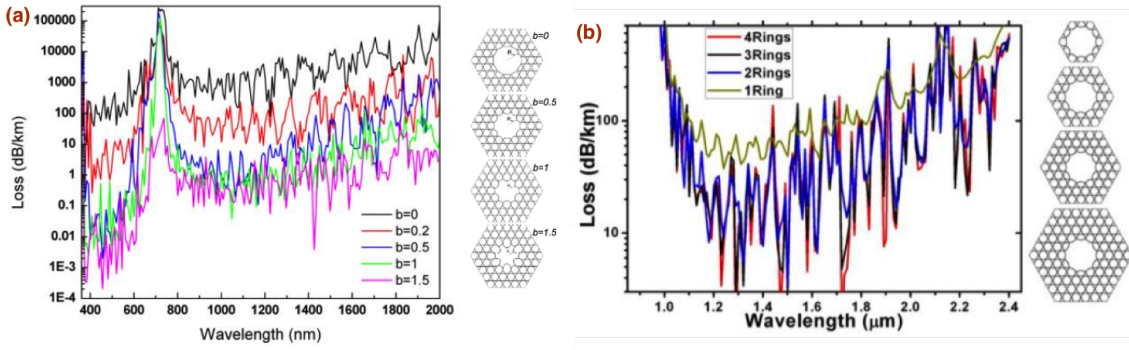
Figure 6.2: Simulated transmission loss (a) for various b = 0, 0.2, 0.5, 1, 1.5 and (b) for different number of ring 1, 2, 3 and 4 (figure reproduced from [6])

is the distance between the top of the arc and the chord joining the nodes connecting the inward arc to its neighboring ones, while $r$ is the half of the chord length. Thus with this definition, $b = 0$ corresponds to 'classical' Kagome fiber (quasi-circular core), while $b = 1$ corresponds to 'modified' Kagome fiber i.e. core contour with a circular shape. For $b > 1$, the inward arcs have an elliptical shape whilst the outward ones are set to have a circular shape. The figure 6.2 (a) shows how the curvature parameter $b$ affects the transmission loss. Similarly, figure 6.2 (b) shows the propagation loss curve for different number of cladding ring [6]. Negative curvature is very newly developed HC-PCF, whose core wall has an inverted curvature and usually exhibits multiple spectral transmission bands of low attenuation [83]. They have a flexibility of tailoring the fiber for specific wavelengths and application. The development of PCFs has speeded up its application immensely [84]. Benabid and co-workers first reported the development of a new type of PCFs called Kagome fiber [85]. These fibers offer an ultrabroad spectral range with multiple transmission bands as compared to other PCFs. In the preceding years, Kagome fiber with negative curvature was developed and was found to exhibit lower attenuation as compared to the regular ones.

## 6.4 Kagome fiber based nonlinear compression

Most of the pulse-compression experiments demonstrated so far in Kagome fibers used input pulses of sub-ps duration [27, 86, 87, 88, 89]. Consequently, due to the high peak power, the throughput pulse energy of those experiments was limited to few hundreds of micro-joule energy in the presence of air [78]. Recently, self-compression of 80-fs pulses down to the single-cycle regime in these fibers has been demonstrated
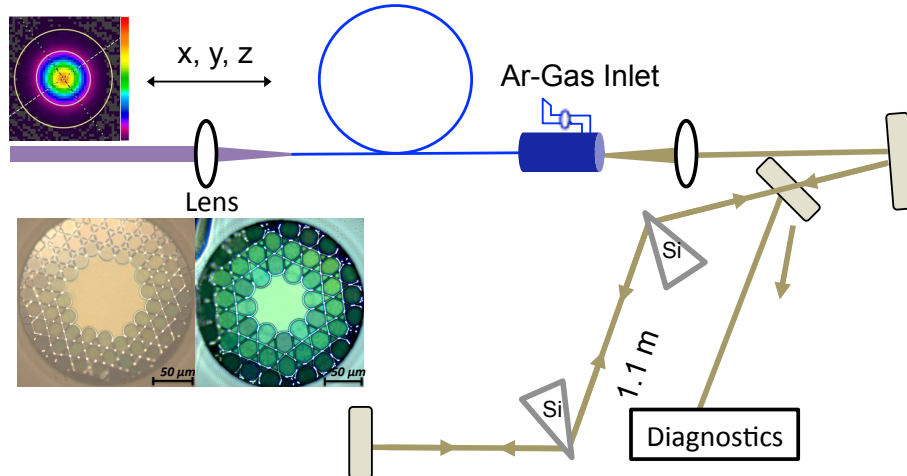
Figure 6.3: Experimental setup of the nonlinear pulse compression scheme using Kagome fiber. The output end of the fiber is placed in the gas chamber.

[89]. However, transferring such a compression technique to start with energetic ps-longer pulses is still a pressing challenge. This is particularly true in the case of 2 $\mu$m laser systems for which fs-pulse generation is still under development. In this section, the results obtained with a two-stage compression of ps-long pulses from Ho:YLF amplifier are presented. With a two stage compression scheme, we generated few-cycle pulses whose results are summarized below.

## 6.5    Compression stage I

### 6.5.1    Experiment

As a recall, the laser system used here is presented in Chapter 5 with etalon based gain shaping. A frequency selective linear filter, etalon of thickness 250 $\mu$m and reflectivity of 3.3 % was placed in the regen cavity to counteract the effect of gain narrowing in the amplifier. This technique enhances the effective gain bandwidth thereby broadening the spectrum from 2.9 nm to 5.4 nm [90]. The RA output was subsequently amplified in a single-pass booster amplifier (SPA) and the pulses were then compressed using a second identical CVBG. The net output of the amplifier (RA + SPA) with a total pump power of 26 W pump power was 2.2 mJ and 2.4 ps pulse duration. The experimental setup of the nonlinear pulse compression is shown in figure 6.3. The linearly polarized output of the CPA system was operated at lower pump power, to emit pulses of 1 mJ and 1.8-ps duration. These pulses were
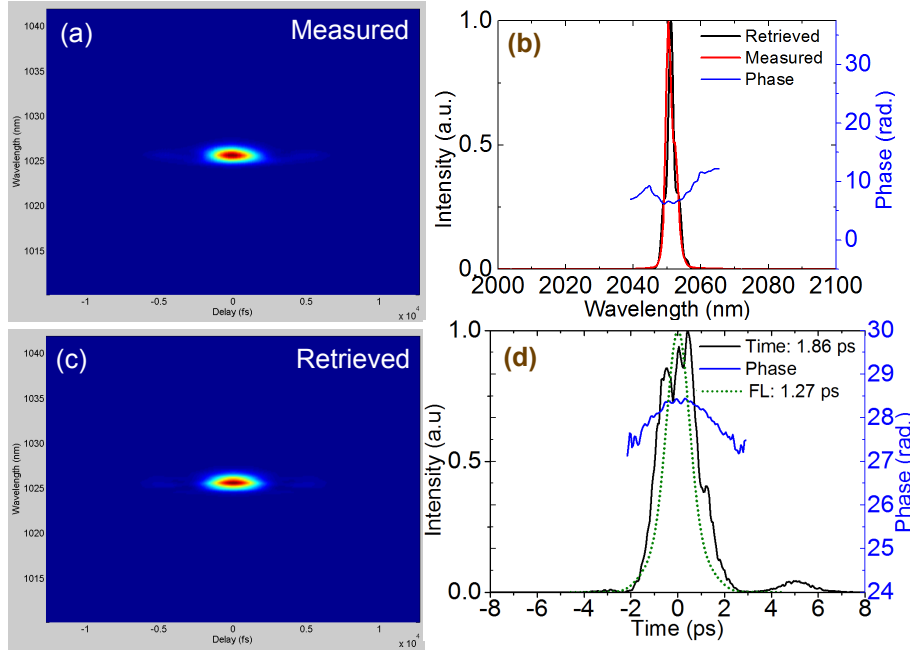
Figure 6.4: (a)-(d) FROG results of the input pulse used in the Kagome experiment. (a) and (c) Measured and retrieved FROG trace respectively, (b) measured (red) and retrieved spectrum (black) with the spectral phase (blue) and (d) retrieved intensity profile (black) with the temporal phase (blue)

coupled through a focusing lens into the Kagome fiber. Before proceeding with the experiments, we initially characterized the input pulses using a second-harmonic generation - frequency resolved optical gating (SHG-FROG) setup employing a 200-$\mu$m thick BBO crystal. Figure 6.4 (a) and (b) show the corresponding measured and reconstructed FROG traces with a reconstruction error of 1.0 %. Figure 6.4 (c) shows the retrieved (black) spectrum ($\sim$40 nm FWHM) and its spectral phase (blue) together with the independently measured spectrum (red), that matches well. Finally, figure 6.4 (d) shows the retrieved temporal intensity profile (solid black line) and the FL intensity profile (dotted red line) calculated from the independently measured spectrum. On the right-hand axis, the smooth and nonlinear temporal phase profile is shown (blue curve) suggesting that the input pulse was not completely compressed and there exist a small amount of residual chirp on the pulse. To investigate the transmission performance of the fiber, different coupling configurations were recorded. The beam diameter before the focusing lens was $\sim$3 mm and three different lenses of focal length f = 50, 60 and 75 mm have been tested to optimize mode matching and maximize the transmission efficiency in the fiber. The input end of the fiber was mounted on a metal V-groove. To adjust the input coupling energy, a TFP and a HWP were used as a variable attenuator 6.3.

## 6.5.2   Results and discussions

We used two different types of IC-guided Kagome HC-PCF fibers with 7-cell and 19-cell core based on a hypocycloid-core-contour designed for 2 $\mu$m wavelength operation. These fiber were fabricated using the stack and draw technique and were developed at University of Limoges in France in the group of Fetah Benabid. This new type of HC-PCF fiber offers relatively large core and low propagation losses. The physical and optical properties of both fibers are summarized in figure 6.5. The 19-cell fiber exhibits a hypocycloid core-contour of an inner core diameter of 82 $\mu$m corresponding to a mode-field diameter (MFD) of 58 $\mu$m. The 7-cell fiber has an inner core diameter of 63 $\mu$m corresponding to an MFD of 44 $\mu$m. The outer diameters of the 19-cell and 7-cell fibers are 330 $\mu$m and 350 $\mu$m, respectively, whose numerical apertures (NA) are estimated to be 0.014 and 0.018, respectively. Figure 6.5(a) shows the GVD as a function of wavelength, simulated using a finite-element method for both 7-cell and 19-cell fiber under three different conditions; in air and in Ar gas with pressure of 3 bar and 5 bar. Figure 6.5(b) shows the measured transmission loss along the extremely broad spectral range of 400 - 2400 nm exhibiting loss of 200 dB/km at 2050 nm. The unique transmission loss and bandwidth in addition to the possibility of easily changing the gas as a nonlinear medium in the fiber to control the nonlinear coefficient make it an ideal choice for exploring high-energy ultrashort pulses. This broad transmission bandwidth of Kagome fiber makes it unique among most of the known fibers. The calculated GVD for both 7-cell and 19-cell fiber at the operating wavelength of 2050 nm is low and anomalous with values of -2200 fs$^2$/m and -1200 fs$^2$/m, respectively. The experiments are performed both in the presence of air and Ar-gas pressure of 3 and 5 bar in 19-cell and 7-cell fiber.

Most of the experiments published previously have demonstrated self-compression in these fibers in FR, which occurs due to an interplay between the SPM and GVD. The SPM effect can be accounted for using the non-linear length of the fiber; $L_{NL} = 1/\gamma P_0$, where $\gamma = 2\pi n_2/\lambda A_{eff}$ is the nonlinear parameter, $n_2$ is the nonlinear refractive index coefficient, $\lambda$ is the wavelength, while GVD effect is accounted by the linear/dispersion length of the fiber given by $L_D = T_0^2/\beta_2$, where $T_0$ is input pulse duration and $\beta_2$ is the negative GVD introduced in the fiber. Hence, we see that the dispersion length, which is proportional to the square of the input pulse duration, can be very long for ps-pulses as compared to femtosecond pulses. Moreover, due to the low dispersion of these fibers (typically 1 ps/nm/km), ps-pulses exhibits hundreds
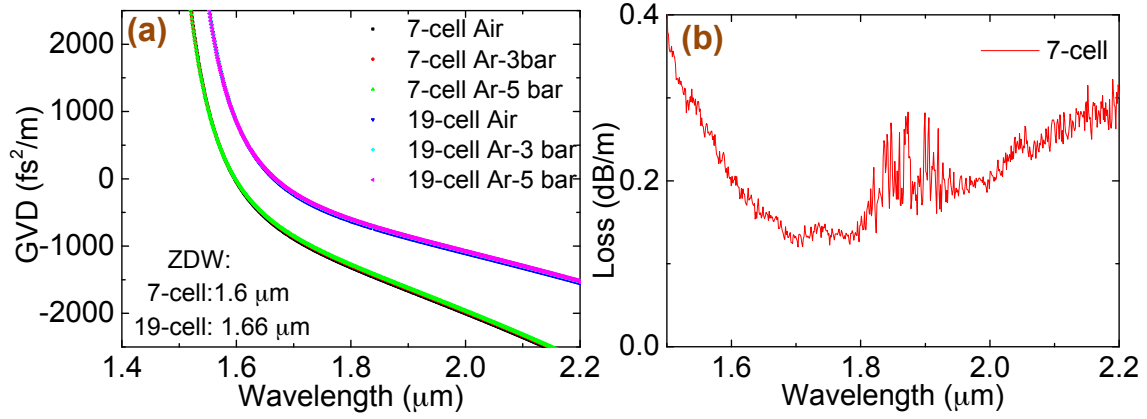
Figure 6.5: (a) Calculated GVD of the 7-cell and 19-cell fibers; (b) measured transmission loss versus wavelength of the 7-cell.

of km long dispersion length in these fibers, making self-compression impractical. Hence pulse compression with these fibers for ps-long pulses can be realized in two steps: spectral broadening in the fiber as the first step and external compression to compensate for the chirp acquired as the second step. It is also to be noted that due to long dispersion length, soliton order $N > 100$ where $N$ is defined as $N = \sqrt{L_D/L_{NL}}$. This satisfies the condition of MI making these experiments very prone towards to any kind of fluctuations.

**19-cell Kagome fibers**

Figure 6.6 (a) presents the efficiency curve for output versus input energy in 19-cell fiber in the presence of air for a different focusing length of 50, 60 and 75 mm at the input. We see that the best coupling efficiency of 90 % was achieved using the focusing length of 50 mm. Therefore, all the experiments shown here are performed using focusing lens of focal length of 50 mm. It is noteworthy that the transmission efficiency was also checked over 24 hours with the same fiber configuration and no damage was observed. The output end of the fiber was capped in a high-pressure gas cell with a 5-mm-thick uncoated $CaF_2$ window, while the input end was left open to the ambient air. As the input pulse duration was in the ps-range, the output spectrum does not support very short pulse duration, hence GVD from the window was of very little significance and was neglected. The first set of experiments was performed with 3.5 m of 19-cell fiber in the presence of ambient air. The experiments mostly rely on the fact that nonlinearity in these fibers can be easily tuned over the species of the gas present and its pressure.
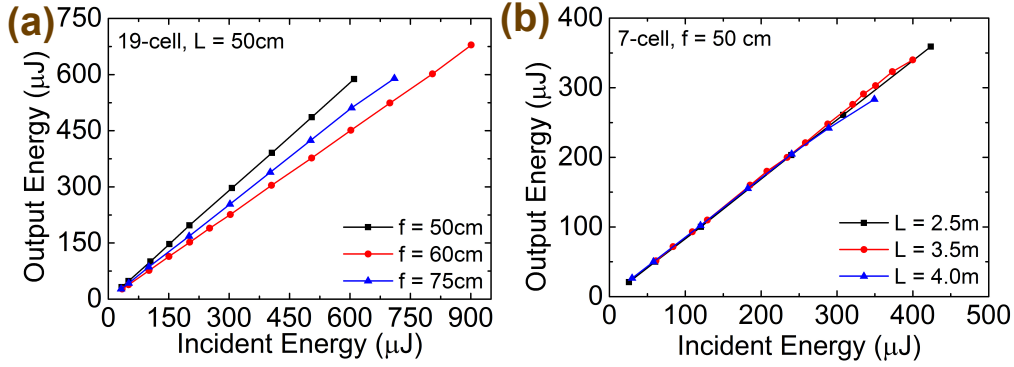
Figure 6.6: Input energy vs output energy (a) for different focusing lens of 50, 60, 75 mm in 19-cell fiber in the presence of air and (b) for different length of 2.5, 3.5, 4.0 m in 7-cell fiber in the presence of air

The spectrum evolution of the pulse after propagating through a 3.5-m-long 19-cell fiber (MFD = 58 $\mu$m) for different incident energies in the presence of ambient air is shown in the figure 6.7 (a). The fiber length was chosen to have enough nonlinearity in gas along the fiber but avoiding the break-up of the pulse due to the propagation of higher order solitons. Figure 6.7 (b) shows the measured autocorrelation traces (solid line) with the computed autocorrelation of the FL pulse corresponding to its respective spectrum (dashed lines). With the increase in incident energy from 45 $\mu$J to 707 $\mu$J, the spectral broadening scales linearly with energy. Without damaging the fiber, an incident energy as high as 707 $\mu$J, lead to increased foot-to-foot bandwidth of 77 nm corresponding to a FL duration of 260 fs (FWHM). Thus, it lead to a maximum peak intensity of 3.5 TW/cm$^2$ and 17 TW/cm$^2$ at the input and output respectively, and 5 times peak enhancement for the 19-cell fiber in the presence of air. It can be seen in figure 6.7 (b) that the shortest autocorrelation pulse duration was achieved with an input pulse energy of 707 $\mu$J resulting in an output pulse energy of 551 $\mu$J including the losses from the uncoated window of the gas cell.

In order to explore the effect of nonlinearity introduced by the gas in the fiber, the measurements were also performed in the presence of Ar at a pressure of 3 and 5 bar. Ar has high nonlinear refractive index coefficient $n_2 = 1.04 \times 10^{-19} cm^2/W$ at Ar pressure of 1 bar and ionization potential of 15.76 eV. This lead to an $n_2$ value of $3.12 \times 10^{-19}$ and $5.2 \times 10^{-19}$ cm$^2/W$ at 3 and 5 bar pressure, respectively [91]. (It is to be noted that the $n_2$ value here corresponds to 800 nm and 50 fs pulse). Thus, Ar leads to a sufficiently high nonlinearity to produce spectral broadening with the nonlinear length of 21 cm and 12 cm for 3 and 5 bar Ar-pressure respectively. ($L_{NL} = (\gamma P_p)^{-1}$), where $P_p$ is the peak power in the fiber core) and its ionization

Air



Figure 6.7: (a) Measured spectral evolution of the 19-cell fiber output in the presence of air for increasing incident energy; (b) measured auto-correlations (solid lines) obtained for the corresponding spectra in (a) after the prism compressor with a fixed GVD of -150000 fs$^2$ with the calculated autocorrelation of FL pulse (dashed lines)

potential limits the incident energy to $\sim$300 $\mu$J. This is due to the fact that the type of gas used here leads to photo-ionization and subsequent plasma absorption. Figure 6.8 (a) shows the broadened spectrum obtained with Ar-filled fiber, while the input side was left open to the ambient air, In the case of Ar pressure of 3 bar with incident energy of 226 $\mu$J, a maximum broadening with foot-to-foot bandwidth of 60 nm, which corresponds to the FL duration of 350 fs, was obtained. However, the measured pulse duration was 480 fs. Similarly, the experiments were also repeated with 5 bar of Ar up to the incident energy of 238 $\mu$J shown in figure 6.9. The maximum bandwidth achieved in this case was 68 nm leading to FL pulse duration of 280 fs and measured pulse duration of 350 fs. The increase in bandwidth with high pressure is due to the higher nonlinearity present in the fiber. Thus at the energy level of $\sim$240 $\mu$J and 5 bar of Ar, the spectral broadening factor increased by a factor of $\sim$2 with respect to air.

The spectrally broadened pulses were compressed using an external prism-compressor whose apex separation was 1.1 m and a prism insertion length of 10 mm. The distance was kept fixed throughout the experiments, which introduced a fixed negative second-order dispersion of $\sim$150000 fs$^2$ and was optimized for the maximum broadened spectrum of $\sim$86 nm, as will be further seen below in the 7-cell experiments. Uncoated silicon Brewster-cut prisms of height 1-inch and an apex angle of 73.84$^{\circ}$ were used as the compressor. Figure 6.8 (b) shows the measured autocorrelation trace with different incident energy corresponding to those spectrum
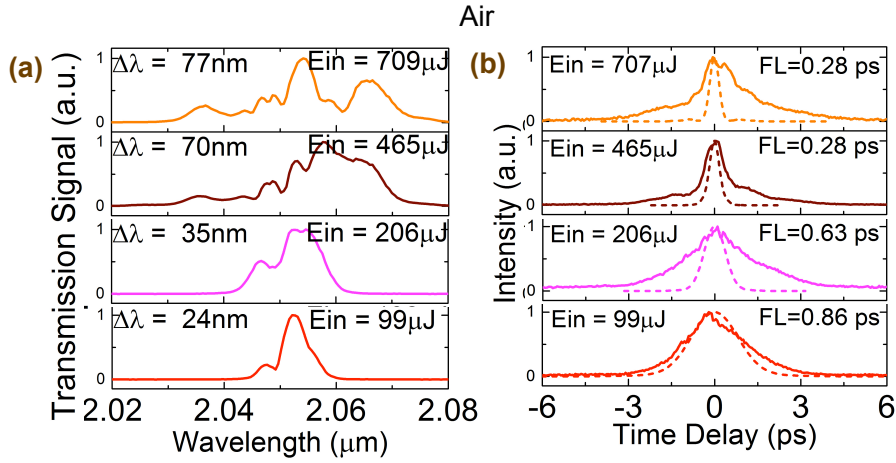
Figure 6.8: (a) Measured spectral evolution of the 19-cell fiber output filled with Ar gas pressure of 3 bar for increasing incident energy; (b) measured auto-correlations (solid lines) obtained for the corresponding spectra in (a) after the prism compressor with a fixed GVD of -150000 fs$^2$ with the calculated autocorrelation of FL pulse (dashed lines)



Figure 6.9: (a) Measured spectral evolution of the 19-cell fiber with an Ar gas pressure of 5 bar; (b) measured auto-correlations (solid lines) obtained for the corresponding spectra in (a) after the prism-compressor with a fixed GVD of -150000 fs$^2$ with the calculated autocorrelation of FL pulse (dashed lines)
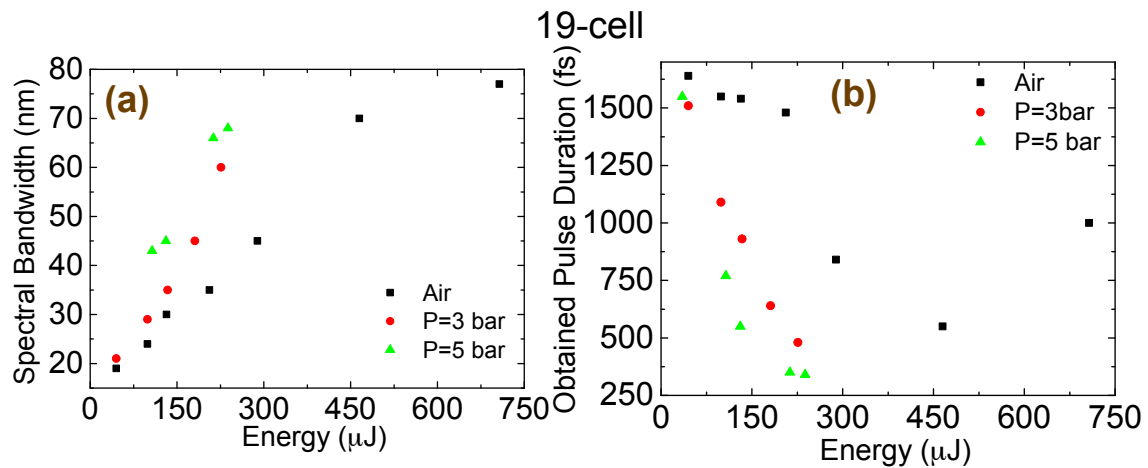
Figure 6.10: (a) Measured spectral broadening with increasing incident energy in 19-cell fiber of 3.5-m length in the presence of air and Ar pressure of 3 and 5 bar; (b) measured pulse duration with increasing incident energy assuming $sech^2$ shape

shown in (a) in 19-cell fiber in the presence of Ar-pressure of 3 bar after the prism compressor with the fixed distance of 1.1 m. Figure 6.10 (a) summarizes the broadening obtained at different incident energy in 19-cell fiber in the presence of air, and Ar pressure of 3 bar and 5 bar. Figure 6.10 (b) summarizes the measured pulse duration for the corresponding energy and gas condition after the prism compressor assuming sech²-shape.

## 7-cell Kagome fibers

To explore the effect of fiber core diameter on the nonlinear spectral broadening in these fibers, similarly, with the same experimental conditions, the above experiments were repeated with 7-cell fiber (MFD = 44 $\mu$m) of length 3 m with slightly smaller core diameter and similar experimental conditions as that for the 19-cell fiber in the presence of air and Ar pressures of 3 and 5 bar. The spectral and temporal evolution obtained is summarized in figure 6.11 and figure 6.12. For an Ar-gas pressure of 3 bar, enhanced broadening to 68 nm was obtained with an incident energy of 227 $\mu$J. This corresponds to a FL duration of 320 fs, while the compressed pulses are not completely compressed to FL duration as seen in figure 6.11 (b). When the experiments were repeated with 5 bar of Ar, the maximum broadening obtained is 88 nm and this corresponds to the FL duration of 250 fs. It is worth noting here that the compressed temporal profile obtained in the case of 5 bar of Ar in the 7-cell fiber exhibits the least amount of energy going into the wings. With a transmission
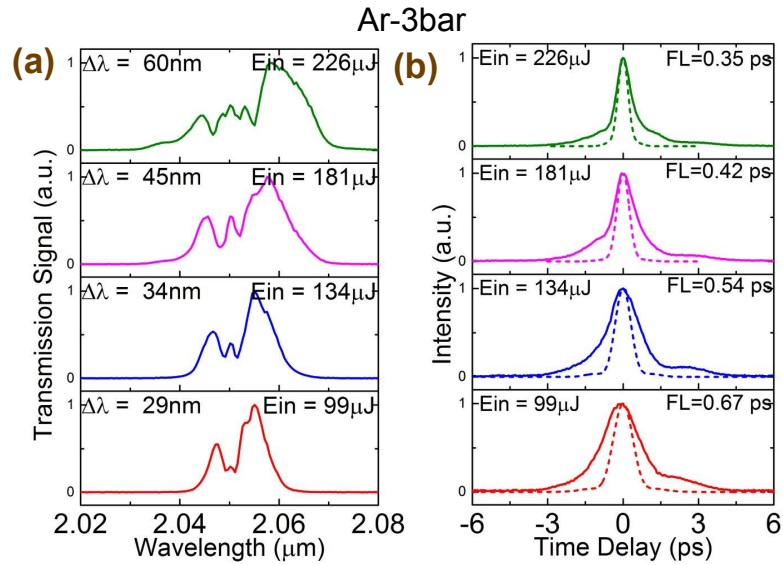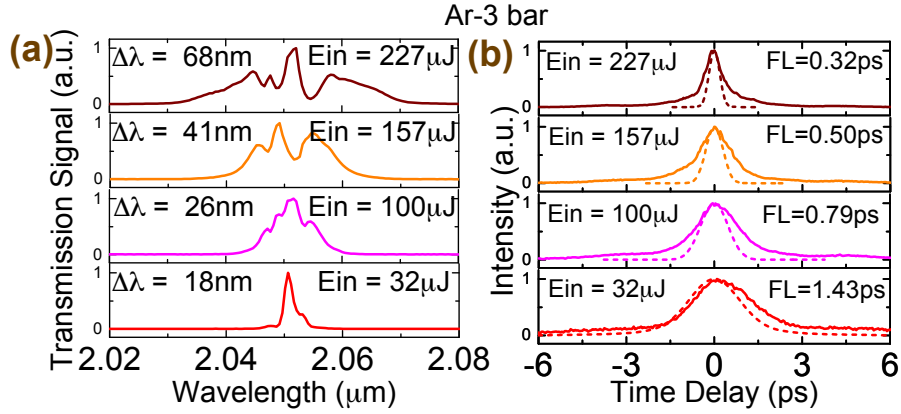
Figure 6.11: (a) Measured spectral evolution of the 7-cell fiber output filled with Ar gas at a pressure of 3 bar for increasing incident energy; (b) measured auto-correlations (solid lines) obtained for corresponding spectra shown in (a) after the prism compressor with a fixed GVD of -150000 fs$^2$ and the calculated autocorrelation FL pulse (dashed lines)

efficiency of 85 % from the fiber and a compressor efficiency of 75 %, the compressed energy obtained was 125 $\mu$J. There was a $\sim$10 % depolarization loss coming from the fiber, which explains the lower compression efficiency. By compensating for the depolarization, compression efficiency can be enhanced to $\sim$85 %.

Figure 6.13(a) summarizes the broadening obtained at different incident energy in 7-cell fiber in the presence of air, and Ar pressure of 3 bar and 5 bar. Figure 6.13 (b) summarizes the measured pulse duration after the prism compressor for the corresponding energy and gas conditions. It can be seen that with this fiber in the case of air and incident energy of 238 $\mu$J maximum bandwidth of only 31 nm and measured pulse duration of 1.03 ps was obtained. However, in the case of Ar pressure of 3 bar and 5 bar, maximum broadening of 68 nm and 88 nm was obtained and the measured pulse duration was 450 fs and 280 fs respectively. Thus, we see that the maximum broadening of 88 nm and shortest duration of 260 fs was achieved with 7-cell fiber and Ar pressure of 5 bar and incident energy of $\sim$240 $\mu$J. In the presence of air, spectral broadening of up to 77 nm and 31 nm was observed in 19-cell and 7-cell fibers at incident energies of 707 $\mu$J and 231 $\mu$J with FL durations of 280 fs and 770 fs, respectively. For an Ar gas pressure of 3 bar, a broadening of up to 60 nm and 68 nm was obtained in 19-cell and 7-cell fiber, which corresponds to a FL pulse duration of 350 fs and 320 fs, respectively, at an energy level of 227 $\mu$J. Finally, for a 5 bar Ar, broadening of up to 68 nm and 88 nm was achieved, which correspond to FL durations of 280 fs and 250 fs in 19-cell and 7-cell, respectively. Using the
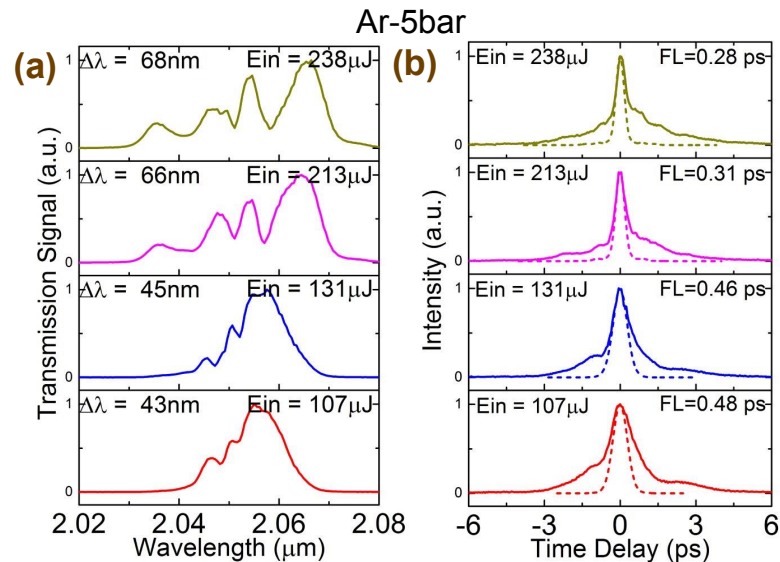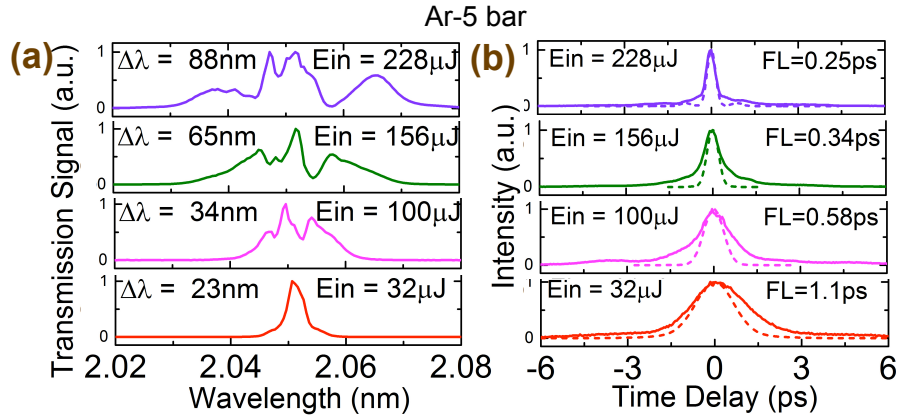
Figure 6.12: (a) Measured spectral evolution of the 7-cell fiber but with an Ar gas pressure of 5 bar; (b) measured auto-correlations (solid lines) obtained for corresponding spectra shown in (a) after the prism compressor with a fixed GVD of -150000 fs$^2$ and the calculated autocorrelation FL pulse (dashed lines)

prism compressor with a fixed apex separation optimized for the broadest spectrum of 88 nm, these pulses were compressed down to 300 fs and 285 fs for 19-cell and 7-cell fibers, respectively.

The output from the 7-cell fiber, with 5 bar of Ar and an incident energy of 227 $\mu$J, an output energy of 125 $\mu$J was achieved after the prism compressor. The pulses were characterized using SHG-FROG. Figure 6.14 (a) and (b) shows the corresponding measured and reconstructed FROG traces with a reconstruction error of 1.4 %. Figure 6.14(c) shows the retrieved (black) spectrum ($\sim$40 nm FWHM) and its spectral phase (blue) together with the independently measured spectrum (red), that matches well. Finally, figure 6.14 (d) shows the retrieved temporal intensity profile (solid black line) and the FL intensity profile (dotted red line) calculated from the independently measured spectrum. On the right-hand axis, the smooth and flat temporal phase profile is shown (blue curve) suggesting that only a small amount of chirp is remaining which can be compressed to 250 fs. However, the retrieved temporal profile still matches quite well with the calculated FL profile with approximately 30 % of the energy located in the wings.

### 6.5.3 Simulations

To understand the physical process involved in the experiments, we theoretically model the propagation dynamics of the presented experiments in gas filled Kagome fibers using numerical model based on the one-dimensional nonlinear Schrödinger
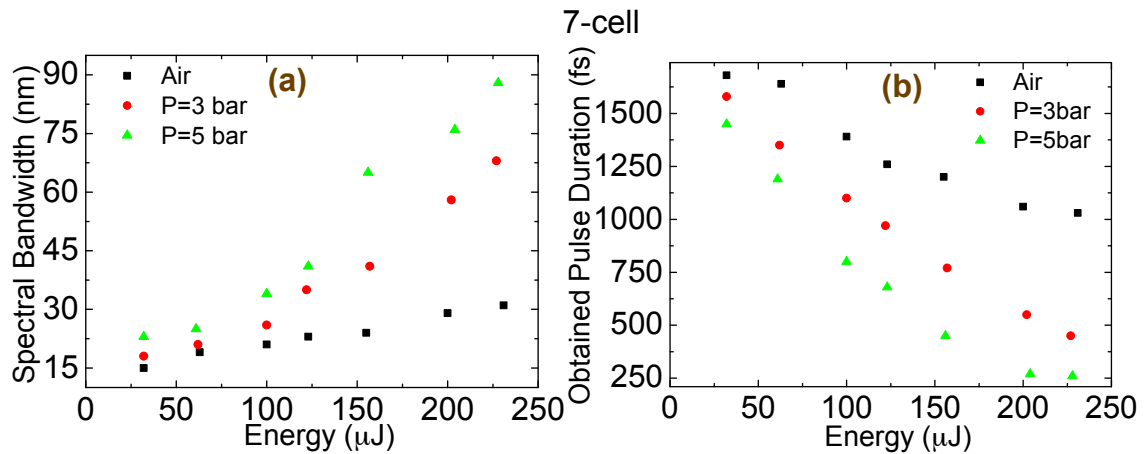
Figure 6.13: (a) Measured spectral broadening with increasing incident energy in 7-cell fiber of 3-m length in the presence of air and Ar pressure of 3 bar and 5 bar; (b) measured pulse duration with increasing incident energy assuming sech$^2$ shape
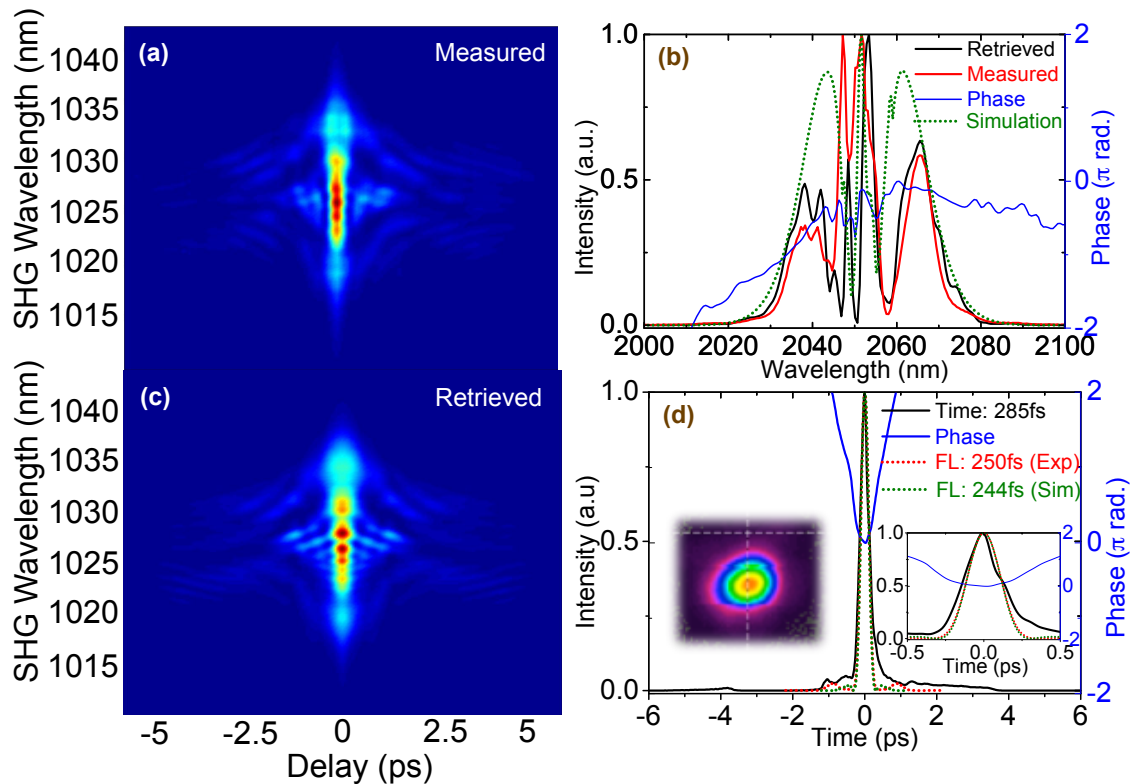


Figure 6.14: FROG results of the pulses from 7-cell Kagome fiber filled with 5 bar of Ar: (a) measured FROG trace (c) retrieved FROG trace, (b) measured (red) and retrieved (black) spectrum with the spectral phase (blue) (d) retrieved temporal intensity (black) and phase (blue) profiles.
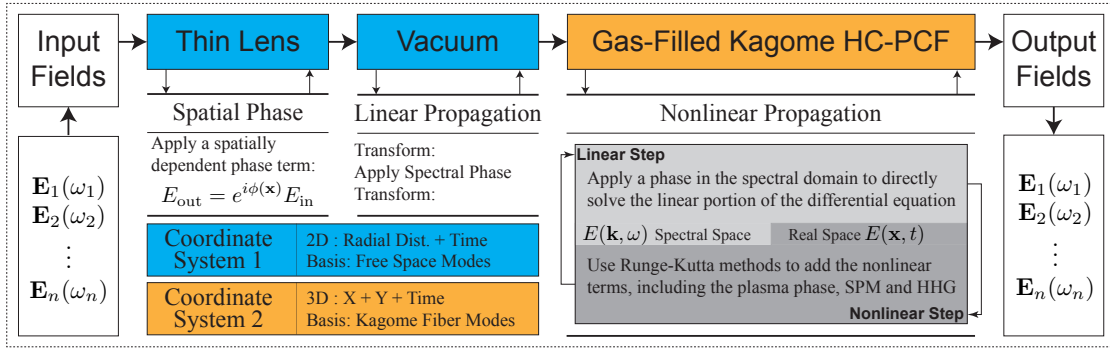
Figure 6.15: Schematic of the simulation model of the pulse propagation in the Kagome fiber (figure reproduced from from [7])

equation.

$$i\frac{\partial A}{\partial z} = \frac{\beta^2}{2}\frac{\partial^2 A}{\partial t^2} - \gamma|A|^2 A \tag{6.18}$$

where $A$ is the electric field envelope, $\gamma = 5.9 \times 10^{-8}$/m.W is the nonlinear parameter and $\beta_2 = -2345$ fs$^2$/m is the second-order dispersion of the gas-filled Kagome fiber including the geometric contribution of the 7-cell fiber. Apart from self-phase modulation, in general, propagation of high-intensity pulses in a fiber may involve various nonlinear processes like plasma formation and higher order Kerr effects. In the model, a static pressure has been assumed throughout the length of the fiber.

The simulation model was developed by Gregory J. Stein in Matlab and is based on the split-step Fourier technique. As an input, we used the transform limited pulse computed from the experimentally measured spectrum and is propagated along a 7-cell fiber of length 3 m. Figure 6.16 shows the temporal and spectral evolution of this input pulse with an energy of 135 $\mu$J, along the 7-cell fiber filled with Ar pressure of 1 bar. Since the combined dispersion of the fiber and the gas is very low, the temporal profile does not change dramatically, as the pulse propagates along the fiber, while its spectrum is significantly broadened. Since the dispersion is small, the output of the fiber is chirped, requiring external compression. The output spectrum overlays the FROG results shown in figure 6.14 (b) (green) which is in good agreement with the measured spectrum. The FL pulse duration of the corresponding spectrum was 244 fs, also an overlay in figure 6.14 (d), which matches quite well to that of the FL pulse obtained from the measured spectrum. Some of the parameters used in the simulation were quite different from the ones in the experiment. For

Figure 6.16: Simulation results obtained using the above model (a) temporal and (b) spectral evolution of the output pulse along the fiber length

example, the pulse energy used in the fiber was 180 $\mu$J, however this excludes the coupling loss, which could not be independently determined. Furthermore, though a measurement of 5 bar was made near one end of the fiber, the exact pressure along the fiber length (as the gas flows through it) is not very realistic to determine. Discrepancies of this nature are relatively standard for experiments such as this one [78], and the close agreement of the simulations with the experimental results lends credibility to these parameters.

## 6.6  Compression stage II

### 6.6.1  Simulations

After the modeling results were benchmarked with the verification of experimental results, the simulations were performed for the second stage Kagome fiber whose results are summarized below in figure 6.17. The simulation of the second stage was performed keeping the pressure same as in the first stage and the energy yielded in that stage. Several runs of simulation were performed looking for the optimum length for which the compressed pulse do not break up into multiple solitons in the fiber. The optimum value was obtained for 80 mm of fiber length which yielded broadened spectrum with Fourier-limited duration of $\sim$6 fs and 20 $\mu$J of energy. The simulation results suggest few-cycle pulse output in a second stage and led to the motivation of the second stage Kagome compression development.
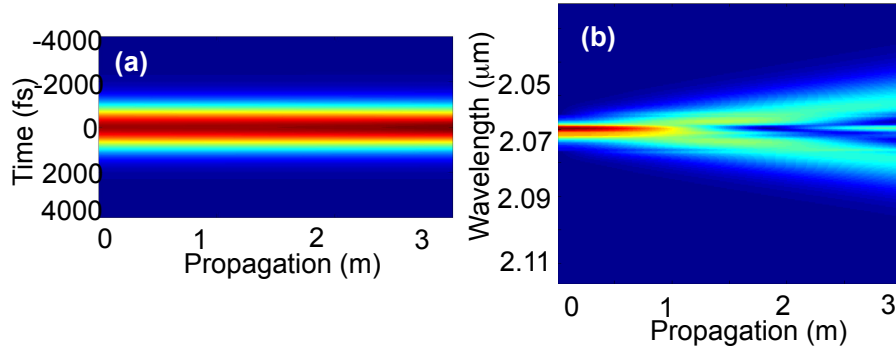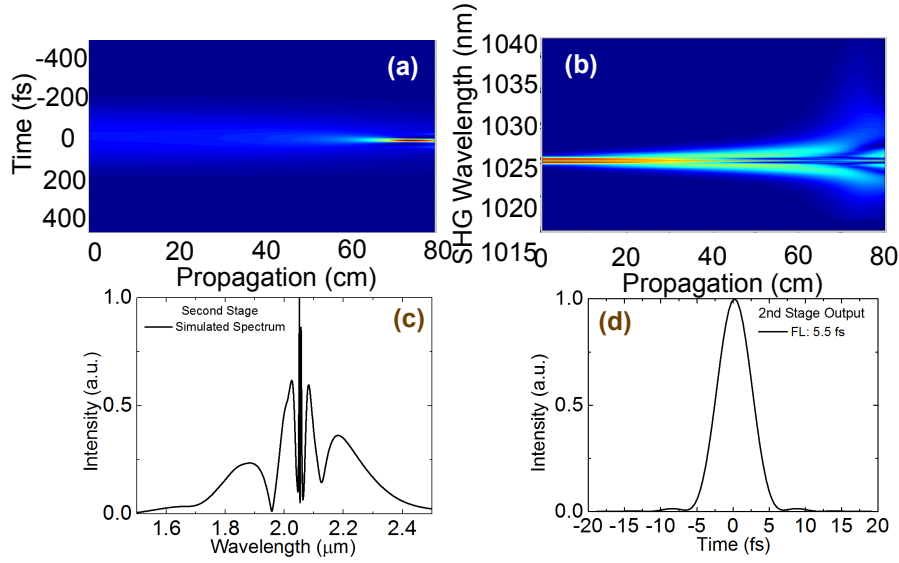
Figure 6.17: Simulation results (a) temporal and (b) spectral evolution of the output pulse along the fiber length

## 6.6.2 Experiment and results

The experimental setup for the two-stage Kagome compressor is shown in the figure 6.18. The compressed output from the first stage 7-cell Kagome fiber having a length of 3 m described in the previous section was launched into the similar fiber that in the first stage. The fiber exhibits hollow inner-core and outer diameters of 63 $\mu$m and 330 $\mu$m, respectively. The MFD of the fiber was 44 $\mu$m and the numerical aperture was 0.014. The experimental layout is shown in figure 6.18. The input energy in the first stage fiber was 140 $\mu$J, while the output energy was 123 $\mu$J. The retrieved pulse duration from FROG measurement of the first stage shown in figure 6.14 (d) (black) is 285 fs FWHM. The length of the 7-cell fiber used in the second-stage Kagome was 2 mts and the output pulse was characterized using the SHG-FROG and NIRQuest spectrometer.

In the second stage, the pulses further undergo SPM, which lead to spectral broadening up to ~370 nm bandwidth (foot-to-foot). The output spectrum is shown in figure 6.19 (blue). The inset shows the spectra on a log-scale. Also, due to the ultrabroad spectrum, the positive chirp, that needs to be compensated, is quite small leading to pulse self-compression in the Kagome fiber. The pulse duration measured at the output of the fiber was ~150 fs. However, the GVD of the fiber was not enough to fully compensate for the chirp. Therefore, we used a thin fused silica window of 2 mm and a sapphire window of 5 mm. We optimized the required
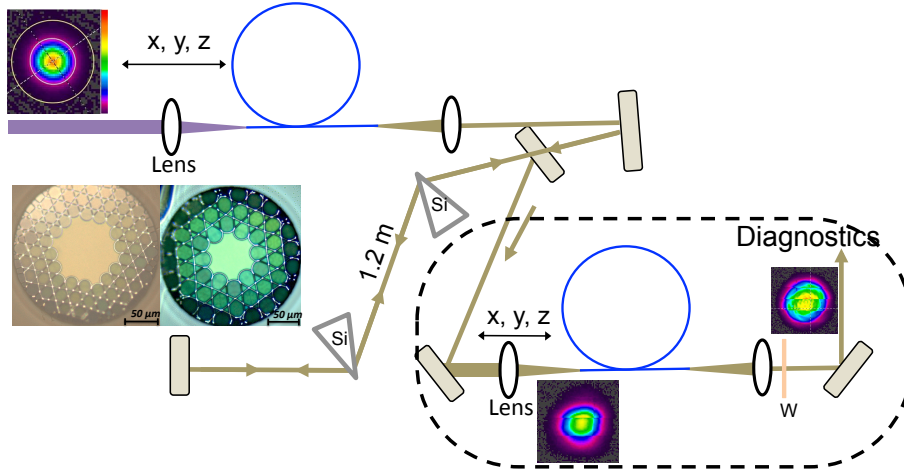
Figure 6.18: Experiment layout of the two stage compressor

amount of dispersion from the windows by performing several scans of SHG-FROG on the output pulse by increasing the window's thickness in a step of 1 mm. Figure 6.20 (a)-(e) shows SHG-FROG results obtained after optimizing the extra-dispersion required to compensate for the residual chirp, remaining after pulse self-compression. The measured FROG trace shown on the full-time scale in figure 6.20 (a) exhibits a spectrally broadband, ultrashort compressed feature riding on top of a several-ps-long component. For numerical reasons emerging from the high complexity of the FROG trace data, in a preliminary reconstruction we filtered out the compressed part using a super-Gaussian filter in time. The resulting filtered FROG trace shown in the figure 6.20 (b) comprises 28 % of the energy contained in the full pulse. From the reconstruction of this filtered FROG trace, as depicted in figure 6.20 (c)-(e), we obtained a 48-fs FWHM duration of the compressed component, which contains 67 % of the energy (within -100 fs to 300 fs). Thus, overall the compressed part contains 28 % × 67 % = 19 % of the total output pulse energy of 60 $\mu$J, i.e. we generated 11-$\mu$J 48-fs FWHM pulses centered at 2050 nm.

## 6.7    Conclusions

In summary, we demonstrated both experimentally and numerically two-stage compression of 2-$\mu$m, 3.4-ps long pulses from Ho:YLF amplifier down to a 7-cycle 48-fs FWHM duration with 11 $\mu$J energy. This strong-field 7-cycle MIR source will have intriguing applications in strong-field attoscience experiments. Nonlinear propagation dynamics of ps-pulses in Kagome-type HC-PCF fibers was studied in two different
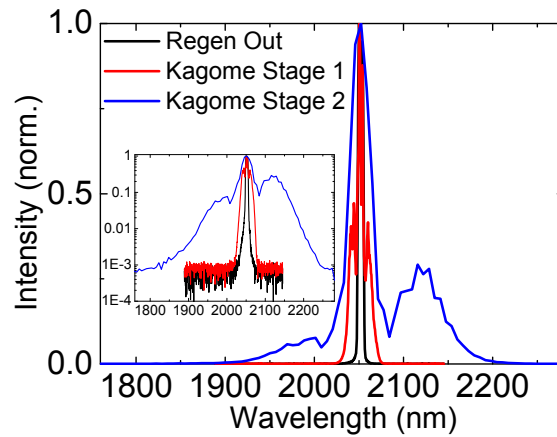
Figure 6.19: Input and output spectra of the two-stage Kagome fiber compressor in the presence of air. The inset shows the spectra on a logarithmic scale.
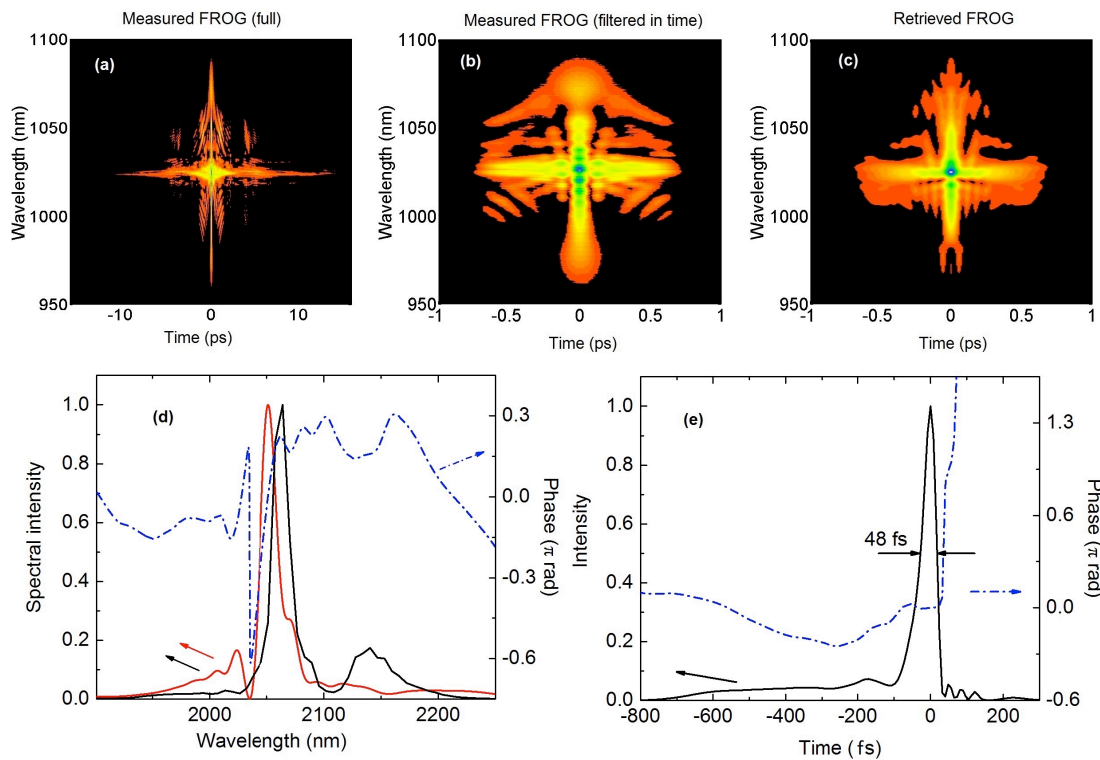


Figure 6.20: SHG-FROG results of the self-compressed pulses from the second-stage 7-cell Kagome fiber filled with air: (a) Measured FROG trace shown on the full-time scale, (b) measured FROG trace after filtering out the compressed part using a super-Gaussian filter in time, (c) reconstructed FROG trace retrieved from the filtered trace shown in panel (b); (d) measured (black) and retrieved (red) spectra with the spectral phase (blue), (e) retrieved temporal intensity profile (black) and the temporal phase (blue).

geometries, 7-cell, and 19-cell designs. In the presence of air, maximum spectral broadening of 77 nm is observed in 19-cell fibers at incident energies of 707 $\mu$J with FL duration of 280 fs. The experiments were also repeated in Ar-filled fibers at pressure of 3 and 5 bar for both designs. The best compression was achieved with a 7-cell fiber at 227 $\mu$J incident energy and Ar gas pressure of 5 bar with maximum broadening of 88 nm which corresponds to a FL-duration of 250 fs. Finally, using external prism-pair, 1.8-ps pulses was compressed to 285 fs with FL duration of 250 fs and more than 70 % of the energy in the central peak. The total throughput energy in these fibers was 500 $\mu$J and 707 $\mu$J for 7-cell and 19-cell fiber respectively, with high a transmission efficiency of 90 %. Though the best compression of 770 fs and 290 fs was achieved at 280 $\mu$J and 560 $\mu$J for 7-cell and 19-cell fiber respectively.

Hence, depending on the application, broadening in both 7-cell and 19-cell fiber can be useful. For experiments, that need shorter pulse duration, 7-cell fiber is optimum, whereas, for experiments that need higher energy, 19-cell is a better choice. The numerical results suggest that in the ps-regime, the spectral broadening is mostly dominated by SPM and no higher order effects are significant. This is for the first time (to the best of our knowledge) compression of 2-$\mu$m ps-laser pulses. We further studied numerically the propagation of ps-pulses in these fibers and the model matched weel to the experimental behavior.

# Part III

# Signal Generation for MIR OPA

# MIR Supercontinuum Generation

## 7.1 Introduction

Supercontinuum (SC) generation is a process that ocurs when a narrowband optical pulse with a certain peak intensity, is incident on a nonlinear medium it undergoes extreme spectral broadening due to self-phase modulation (SPM), thereby generating an ultrabroad spectrum at the output. The schematic of the process is shown in the figure 7.1. Ever since its first demonstration by Alfano and Shapiro in 1970 in bulk medium [92], SC has found its application in the diverse fields, and even after four decades from its discovery, it is still a hot topic today due to its high spatial coherence, high brightness, and broad bandwidth. The underlying mechanism of SC generation depends largely on whether the pump wavelength lies in normal or anomalous dispersion regime, and can include several effects like SPM, self-focussing, cross-phase modulation (XPW), Raman scattering and four-wave mixing (FWM). The ultrabroad spectrum of SC phenomena particularly attracted people from telecommunication community for developing wavelength division multiplexing systems. With the advent of discovery of photonic crystal fibers, the study of SC became more intense and a breakthrough occurred in 2000 when Ranka et al. demonstrated an octave wide spanning spectrum from a Ti:Sapp laser [93].
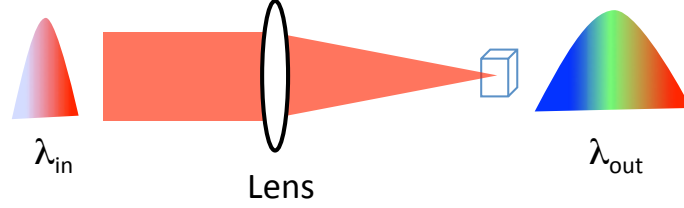
Figure 7.1: Experimental layout for a SC generation process

## 7.2   Theory

Despite the experimental demonstration of SC generation in the 1970s, the process was not well understood in the many preceeding years. This was mainly because SC process involves different complex behavior for different experimental conditions. In order to understand the physical picture behind SC process, one needs to solve the following generalized propagation equation and study its pulse evolution. The detailed description can be found in Ref. [94, 95].

$$
\frac{\partial A(z,t)}{\partial z} + \frac{\alpha}{2} A(z,t) - \sum_{k \geq 2} \frac{i^{k+1}}{k!} \beta_k \frac{\partial^k A(z,t)}{\partial t^k} = i\gamma \left( 1 + i\tau_{shock} \frac{\partial}{\partial t} \right) \times
$$
$$
\left[ A(z,t) \left( \int_{-\infty}^{+\infty} R(t')|A(z,t-t')^2|dt' + i\Gamma_R \right) (z,t) \right]
$$
(7.1)

where $A(z,t)$ is the envelope electric field, $\beta_k$ is the dispersion coefficients at center frequency $\omega_0$, $\gamma$ is the nonlinear coefficient that depends on nonlinear refractive index $n_2$ and fiber core effective area $A_{eff}$. The time derivative term includes the self-steepening and optical shock effects, $\tau_{shock} = 1/\omega_0$ is the time scale of the shock effect. Hence by tailoring the fiber core, the amount of dispersion can be manipulated for their nonlinear response and can be included in the shock term to the first-order correction. $R(t) = (1 - f_R)\delta(t) + f_R h_R(t)$ includes the Raman response (both instantaneous and delayed response), and the input field envelope $A(z = 0, t) = \sqrt{P_0} sech(t/T_0)$ is assumed to be chirp-free, where $P_0$ is the peak power and $T_0$ is the pulse duration of the input pulse. The model includes spontaneous Raman noise term $\Gamma_R$ and the quantum-limited noise of the input pulse (one photon per mode background).

A simplified version of the Schrödinger equation 7.1 can be derived as [82]:

$$\frac{\partial A}{\partial z} + \frac{\alpha}{2}A = i\sum_{m=1}^{\infty} \frac{i^m \beta_m}{m!} \frac{\partial^m A}{\partial t^m} + i\gamma\left(1 + \frac{i}{\omega_0}\frac{\partial}{\partial t}\right) \times \left(A(z,t)\int_0^{\infty} R(t')|A(z,t-t')|^2 dt'\right)$$

$$(7.2)$$

For most of the application, up to third-order dispersion terms are enough, and the above equation can be re-written into new normalized variables $U, \xi, \tau$ as:

$$i\frac{\partial U}{\partial \xi} - \frac{\delta_2}{2}\frac{\partial^2 U}{\partial \tau^2} + N^2|U|^2 U = i\delta_3\frac{\partial^3 U}{\partial \tau^3} + iN^2\left(1 + is\frac{\partial}{\partial \tau}\right) \tag{7.3}$$

$$\times \left(U(\xi,\tau)\int_0^{\infty} R(\tau')|U(\xi,\tau-\tau')|^2 d\tau'\right) \tag{7.4}$$

where the normalization factors are defined as:

$$U = \frac{A}{\sqrt{P_0}}, \tag{7.5}$$

$$\xi = \frac{z}{L_D}, \tag{7.6}$$

$$\tau = \frac{T}{T_0} \tag{7.7}$$

In the above equation, $\delta_2 = sgn(\beta_2) = \pm 1$ and $N$ is the soliton number defined as $N = T_0\sqrt{\gamma P_0/\beta_2}$, $\beta_2$ is the second of dispersion (GVD), $P_0$ is the peak power and $T_0$ is the pulse duration of the incident pulse, $\alpha$ is the fiber loss. $s$ is the self-steepening factor given by $s = (\omega_0 T_0)^{-1} << 1$ and can be neglected for most cases (for more than few fs pulses), $\delta_3$ is the third-order dispersion (TOD) parameter given by $\delta_3 = \beta_3/(6|\beta_2|T_0)$ and usually leads to a break-up of fundamental soliton into multiple higher order solitons, giving rise to new process called as soliton fission. In this process, part of the soliton energy is transferred to a *'dispersive wave'* at a specific frequency satisfying the phase-matching condition (usually on the blue side of the spectrum). The frequency of the dispersive waves is generally given by $\omega_d = \omega_0 - 3\beta_2/\beta_3$.

## 7.3 Propagation dynamics

Due to the vast application of SC, the complete understanding of the underlying process is of immense importance. However, the rate at which there has been

the experimental development of SC generation, the theoretical developmemt did not exist at same rate. The main reason for this has been the various complex processes involved in SC generation under various experimental conditions. Due to the experiments performed with variety of different parameters like fiber types, pump pulse duration, length of the medium and pulse energies, it has never been easy to isolate the individual contributions arising from various nonlinear processes like SPM, XPM, FWM, modulation instability (MI), soliton fission, dispersive wave generation and Raman Scattering. Therefore, it was often found that the physics behind the experiment was wrongly interpreted. Over time, this has led to large misunderstanding in the community and even till date, it appears that there does not seem to exist a clear path to interpret various underlying process in SC generation. A very good review was presented by Dudley and co-workers who discusses various important published results and tried to isolate various nonlinear process based on the experimental conditions [71].

## 7.3.1 SC generation in fibers

The processes involved in SC generation varies largely depending on whether the input wavelength is to the right (anomalous) or left (normal) of the zero dispersion wavelength (ZDW) of the fibers and whether the duration of the input pulse is in fs-regime or ps-regime. In the case of input pulse being short or in fs-range and the wavelength is in normal dispersion regime, SC is dominated by SPM, while in anomalous regime, the SC is governed by soliton dynamics. However, when the input pulses are long or in ps-range, then in normal dispersion regime FWM and stimulated Raman scattering (SRS) dominate, while in the anomalous regime, the noise of the input pulse can give rise to higher-order soliton formation through a phenomenon called as modulation instability (MI), which results in pulse splitting temporally and thus distributing the generated frequencies to many shorter sub-pulses. In MI, the noise of the long input pulse can undergo parametric gain, giving rise to higher order soliton formation. These higher order solitons are a particular solutions of NLS equation and they represent N-fundamental solitons which propagate in a complex manner. They undergo spectral & temporal compression and pulse splitting, and after propagating through a characteristic distance of soliton period, the pulse recovers to its original state [71]. However, it was shown [96] that despite the complex evolution of higher order solitons, in anomalous GVD regime of fibers, the initial dynamics involves relatively simple SPM-induced spectral broadening

and temporal compression due to anomalous GVD. In the presence of higher order dispersion, higher-order solitons become more pronounced, leading to a temporal break-up of the pulse into its constituent fundamental solitons and the process is known as soliton fission. The extensive studies on the amplitudes and widths of these constituent solitons have been studied by [97] and shown that the sum of energies of the constituent solitons is equal to that of higher order solitons. This suggests that there exist intrinsic instabilities of these solitons due to the presence of fluctuations on the input pulse. Other studies have shown that the instabilities can also arise due to the presence of self-steepening, Raman effect, and multi-photon absorption. The fact that nonlinear pulse propagation depends on the input power, the unavoidable fluctuations on the input pulses can lead to jitter in both spectral and temporal evolution. This leads to a difference in the actual spectrum and the measured spectrum that is the ensemble average of each constituent fundamental solitons undergone different self-frequency shift. These studies suggest that process of soliton fission is highly sensitive to the input pulse noise.

## 7.3.2 SC generation in bulk medium

SC generation in a bulk medium is much more complex than in fibers due to self-focusing effect playing a significant role. Beyond a critical power, self-focusing leads to a catastrophic collapse of the beam which leads to steepening of the backside of the pulse causing very steep negative intensity slope. This leads to an explosive increase of peak intensity which enhances various nonlinear effects like SPM, self-steepening, space-time focusing, multi-photon absorption, avalanche ionization and plasma formation ([98, 99, 100]). A mathematical model explaining the underlying process of SC generation in the bulk medium was explained by Gaeta et al. who performed a three-dimensional analysis and theoretically proved that enhanced SPM due to self-steepening owing to space-time focusing and defocusing is the main cause of extreme spectral broadening in SC generation [101]. The collapse of the beam and material break-down is prevented by multi-photon absorption and plasma formation. Understanding the complete dynamics of SC in a bulk medium is very complex that involves intricate coupling between spatial and temporal effects.

### 7.3.3   Different regimes under which SC can be studied

Various numerical studies have shown that SC generation process can be explained broadly in three phases: (1) initial spectral broadening and temporal compression, (2) fission of the fundamental soliton into series of distinct constituent fundamental solitons and (3) continued propagation of these solitons which due to Raman soliton self-frequency shift causes continuous shift to the longer wavelength leading to generation of corresponding dispersive waves at shorter wavelength across ZDW point.

- **_Short pump pulse (fs) in anomalous GVD regime:_** In this case, the spectral broadening occurs due to soliton dynamics and can be understood in three phases. Since the pulse duration is short, $L_D$ and $L_{NL}$ are comparable and the soliton number $N \sim 1, (N = L_D/L_{NL})$. Thus the higher-order soliton does not play very significant role. In the first phase, pulse undergoes spectral broadening due to SPM and temporal compression due to opposite sign of chirp arising from the anomalous dispersion. In the second phase, due to perturbations arising from noise, high-order dispersion and SRS, the pulse break-up (*'soliton-fission'*) into series of $N$ number of distinct soliton components. As these individual solitons propagate in the fiber, due to higher-order dispersion, resonant energy transfer takes place across the ZDW, which gives rise to dispersive wave spectral components and is intrinsically narrow-band. Due to the narrow-band behavior of the dispersive wave, an abrupt edge is seen at the short wavelength in the SC spectra. Finally, in the third phase, as the solitons propagate further, it gives rise to Raman soliton which due to self-frequency shift results in the continuous shift of spectrum to the longer wavelength. Also, due to XPM, the Raman solitons and the dispersive waves can couple which generates additional frequency components thereby enhancing the overall bandwidth.

- **_Long pulse (ps) in anomalous GVD regime:_** In this case, since the pulse duration is long, $L_D >> L_{NL}$, hence the soliton number $N$ is large ($N >> 10$) and as the length of soliton fission process scales proportionally with the pulse duration ($L_{fiss} = L_D/N \propto \tau$), the soliton fission becomes less important and MI begins to dominate. MI is the generation of parametric side-bands due to FWM spontaneously arising from noise at frequencies not overlapping with

the broadened spectrum. This leads to the temporal break-up of the pulse into a large number of sub-pulses. As these sub-pulses propagate in the fiber, they undergo spectral broadening with the same mechanism as that of short duration i.e. each sub-pulse further undergoes soliton fission, dispersive wave generation, and self-frequency shift. However, if the pump wavelength is too far from ZDW, the energy transfer from the sub-pulse across ZDW responsible for dispersive wave generation may not be possible and thereby leading to reduced spectral broadening. It is also to be noted that depending on the fission length, there can exist a competition between MI gain and soliton fission. Furthermore, the coherence of SC is largely affected by the MI.

- ***Short pulse (fs) in normal GVD regime:*** In this regime, when the pump wavelength is well away from the ZDW, then simply SPM and the normal GVD contributes towards both spectral & temporal broadening and thus limiting the broadening, as the peak power reduces as the pulse propagate in the fiber. However, if the pump wavelength is close to ZDW, the spectral broadening leads to transfer of the spectral contents to the anomalous GVD regime thereby bringing soliton dynamics into the picture. Moreover, depending on the fiber and pump parameters, the energy transfer across ZDW can also occur from the contribution of parametric generation and the SRS.

- ***Long pulse (ps) in normal GVD regime:*** In this regime, SPM does not play a major role in spectral broadening but rather important contributions come from FWM and Raman scattering. If the pump wavelength is far from ZDW, then the parametric gain is not high and the spectral broadening is affected mainly by Raman effects. However, if the pump wavelength is close to ZDW, then the parametric gain is higher than the Raman gain leading to FWM process.

## 7.4 Applications

Ever since its discovery, SC has found its way in variety of applications in the field as diverse as spectroscopy, tomography and metrology. The metrological application has led to the development of optical clocks leading to 2005 Nobel Prize in physics to Hall and Hansch. Due to the extreme broadening effect of SC generation, the spectrum obtained can be used in many applications requiring a broadband source.
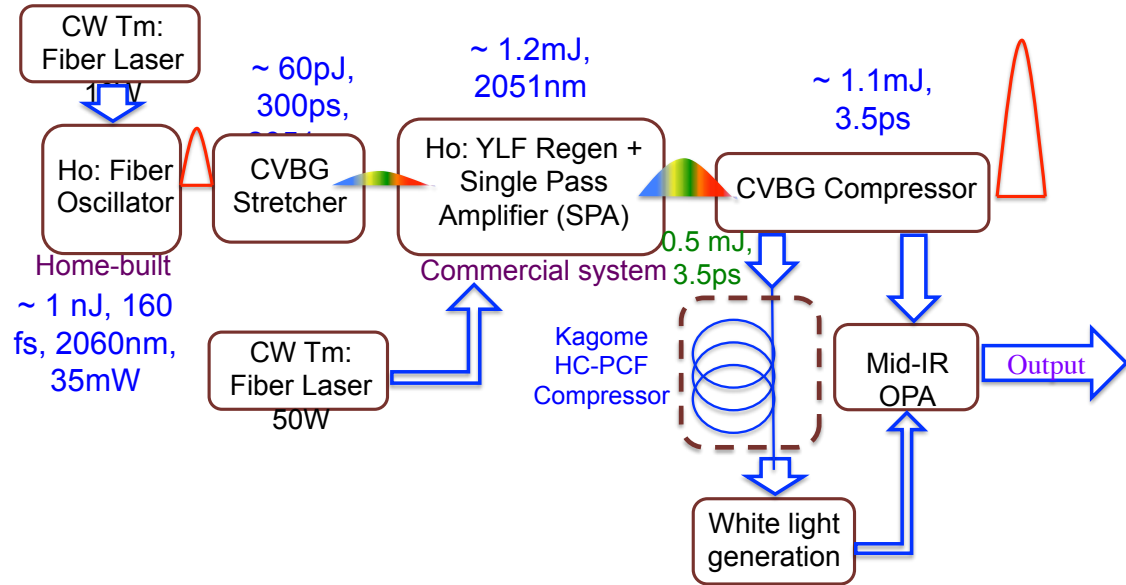
Figure 7.2: Schematic for the MIR OPA

There has been the demonstration of SC generation using input pulses ranging from 10s of fs to ns and even CW pulses. Such sources has also been found useful for applications like pump-probe spectroscopy, coherent Raman spectroscopy, near-field optical spectroscopy, and other forms of coherent nonlinear spectroscopy. They have been found very useful in medical applications like probing of several unknown species in nature. They are also widely used in anti-Stokes Raman scattering and optical coherence tomography (OCT). They are widely used as a seed source for an OPA which can amplify the entire or large part of the spectrum to several orders of magnitude. Nowadays, one can easily generate ultra-broadband SC using femtosecond pulses from an oscillator in a small core fiber which confines high peak intensities into a small core leading to SPM and hence the spectrum broadens. But the small core size of the fiber limits the average output power to few mW. One also needs to take care of the extent of spatial and temporal coherence. Depending on the application the choice of SC source is decided as some may need low-power broadband light and good coherence while some may require high-power broadband light with temporal coherence not being a stringent requirement [102].

## 7.5   Need for sub-ps pulse

Stability of SC white light is a key for it to be usable in numerous applications. As discussed in the earlier, spectral broadening is very sensitive to any kind of noise

on the pump pulse be it quantum noise or amplifier noise and they give rise to instabilities in the SC. Hence it is important to understand the noise behavior so that instabilities on the SC can be minimized. In anomalous GVD regime, as the input pulse propagates along the fiber, the noise gets significantly amplified as it sees MI gain and there is a competition between MI and soliton fission and the saying *'winner takes all'* becomes true. Depending on which process finally succeeds during propagation, the instability statistics differ. If soliton fission dominates, then the input pulse gets temporally compressed fast enough that the spectral content of SC gets overlapped with the frequencies of MI-gain bandwidth. Thus the noise background does not get enough time to amplify leading to coherent seeding of MI gain bandwidth which results in stable SC. However, if MI dominates, noise background gets amplified and the spectral broadening gets seeded by the noise which leads to spectral and temporal instabilities on each pulse leading to incoherent SC. Since the phenomena of MI is more likely to be seen with a long pulse, MI-gain will dominate leading to incoherent SC. However in normal GVD regime, with a short pulses as the MI is absent, SC is always highly coherent but as mentioned above, due to the rapid temporal spreading of the pulse the peak power decreases and thus it has the limited extent of spectral broadening. But with the long pulse, SC generation occurs due to the fast modulation on the pump pulse and thus SC is also incoherent.

## 7.6 Experiment and results

We generated SC in a bulk medium using the pump chain discussed in the previous chapters. As discussed in the previous section, the Ho:YLF laser, emitting ps-pulses cannot be used to generate stable supercontinuum. Therefore, we used the compressed output from the Kagome fiber experiment presented in Chapter 6. As a recall, in that chapter, we presented the results for the Kagome fiber based compression in two stages. At the end of the first stage, we compressed 1.8 ps long pulses to 285 fs at the energy of 125 $\mu$J. These pulses were later self-compressed in a second stage Kagome fiber and we achieved 48 fs pulses and energy of 60 $\mu$J. We used the output of both stages separately for SC generation whose results are presented in this chapter. The experimental layout for SC generation is simple and shown in figure 7.1. We focused the laser pulse using a lens of focal length 75 mm in a bulk medium and the output was collimated and sent to the spectrometer. We used three different materials,
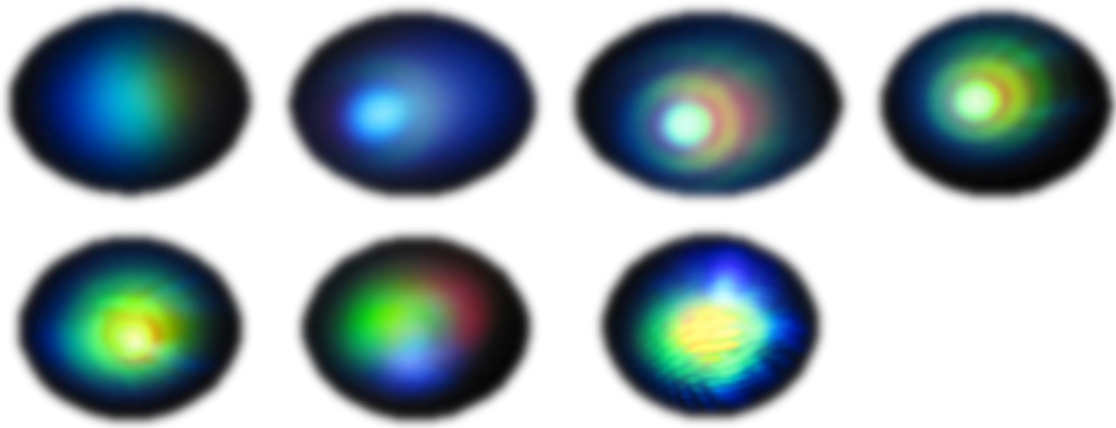
Figure 7.3: Beam profile of the SC at the visible wavelength obtained using a CCD camera

YAG, Sapphire and ZnSe windows of different thicknesses. As the pump pulse, we first used 285 fs pulses from the output of the first stage Kagome fiber. The window was initially kept away from the focus and slowly moved towards the focus. As the window was moved into the Rayleigh range of the lens, visible light was generated, whose color and profile changed as the window was further moved into the focus.

The beam profiles of SC obtained at different pump focus point in the crystal was collimated and recorded using a CCD camera that are shown in the figure 7.3. The output beam was collimated using another positive lens of focal length 100 mm. Due to the extremely low energy of the broad spectrum of the SC, it was difficult to measure its spectrum, especially at the longer wavelength where no good commercial spectrometer exists. Moreover, the high spectral power of the narrow-band pump wavelength that saturates the spectrometer, adds further complexity to the spectrum measurement. This is because it is difficult to find the narrow-band filter for the pump wavelength and at the same time 100 % transmission at the ultra-broad spectrum of the SC. Thus one needs to employ several filters before the spectrometer in different range for proper spectral analysis. For our measurement, we first used HR 4000 spectrometer from Ocean Optics Inc. which covers the wavelength from 200 - 1100 nm. This part of the spectrum was not difficult to measure due to high sensitivity in the spectral range and no detection of the pump wavelength. The figure 7.4 shows the normalized spectrum obtained from HR4000.

We then utilized NIRQuest model of Ocean Optics Inc. that covers the spectral range from 1200 nm - 2500 nm, to measure the long wavelength part of the spectrum after filtering out the pump. The pump was filtered using dielectric coated high
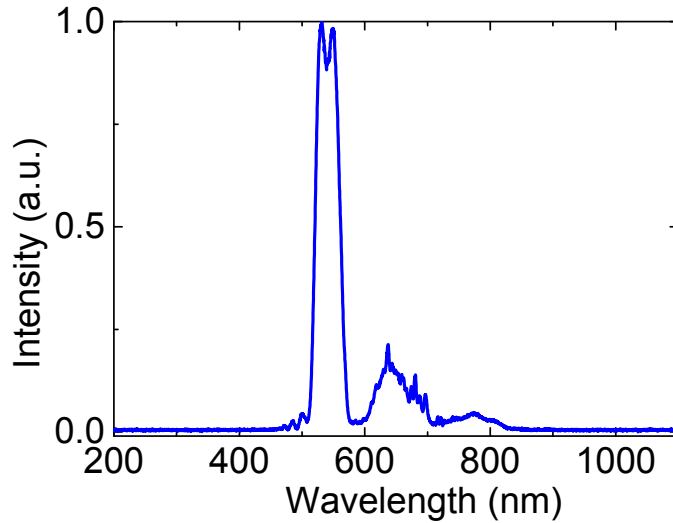
Figure 7.4: SC spectrum measured from HR4000 spectral covering the spectral range from 200 - 1100 nm
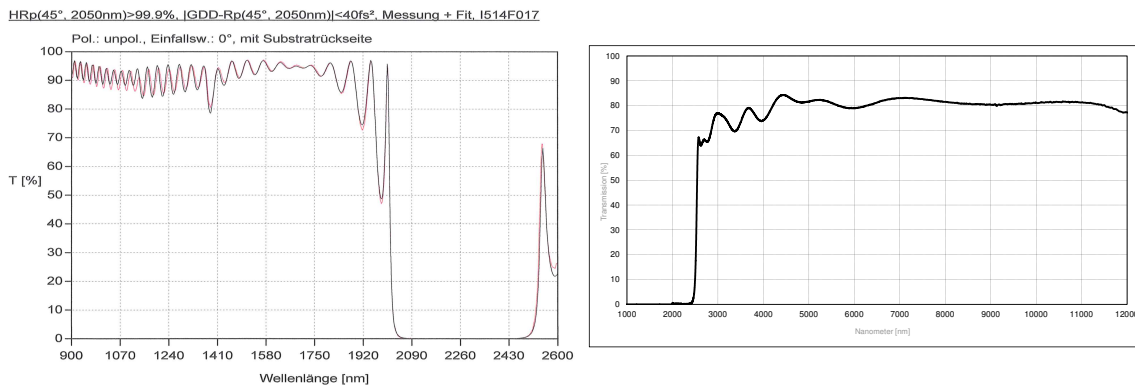


Figure 7.5: (a) The transmission curve of dielectric high reflective mirror (taken from Layertec Inc. measurement report) (b) uncoated Germanium window used as filter.

reflective (HR) mirrors and germanium filters to cut the pump out. In the figure 7.5, the transmission curve for both filters are shown.

Since the HR mirror has almost zero transmission around 2 $\mu$m wavelength, it acts as a perfect filter for the pump wavelength, but it also has a drawback that all the SC spectrum above 2 $\mu$m wavelength up to 2450 nm was cut out. However, there exists narrow spectral range above 2450 nm that can be measured with the NIRQuest spectrometer. The spectrum obtained with HR mirror as a filter, is shown in figure 7.6 (a). Similarly, the spectrum was also measured with a germanium (Ge) filter placed before the spectrometer. However, as seen in the figure 7.5, Ge does not transmit below 2500 nm and there exists a sharp cut-off at 2500 nm. And since our spectrometer range is only up to 2500, ideally we should not see any signal, but
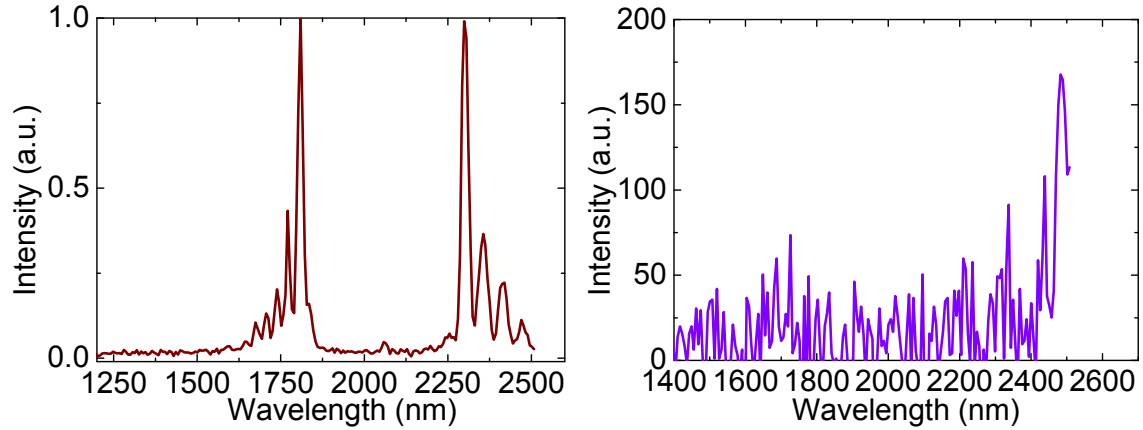
Figure 7.6: The SC spectrum measured from NIRQuest spectrometer with (a) HR mirror as filter (b) With Ge window as filter

due to small on the edges of the window, we saw a small amount of signal around 2500 nm confirming the spectral components around this wavelength (figure 7.6 (b)). Hence the SC spans from visible to at least 2500 nm, though not limited to 2500 nm, it could not be confirmed due to lack of measurement device.

## 7.7 Conclusions

In conclusion, we demonstrated SC generation as an application of the laser system developed during this work. We used three different materials YAG, Sapphire, and ZnSe window of different thickness. We measured the spectrum in the visible up to 500 nm and in the long wavelength side up to 2500 nm. Due to lack of measuring device, we could not measure the spectrum above 2500 nm but we believe that there must be low energy spectral components at an even longer wavelength which can be amplified using an OPA to generate even longer idler.

# Conclusions and Outlook

## 8.1  Conclusions

In this work, we demonstrated a simple and compact 2 $\mu$m wavelength, mJ-level Ho:YLF amplifier system producing 2.4 ps pulses. The system was seeded with a home-built seed oscillator having a pulse energy of 60 pJ. The Ho:YLF amplifier system initially produced 2 mJ energy pulses with a duration of 3.5 ps and the spectral bandwidth of 2.3 nm at 1 kHz repetition rate and < 1 % RMS fluctuations. Later, we implemented intracavity gain shaping with an etalon in the RA cavity both experimentally and numerically. Using this method, we were able to double the bandwidth of the pulses at the RA output from 2.9 nm to 5.4 nm (FWHM), that supports a minimum of 1 ps Fourier limit (FL) duration. The 60 pJ seed energy is amplified to 0.5 mJ in the RA. The output was further amplified via SPA to 2.2 mJ and after compression in a CVBG, we obtained the pulse duration of 3.4 ps. This was further improved to a pulse duration of 2.4 ps using etalon inside the RA. Together with SPA, we achieved 30 % reduction in pulse duration from 3.4 ps to 2.4 ps beyond the gain narrowing limit. This was the first demonstration of shortest pulse duration achieved from Ho:YLF RA together with a SPA both without gain shaping i.e. 3.4 ps and with gain shaping i.e. 2.4 ps [90].

Next, we demonstrated both experimentally and numerically a two-stage compression of 2-$\mu$m, 3.4-ps long pulses from the Ho:YLF amplifier down to a 7-cycle 48-fs

FWHM duration with 11 $\mu$J energy. Nonlinear propagation dynamics of ps-pulses in Kagome-type HC-PCF fibers was studied in two different geometries, 7-cell, and 19-cell designs. As a first stage, in the presence of air, maximum spectral broadening of 77 nm was observed in 19-cell fibers at incident energies of 707 $\mu$J with FL duration of 280 fs. The experiments were also repeated in Ar-filled fibers at 3 and 5 bars pressure for both designs. The best compression was achieved with the 7-cell fiber at 227 $\mu$J incident energy and Ar gas pressure of 5 bar with the maximum broadening of 88 nm which corresponds to a FL duration of 250 fs. Using external prism-pair, 1.8-ps pulses were compressed to 285 fs with FL duration of 250 fs and more than 70 % of the energy in the central peak. The total throughput energy in these fibers was 500 $\mu$J and 780 $\mu$J for 7-cell and 19-cell fiber respectively, with a high transmission efficiency of 90 %. Though, the best compression of 770 fs and 290 fs was achieved at 280 $\mu$J and 560 $\mu$J for 7-cell and 19-cell fiber respectively. As a second stage, the compressed pulse of 285-fs duration was further self-compressed down to a 7-cycle 48-fs FWHM duration with 11 $\mu$J energy in 2 meters of 7-cell fiber filled with air. This strong-field 7-cycle MIR source will have intriguing applications in strong-field attoscience experiments.

Hence depending on the application, broadening in both 7-cell and 19-cell fiber can be useful. For experiments that need only small amount of energy to be compressed as the one envisioned here, 7-cell fiber is optimum. Whereas, for experiments that require more compressed energy, 19-cell is a better choice. The numerical results suggest that, in the ps-regime, the spectral broadening is mostly dominated by SPM and no higher order effects are significant. This is for the first time (to the best of our knowledge) compression of 2-$\mu$m ps-laser pulses have been achieved. We further studied numerically the propagation of ps-pulses in these fibers and the model matches the experimental behavior of spectral evolution for different input conditions. This work is an important step in the generation of few to single-cycle MIR pulses directly from a compact ps-source. The 2-$\mu$m compressed output pulse from Kagome fiber enables generation of a stable supercontinuum in bulk solids in the MIR for seeding of OPAs. As an application, we demonstrated SC generation using the compressed output from Kagome fiber stage.

## 8.2 Outlook

As an outlook, since our front-end amplifier chain delivers output pulses with 2.2-mJ energy, and only a small fraction of it is used for the Kagome compression stage, all the remaining energy from the amplifier can be used to pump OPA stages. The output of the amplifier chain can be divided into two. One part, which has an energy of 225 $\mu$J, was used as the input for the Kagome nonlinear compression stage, while the remaining energy from the amplifier can be used to pump OPA. Thus, deriving the pump and seed pulses in the OPA from a common laser pulse, it permits pssibility to generate passively passively CEP-stable idler pulses [103]. Finally, generation of such MIR passively CEP stable pulses can be used to study several important phenomena in solid-state physics at the long wavelength where very few works have been yet demonstrated. For example, these long wavelength MIR pulse can be used to generate high-harmonics in solids [25]. And if properly scaled in energy, these studies can also be possible in gases. The long wavelength driver pulse can permit increased cutoff energy for attosecond pulse generation.

# Acknowledgment

Finally, a PhD cannot be deemed to complete without acknowledging numerous people who contribute directly or indirectly, not only to one of the greatest endeavor of life but also almost a half-decade combat with various problems we encounter, to which sometimes we succeed, and sometime not. First and foremost, I would like to thank my supervisor Prof. Franz X. Kaertner who gave me the lifetime opportunity to work under his supervision with proper financial support. I find myself deeply honored to have him as my supervisor whose patience and support provided an independent research environment which helped me to conquer my strength and weakness and mould in me the leadership skills.

I would like to offer my gratitude to all my colleagues at DESY, MIT and University of Limoges with whom I have had the chance to work with. In particular, I would like to acknowledge the names of those who have directly contributed to the success of this project. I would like to thank my mentor Dr. Huseyin Cankaya who have worked most closely with me in the past four years. A special thanks to him for supporting me throughout this time. I would then like to thank Dr. Oliver Muecke for the discussions and time he devoted for this project which helped me gain knowledge in the application side of MIR wavelength. With his out-of box thinking, on several occasion, he has helped in the lab without which I could end-up spending lot of time. His writing skills always helped polishing of the journal papers and which eventually improved my skills as well. Then I would like to mention of Dr. Giovanni Cirmi, whose help for measurement and analysis of FROG data that was crucial for the nonlinear compression experiments. And I cannot forget his humor, which always made scientific discussions enjoyable whether it be on the lunch table or at the end of the tiring day in the lab. I would like to thank Michael Hemmer whose vast knowledge of MIR and contacts became a life-savior for winding-up the experiments towards the end of PhD. In the simulation side, I would like to thank Gregory J. Stein and Kyung-Han Hong who developed the simulation model for the

# Eidesstattliche Versicherung
## *Declaration on Oath*

Hermit erkläre ich an Eides statt, dass ich die vorliegende Dissertationsschrift selbst verfasst und keine anderen als die angegebenen Quellen und Hilfsmittel benutzt habe.

*I hereby declare, on oath, that I have written the present dissertation by my own and have not used other than the acknowledged resources.*

Hamburg, den                         Unterschrift

*Hamburg, date*                        *Signature*

# Bibliography

[1] P. B. Corkum and F. Krausz, "Attosecond science," *Nature Physics*, vol. 3, pp. 381–387, jun 2007.

[2] Q. Peng, A. Juzeniene, J. Chen, L. O. Svaasand, T. Warloe, K.-E. Giercksky, and J. Moan, "Lasers in medicine," *Reports on Progress in Physics*, vol. 71, no. 5, p. 056701, 2008.

[3] G. Agarwal, *Nonlinear Fiber Optics*. Elsevier, 2016.

[4] F. Kaertner, "Ultrafast Optics Class Notes," 2014.

[5] G. Mourou, T. Tajima, M. N. Quinn, B. Brocklesby, and J. Limpert, "Nuclear Instruments and Methods in Physics Research A Are fi ber-based lasers the future of accelerators ?," *Nuclear Inst. and Methods in Physics Research, A*, vol. 740, pp. 17–20, 2014.

[6] F. Benabid, F. Gérôme, L. Vincetti, B. Debord, M. Alharbi, and T. Bradley, "Inhibited coupling hollow-core photonic crystal fiber," *SPIE Photonics West 2014-OPTO: Optoelectronic Devices and Materials*, vol. 8994, p. 89940A, 2014.

[7] G. J. Stein, "Modeling of nonlinear ultrashort optical pulse propagation," Master's thesis, Massachuesetts Institute of Technology, 2015.

[8] F. Krausz and M. Ivanov, "Attosecond physics," *Reviews of Modern Physics*, vol. 81, no. 1, pp. 163–234, 2009.

[9] J. Biegert, P. K. Bates, and O. Chalus, "New mid-infrared light sources," *IEEE Journal on Selected Topics in Quantum Electronics*, vol. 18, no. 1, pp. 531–540, 2012.

[10] T. Brabec and F. Krausz, "Intense few-cycle laser fields: Frontiers of nonlinear optics," *Reviews of Modern Physics*, vol. 72, no. 2, pp. 545–591, 2000.

[11] G. A. Mourou, C. P. J. Barry, and M. D. Perry, "Ultrahigh-intensity lasers: physics of the extreme on a tabletop," *Physics Today*, vol. 51, no. 1, pp. 22–28, 1998.

[12] U. Keller, "Recent developments in compact ultrafast lasers.," *Nature*, vol. 424, no. 6950, pp. 831–838, 2003.

[13] H. Pires, M. Baudisch, D. Sanchez, M. Hemmer, and J. Biegert, "Ultrashort pulse generation in the mid-IR," *Progress in Quantum Electronics*, vol. 43, pp. 1–30, sep 2015.

[14] B. Sheehy, J. Martin, L. DiMauro, P. Agostini, K. Schafer, M. Gaarde, and K. Kulander, "High Harmonic Generation at Long Wavelengths," *Physical Review Letters*, vol. 83, no. 25, pp. 5270–5273, 1999.

[15] A. Gordon and F. X. Kärtner, "Scaling of keV HHG photon yield with drive wavelength," *Optics Express*, vol. 13, no. 8, p. 2941, 2005.

[16] T. Popmintchev, M.-C. Chen, D. Popmintchev, P. Arpin, S. Brown, S. Alisauskas, G. Andriukaitis, T. Balciunas, O. D. Mucke, A. Pugzlys, A. Baltuska, B. Shim, S. E. Schrauth, A. Gaeta, C. Hernandez-Garcia, L. Plaja, A. Becker, A. Jaron-Becker, M. M. Murnane, and H. C. Kapteyn, "Bright Coherent Ultrahigh Harmonics in the keV X-ray Regime from Mid-Infrared Femtosecond Lasers," *Science*, vol. 336, no. 6086, pp. 1287–1291, 2012.

[17] J. Tate, T. Auguste, H. G. Muller, P. Salières, P. Agostini, and L. F. Dimauro, "Scaling of wave-packet dynamics in an intense midinfrared Field," *Physical Review Letters*, vol. 98, no. 1, pp. 1–4, 2007.

[18] C. I. Blaga, F. Catoire, P. Colosimo, G. G. Paulus, H. G. Muller, P. Agostini, and L. F. DiMauro, "Strong-field photoionization revisited," *Nature Physics*, vol. 5, pp. 335–338, may 2009.

[19] J. Dura, N. Camus, A. Thai, A. Britz, M. Hemmer, M. Baudisch, A. Senftleben, C. D. Schröter, J. Ullrich, R. Moshammer, and J. Biegert, "Ionization with low-frequency fields in the tunneling regime," *Scientific Reports*, vol. 3, p. 2675, sep 2013.

[20] A. Ludwig, J. Maurer, B. W. Mayer, C. R. Phillips, L. Gallmann, and U. Keller, "Breakdown of the dipole approximation in strong-field ionization," *Physical Review Letters*, vol. 113, no. 24, pp. 1–5, 2014.

[21] P. Colosimo, G. Doumy, C. I. Blaga, J. Wheeler, C. Hauri, F. Catoire, J. Tate, R. Chirla, a. M. March, G. G. Paulus, H. G. Muller, P. Agostini, and

L. F. DiMauro, "Scaling strong-field interactions towards the classical limit," *Nature Physics*, vol. 4, pp. 386–389, may 2008.

[22] C. I. Blaga, J. Xu, A. D. DiChiara, E. Sistrunk, K. Zhang, P. Agostini, T. a. Miller, L. F. DiMauro, and C. D. Lin, "Imaging ultrafast molecular dynamics with laser-induced electron diffraction," *Nature*, vol. 483, pp. 194–197, mar 2012.

[23] A. H. Chin, J. M. Bakker, and J. Kono, "Ultrafast electroabsorption at the transition between classical and quantum response," *Physical Review Letters*, vol. 85, no. 15, pp. 3293–3296, 2000.

[24] S. Ghimire, A. D. Dichiara, E. Sistrunk, U. B. Szafruga, P. Agostini, L. F. Dimauro, and D. A. Reis, "Redshift in the optical absorption of ZnO single crystals in the presence of an intense midinfrared laser field," *Physical Review Letters*, vol. 107, no. 16, pp. 1–5, 2011.

[25] S. Ghimire, A. D. DiChiara, E. Sistrunk, P. Agostini, L. F. DiMauro, and D. A. Reis, "Observation of high-order harmonic generation in a bulk crystal," *Nature Physics*, vol. 7, pp. 138–141, feb 2011.

[26] O. D. Mücke, "Isolated high-order harmonics pulse from two-color-driven Bloch oscillations in bulk semiconductors," *Physical Review B*, vol. 84, p. 081202, aug 2011.

[27] K. F. Mak, J. C. Travers, N. Y. Joly, A. Abdolvand, and P. S. J. Russell, "Two techniques for temporal pulse compression in gas-filled hollow-core kagomé photonic crystal fiber," *Optics Letters*, vol. 38, p. 3592, sep 2013.

[28] M. Hemmer, M. Baudisch, A. Thai, A. Couairon, and J. Biegert, "Self-compression to sub-3-cycle duration of mid-infrared optical pulses in dielectrics," *Optics Express*, vol. 21, no. 23, pp. 28095–28102, 2013.

[29] C. Vozzi, G. Cirmi, C. Manzoni, E. Benedetti, F. Calegari, G. Sansone, S. Stagira, O. Svelto, S. De Silvestri, M. Nisoli, and G. Cerullo, "High-energy, few-optical-cycle pulses at 1.5 $\mu$m with passive carrier-envelope phase stabilization," *Optics Express*, vol. 14, no. 21, pp. 10109–10116, 2006.

[30] T. Wilhelm, J. Piel, and E. Riedle, "Sub-20-fs pulses tunable across the visible from a blue-pumped single-pass noncollinear parametric converter," *Optics Letters*, vol. 22, no. 19, p. 1494, 1997.

[31] C. Schriever, S. Lochbrunner, P. Krok, and E. Riedle, "Tunable pulses from below 300 to 970 nm with durations down to 14 fs based on a 2 MHz

ytterbium-doped fiber system.," *Optics letters*, vol. 33, no. 2, pp. 192–194, 2008.

[32] D. Brida, M. Marangoni, C. Manzoni, S. D. Silvestri, and G. Cerullo, "Two-optical-cycle pulses in the mid-infrared from an optical parametric amplifier.," *Optics letters*, vol. 33, no. 24, pp. 2901–2903, 2008.

[33] O. Chalus, A. Thai, P. K. Bates, and J. Biegert, "Six-cycle mid-infrared source with 38 $\mu$J at 100 kHz," *Optics Letters*, vol. 35, p. 3204, oct 2010.

[34] C. R. Phillips, J. Jiang, C. Mohr, A. C. Lin, C. Langrock, M. Snure, D. Bliss, M. Zhu, I. Hartl, J. S. Harris, M. E. Fermann, and M. M. Fejer, "Widely tunable midinfrared difference frequency generation in orientation-patterned GaAs pumped with a femtosecond Tm-fiber system," *Optics Letters*, vol. 37, p. 2928, jul 2012.

[35] O. Chalus, P. G. Schunemann, K. T. Zawilski, J. Biegert, and M. Ebrahim-Zadeh, "Optical parametric generation in CdSiP2.," *Optics Letters*, vol. 35, no. 24, pp. 4142–4144, 2010.

[36] V. Petrov, "Parametric down-conversion devices: The coverage of the mid-infrared spectral range by solid-state laser sources," *Optical Materials*, vol. 34, pp. 536–554, jan 2012.

[37] F. Silva, D. R. Austin, A. Thai, M. Baudisch, M. Hemmer, D. Faccio, A. Couairon, and J. Biegert, "Multi-octave supercontinuum generation from mid-infrared filamentation in a bulk crystal.," *Nature communications*, vol. 3, no. may, p. 807, 2012.

[38] H. Liang, P. Krogen, R. Grynko, O. Novak, C.-L. Chang, G. J. Stein, D. Weerawarne, B. Shim, F. X. Kärtner, and K.-H. Hong, "Three-octave-spanning supercontinuum generation and sub-two-cycle self-compression of mid-infrared filaments in dielectrics," *Optics Letters*, vol. 40, no. 6, pp. 1069–1072, 2015.

[39] P. Malevich, G. Andriukaitis, T. Flöry, a. J. Verhoef, a. Fernández, S. Ališauskas, a. Pugžlys, a. Baltuška, L. H. Tan, C. F. Chua, and P. B. Phua, "High energy and average power femtosecond laser for driving mid-infrared optical parametric amplifiers.," *Optics letters*, vol. 38, no. 15, pp. 2746–2749, 2013.

[40] D. Sanchez, M. Hemmer, M. Baudisch, S. L. Cousin, K. Zawilski, P. Schunemann, O. Chalus, C. Simon-Boisson, and J. Biegert, "7 $\mu$m, ultrafast,

sub-millijoule-level mid-infrared optical parametric chirped pulse amplifier pumped at 2 $\mu$m," *Optica*, vol. 3, p. 147, feb 2016.

[41] A. Godard, "Infrared (2-12 $\mu$m) solid-state laser sources: a review," *Comptes Rendus Physique*, vol. 8, pp. 1100–1128, dec 2007.

[42] G. Cerullo and S. De Silvestri, "Ultrafast optical parametric amplifiers," *Review of Scientific Instruments*, vol. 74, no. 1 I, pp. 1–18, 2003.

[43] Y. R. Shen, *The Principles of Nonlinear Optics.*
Wiley, 2002.

[44] R. Boyd, *Nonlinear Optics.*
Elsevier, third ed., 2008.

[45] A. Wienke, D. Wandt, U. Morgner, J. Neumann, and D. Kracht, "700 MW peak power of a 380 fs regenerative amplifier with Tm:YAP," *Opt. Express*, vol. 23, no. 13, pp. 16884–16889, 2015.

[46] H. A. Haus, "Mode-locking of lasers," *IEEE Journal on Selected Topics in Quantum Electronics*, vol. 6, no. 6, pp. 1173–1185, 2000.

[47] F. X. Kärtner, I. D. Jung, and U. Keller, "Soliton mode-locking with saturable absorbers," *IEEE Journal on Selected Topics in Quantum Electronics*, vol. 2, no. 3, pp. 540–556, 1996.

[48] S. Y. Set, H. Yaguchi, Y. Tanaka, and M. Jablonski, "Laser Mode Locking Using a Saturable Absorber Incorporating Carbon Nanotubes," *Journal of Lightwave Technology*, vol. 22, no. 1, pp. 51–56, 2004.

[49] S. Yamashita, Y. Inoue, S. Maruyama, Y. Murakami, H. Yaguchi, M. Jablonski, and S. Y. Set, "Saturable absorbers incorporating carbon nanotubes directly synthesized onto substrates and fibers and their application to mode-locked fiber lasers.," *Optics letters*, vol. 29, no. 14, pp. 1581–3, 2004.

[50] T. R. Schibli, K. Minoshima, H. Kataura, E. Itoga, N. Minami, S. Kazaoui, K. Miyashita, M. Tokumoto, and Y. Sakakibara, "Ultrashort pulse-generation by saturable absorber mirrors based on polymer-embedded carbon nanotubes," *Optics Express*, vol. 13, no. 20, p. 8025, 2005.

[51] M. Zhang, E. J. R. Kelleher, F. Torrisi, Z. Sun, T. Hasan, D. Popa, F. Wang, A. C. Ferrari, S. V. Popov, and J. R. Taylor, "Tm-doped fiber laser mode-locked by graphene-polymer composite," *Optics Express*, vol. 20, pp. 25077–25084, oct 2012.

[52] U. Keller, K. Weingarten, F. Kartner, D. Kopf, B. Braun, I. Jung, R. Fluck, C. Honninger, N. Matuschek, and J. Aus der Au, "Semiconductor saturable absorber mirrors (SESAM's) for femtosecond to nanosecond pulse generation in solid-state lasers," *IEEE Journal of Selected Topics in Quantum Electronics*, vol. 2, no. 3, pp. 435–453, 1996.

[53] N. Coluccelli, A. Lagatsky, A. D. Lieto, M. Tonelli, G. Galzerano, W. Sibbett, and P. Laporta, "Passive mode locking of an in-band-pumped Ho:YLiF<sub>4</sub> laser at 2.06?$\mu$m.," *Optics letters*, vol. 36, no. 16, pp. 3209–3211, 2011.

[54] P. Li, A. Ruehl, U. Grosse-Wortmann, and I. Hartl, "Sub-100 fs passively mode-locked holmium-doped fiber oscillator operating at 2.06 mm," in *Optics letters* (L. B. Shaw, ed.), vol. 39, p. 93441L, SPIE-Intl Soc Optical Eng, mar 2015.

[55] L. M. Frantz and J. S. Nodvik, "Theory of Pulse Propagation in a Laser Amplifier," *Journal of Applied Physics*, vol. 34, no. 8, p. 2346, 1963.

[56] M. Grishin and A. Michailovas, *Dynamics of Continuously Pumped Solid-State Regenerative Amplifiers.*
No. February in 12, Intech, 2010.

[57] A. Dergachev, "High-energy, kHz-rate, picosecond, 2-$\mu$m laser pump source for mid-IR nonlinear optical devices," *Photonic West*, vol. 8599, pp. 85990B–85990B–14, 2013.

[58] J. Peng, H. Xia, P. Wang, H. Hu, L. Tang, Y. Zhang, H. Jiang, and B. Chen, "Optical spectra and gain properties of Ho3+/Pr3+ Co-doped LiYF4 crystal," *Journal of Materials Science and Technology*, vol. 30, no. 9, pp. 910–916, 2014.

[59] P. Kroetz, A. Ruehl, K. Murari, H. Cankaya, A.-l. Calendron, F. Kaertner, I. Hartl, and R. D. Miller, "High Energy and Low Noise Ho:YLF Regenerative Amplifiers: A Noise and Stability Analysis," in *CLEO: 2015*, (Washington, D.C.), p. SF1F.3, OSA, 2015.

[60] J. Dörring, A. Killi, U. Morgner, A. Lang, M. Lederer, and D. Kopf, "Period doubling and deterministic chaos in continuously pumped regenerative amplifiers.," *Optics express*, vol. 12, no. 8, pp. 1759–1768, 2004.

[61] J. Swain and F. Rainer, "Many-pass resonant laser amplifier," *IEEE Journal of Quantum Electronics*, vol. 5, pp. 385–386, jul 1969.

[62] X. D. Wang, P. Basseras, R. J. Dwayne Miller, J. Sweetser, and I. A. Walmsley, "Regenerative pulse amplification in the 10-kHz range," *Opt. Lett.*, vol. 15, no. 15, pp. 839–841, 1990.

[63] P. Kroetz, A. Ruehl, G. Chatterjee, A.-L. Calendron, K. Murari, H. Cankaya, P. Li, F. X. Kärtner, I. Hartl, and R. J. Dwayne Miller, "Overcoming bifurcation instability in high-repetition-rate Ho:YLF regenerative amplifiers," *Optics Letters*, vol. 40, p. 5427, dec 2015.

[64] P. Kroetz, A. Ruehl, A.-L. Calendron, G. Chatterjee, H. Cankaya, K. Murari, F. X. Kaertner, I. Hartl, and R. J. D. MIller, "Operation regimes , gain dynamics and highly stable operation points of Ho : YLF regenerative amplifiers," *Opt. Express*, 2016.

[65] C. P. Barty, G. Korn, F. Raksi, C. Rose-Petruck, J. Squier, a. C. Tien, K. R. Wilson, V. V. Yakovlev, and K. Yamakawa, "Regenerative pulse shaping and amplification of ultrabroadband optical pulses.," *Optics letters*, vol. 21, no. 3, pp. 219–221, 1996.

[66] I. P. Christov and M. B. Danailov, "Theory of ultrabroadband light amplification in a spatially-dispersive scheme," *Optics Communications*, vol. 84, no. 1-2, pp. 61–66, 1991.

[67] J. Faure, J. Itatani, S. Biswal, G. Chériaux, L. R. Bruner, G. C. Templeton, and G. Mourou, "A spatially dispersive regenerative amplifier for ultrabroadband pulses," *Optics Communications*, vol. 159, no. 1-3, pp. 68–73, 1999.

[68] Y. Leng, L. Lin, W. Wang, Y. Jiang, B. Tang, and Z. Xu, "Broadband spectral shaping in a Ti:sapphire regenerative amplifier," *Optics and Laser Technology*, vol. 35, no. 6, pp. 425–429, 2003.

[69] P. Kroetz, A. Ruehl, K. Murari, H. Cankaya, F. X. Kärtner, I. Hartl, and R. J. D. Miller, "Numerical study of spectral shaping in high energy Ho:YLF amplifiers," *Optics Express*, vol. 24, no. 9, p. 9905, 2016.

[70] K. Mecseki, D. Bigourd, S. Patankar, N. H. Stuart, and R. a. Smith, "Flat-top picosecond pulses generated by chirped spectral modulation from a Nd:YLF regenerative amplifier for pumping few-cycle optical parametric amplifiers.," *Applied optics*, vol. 53, no. 10, pp. 2229–35, 2014.

[71] J. M. Dudley, G. Genty, and S. Coen, "Supercontinuum generation in photonic crystal fiber," *Reviews of Modern Physics*, vol. 78, pp. 1135–1184, oct 2006.

[72] R. F. Cregan, B. J. Mangan, J. C. Knight, T. A. Birks, P. S. J. Russell, P. J. Roberts, and D. C. Allan, "Single-mode photonic band gap guidance of light in air," *Science*, vol. 285, no. 5433, pp. 1537–1539, 1999.

[73] F. Benabid and P. Roberts, "Linear and nonlinear optical properties of hollow core photonic crystal fiber," *Journal of Modern Optics*, vol. 58, pp. 87–124, jan 2011.

[74] F. Benabid, "Hollow-core photonic bandgap fibre: new light guidance for new science and technology.," *Philosophical transactions. Series A, Mathematical, physical, and engineering sciences*, vol. 364, no. 1849, pp. 3439–3462, 2006.

[75] F. Couny, F. Benabid, P. J. Roberts, P. S. Light, M. G. Raymer, O.-f. Combs, F. Couny, F. Benabid, P. J. Roberts, P. S. Light, and M. G. Raymer, "Generation and Photonic," *Science*, vol. 318, no. November, pp. 1118–1121, 2007.

[76] Y. Y. Wang, N. V. Wheeler, F. Couny, P. J. Roberts, and F. Benabid, "Low loss broadband transmission in hypocycloid-core Kagome hollow-core photonic crystal fiber.," *Optics letters*, vol. 36, no. 5, pp. 669–671, 2011.

[77] Y. Y. Wang, X. Peng, M. Alharbi, C. F. Dutin, T. D. Bradley, F. Gérôme, M. Mielke, T. Booth, and F. Benabid, "Design and fabrication of hollow-core photonic crystal fibers for high-power ultrashort pulse transportation and pulse compression," *Optics Letters*, vol. 37, no. 15, p. 3111, 2012.

[78] B. Debord, M. Alharbi, L. Vincetti, A. Husakou, C. Fourcade-Dutin, C. Hoenninger, E. Mottay, F. Gérôme, and F. Benabid, "Multi-meter fiber-delivery and pulse self-compression of milli-Joule femtosecond laser and fiber-aided laser-micromachining.," *Optics express*, vol. 22, no. 9, pp. 10735–46, 2014.

[79] J. Nold, P. Hölzer, N. Y. Joly, G. K. L. Wong, a. Nazarkin, a. Podlipensky, M. Scharrer, and P. S. J. Russell, "Pressure-controlled phase matching to third harmonic in Ar-filled hollow-core photonic crystal fiber.," *Optics letters*, vol. 35, no. 17, pp. 2922–4, 2010.

[80] O. H. Heckl, C. R. E. Baer, C. Kränkel, S. V. Marchese, F. Schapper, M. Holler, T. Südmeyer, J. S. Robinson, J. W. G. Tisch, F. Couny, P. Light, F. Benabid, and U. Keller, "High harmonic generation in a gas-filled hollow-core photonic crystal fiber," *Applied Physics B: Lasers and Optics*, vol. 97, no. 2, pp. 369–373, 2009.

[81] H. Ren, A. Nazarkin, J. Nold, and P. S. Russell, "Quasi-phase-matched high harmonic generation in hollow core photonic crystal fibers," *Optics Express*, vol. 16, no. 21, p. 17052, 2008.

[82] G. P. Agrawal, "Nonlinear fiber optics: its history and recent progress [Invited]," *Journal of the Optical Society of America B*, vol. 28, p. A1, dec 2011.

[83] F. Yu and J. C. Knight, "Negative Curvature Hollow-Core Optical Fiber," *IEEE Journal of Selected Topics in Quantum Electronics*, vol. 22, no. 2, pp. 1–10, 2016.

[84] P. Roberts, F. Couny, H. Sabert, B. Mangan, D. Williams, L. Farr, M. Mason, A. Tomlinson, T. Birks, J. Knight, and P. St J Russell, "Ultimate low loss of hollow-core photonic crystal fibres.," *Optics express*, vol. 13, no. 1, pp. 236–244, 2005.

[85] F. Benabid, J. C. Knight, G. Antonopoulos, and P. S. J. Russell, "Stimulated Raman Scattering in Photonic Crystal Fiber," *October*, vol. 298, no. October, pp. 2000–2003, 2002.

[86] K. F. Mak, M. Seidel, O. Pronin, M. H. Frosz, A. Abdolvand, V. Pervak, A. Apolonski, F. Krausz, J. C. Travers, and P. S. J. Russell, "Compressing $\mu$J-level pulses from 250 fs to sub-10 fs at 38-MHz repetition rate using two gas-filled hollow-core photonic crystal fiber stages," *Optics Letters*, vol. 40, no. 7, p. 1238, 2015.

[87] F. Guichard, A. Giree, Y. Zaouter, M. Hanna, G. Machinet, B. Debord, F. Gérôme, P. Dupriez, F. Druon, C. Hönninger, E. Mottay, F. Benabid, and P. Georges, "Nonlinear compression of high energy fiber amplifier pulses in air-filled hypocycloid-core Kagome fiber," *Optics Express*, vol. 23, no. 6, pp. 7416–7423, 2015.

[88] M. Gebhardt, C. Gaida, S. Hädrich, F. Stutzki, C. Jauregui, J. Limpert, and A. Tünnermann, "Nonlinear compression of an ultrashort-pulse thulium-based fiber laser to sub-70 fs in Kagome photonic crystal fiber," *Optics Letters*, vol. 40, p. 2770, jun 2015.

[89] T. Balciunas, C. Fourcade-Dutin, G. Fan, T. Witting, A. A. Voronin, A. M. Zheltikov, F. Gerome, G. G. Paulus, A. Baltuska, and F. Benabid, "A strong-field driver in the single-cycle regime based on self-compression in a kagome fibre.," *Nature communications*, vol. 6, no. May 2014, p. 6117, 2015.

[90] K. Murari, H. Cankaya, P. Kroetz, G. Cirmi, P. Li, A. Ruehl, I. Hartl, and F. X. Kärtner, "Intracavity gain shaping in millijoule-level, high gain Ho:YLF regenerative amplifiers," *Optics Letters*, vol. 41, pp. 1114–1117, mar 2016.

[91] D. Wang, Y. Leng, and Z. Xu, "Measurement of nonlinear refractive index coefficient of inert gases with hollow-core fiber," *Applied Physics B: Lasers and Optics*, vol. 111, no. 3, pp. 447–452, 2013.

[92] R. R. Alfano and S. L. Shapiro, "Observation of self-phase modulation and small-scale filaments in crystals and glasses," *Phys. Rev. Lett.*, vol. 24, pp. 592–594, mar 1970.

[93] J. K. Ranka, R. S. Windeler, and A. J. Stentz, "Visible continuum generation in air-silica microstructure optical fibers with anomalous dispersion at 800 nm," *Optics Letters*, vol. 25, p. 25, jan 2000.

[94] G. Genty, S. Coen, and J. M. Dudley, "Fiber supercontinuum sources (Invited)," *Journal of the Optical Society of America B*, vol. 24, no. 8, p. 1771, 2007.

[95] K. Blow and D. Wood, "Theoretical description of transient stimulated Raman scattering in optical fibers," *IEEE Journal of Quantum Electronics*, vol. 25, no. 12, pp. 2665–2673, 1989.

[96] L. F. Mollenauer, R. H. Stolen, J. P. Gordon, and W. J. Tomlinson, "Extreme picosecond pulse narrowing by means of soliton effect in single-mode optical fibers.," *Optics letters*, vol. 8, no. 5, pp. 289–291, 1983.

[97] Y. Kodama and A. Hasegawa, "Nonlinear pulse propagation in a monomode dielectric guide," *IEEE Journal of Quantum Electronics*, vol. 23, pp. 510–524, may 1987.

[98] J. E. Rothenberg, "Space–time focusing: breakdown of the slowly varying envelope approximation in the self-focusing of femtosecond pulses," *Optics Letters*, vol. 17, pp. 1340–1342, Oct 1992.

[99] N. Bloembergen, "Role of cracks, pores, and absorbing inclusions on laser induced damage threshold at surfaces of transparent dielectrics.," *Applied optics*, vol. 12, no. 4, pp. 661–664, 1973.

[100] W. Werncke, A. Lau, M. Pfeiffer, K. Lenz, H.-J. Weigmann, and C. Thuy, "An anomalous frequency broadening in water," *Optics Communications*, vol. 4, pp. 413–415, feb 1972.

[101] A. L. Gaeta, "Catastrophic Collapse of Ultrashort Pulses," *Physical Review Letters*, vol. 84, pp. 3582–3585, apr 2000.

[102] J. Swiderski, "High-power mid-infrared supercontinuum sources: Current status and future perspectives," *Progress in Quantum Electronics*, vol. 38, pp. 189–235, sep 2014.

[103] G. Cerullo, A. Baltuška, O. D. Mücke, and C. Vozzi, "Few-optical-cycle light pulses with passive carrier-envelope phase stabilization," *Laser and Photonics Reviews*, vol. 5, no. 3, pp. 323–351, 2011.